Title
Development of an Optically Detected Magnetic Resonance Spectrometer under pressure

Author
Wang, Zhipan

Publication Date
2022

Peer reviewed|Thesis/dissertation

Development of an Optically Detected Magnetic Resonance Spectrometer under pressure

By

Zhipan Wang
DISSERTATION

Submitted in partial satisfaction of the requirements for the degree of

DOCTOR OF PHILOSOPHY

in

PHYSICS

in the

OFFICE OF GRADUATE STUDIES

of the

UNIVERSITY OF CALIFORNIA

DAVIS

Approved:

[Nicholas J. Curro] (Chair)

[Valentin Taufour]

[Dong Yu]

Committee in Charge
2022

For my parents,
the woman I love, Jiaqi,
who give me endless support and love

Contents

List of Figures

List of Tables

Abstract

Nitrogen-vacancy color centers in diamond have attracted broad attention as quantum sensors for AC mangetic field. Here we develop a quantum diamond spectrometer for both ambient condition and under pressure in diamond anvil cells. Optically based nuclear magnetic resonance has been achieved and various AC sensing methods have been demonstrated. A clear signal from precessing ^{13}C spins in the diamond lattice has been found. The synchronized readout sensitivity at ambient and 3.6 GPa pressure are 1.9 and 7.6 $nT/\sqrt{Hz}$, respectively. In order to decrease the pressure inhomogeneity, a novel method – double quantum resonance – has been testified and discussed.

Using conventional nuclear magnetic resonance approach, a rare earth insulator $TmVO_4$, which is a model system to study nematic order and the roles played by nematic fluctuations, has been studied as a function of temperature and magnetic field direction orientation. We find that the magnetic shift tensor agrees quantitatively with direct dipolar coupling between the V nuclear moments and the Tm 4f moments. The spin-lattice relaxation rate exhibits a steep minimum for a field oriented 90° to the c axis, which is inconsistent with purely magnetic fluctuations. It is likely that both quadrupolar and magnetic fluctuations are present and drive spin-lattice relaxation.

Acknowledgments

It gives me genuine pleasure to express my deep sense of gratitude to my major professor Nick Curro, for his continuous guidance and help with my studies, for his patience, motivation, and his curiosity in research. I am so grateful that I have Nick as my mentor and eventually it makes up my mind to become a researcher like him.

Secondly, I would like to thank Peter Klavins, who is so unselfish to share his experiences in experimental physics. From the basic coil making to the challenging cryogenic systems, he gradually makes me a qualified experimentalist.

I would also like to thank Bill Casey and Valentin Taufour, who gave my lots of practical guidance from a different perspective. The generous contribution of their time and energy made these research works possible.

To all Curro lab graduate students – Tanat Kissikov, Louis Steele, Victoria Norman, Chris McPherson, Phurba Sherpa, Rashad Kadado, Cameron Chaffey and Yu-Hsuan Nian – it has been a pleasure working with you.

Finally, I should thank all the friends who has been knowing me during these five years. You guys fill up my life outside of physics and keep me in check all the time. For my love Jackie and my parents, thank you for carrying me through the difficulty, especially during the pandemic lock-down. There is no way I can earn this degree without you!

Chapter 1

Spin systems and magnetic resonance

The solid is the state where a large amount of particles break translation symmetry and take up some lattice structure so as to minimize the total potential energy. The fundamental particle usually is atom, which consists of electron(s) and nuclei. The nucleus is much heavier than electron ($\frac{m_p}{m_e} = 1836.153$), hence electrons have better mobility. By the uncertainty principle, we can infer that electron has much bigger energy variation than the nuclei. In fact, in most cases, the electrons control most physical properties of the solids.

In the Born–Oppenheimer approximation, we assume that the wave functions of the nuclei and electrons can be treated separately. In the following sections, we will introduce electron and nuclear spins behavior in the solid systems and how we can probe the physical properties using these local probes.

1.1 Electrons in solids

Electrons in solids can be roughly categorized into two types: valence (ion) electrons that behaves like atomic electrons that form ions together with nuclei core; and

conduction electrons that hop from one site to another.

Since the periodic structure breaks continuous translation symmetry, electrons can be described by Bloch waves. Their energies are described by the band structure, which is analogous to the energy levels of atoms. Conduction electrons usually exist near the Fermi energy. For insulators, there is a gap near the Fermi energy, which dominates the electron behavior. The typical gap size is around $0.1 \sim 4$ eV ($0.1 \sim 4.6 \times 10^4$ K). For metals, conduction electrons play important roles in transport, magnetism and so on.

Due to the mobility of conduction electrons, they cannot be easily described by a single energy level due to the uncertainly principle. On the other hand, valence electrons, which are more localized, usually can be treated as linear combination of atomic orbitals with other perturbations. In such case, we can picture these electrons as single particles carrying magnetic moments.

If we assume the spin orbit coupling is rather weak, the valence electron's magnetic moment might be written as (assuming $\hbar = 1$ from now on):

$$\mu_{\mathbf{e}} = g\mu_B \mathbf{S}, \tag{1.1}$$

where μ_B is the Bohr magneton and g is called g-factor. For free electron g = 2.0023. Due to the Zeeman effect, the electron's Hamiltonian under magnetic field is:

$$H_{Zeeman} = g\mu_B \mathbf{S} \cdot \mathbf{B}, \tag{1.2}$$

where $\mathbf{B} = B_0 \hat{z}$ is the external magnetic field. Projecting onto the z axis, the degeneracy is lifted by $m_s = \pm 1/2$:

$$E_{\pm} = \pm g\mu_B B_0/2 \tag{1.3}$$

$$\Delta E = g\mu_B B_0 \tag{1.4}$$

If there is microwave (MW) radiation (photon) that obeys $h\nu_e = \Delta E$, the absorption rate for single electron can be written as:

$$p_{\pm} \sim |\langle -| \mathbf{D} |+\rangle|^2 \delta(h\nu - \Delta E), \tag{1.5}$$

where $\mathbf{D}$ is the magnetic dipole for spin resonance. In other words, during a sweep of MW frequency, the electron spin in the lowest energy state (- state) can move to the upper state (+ state) by absorbing a quantum of electromagnetic radiation energy (photon) when $h\nu = \Delta E$. This phenomenon is called electron spin resonance (ESR).

For a macroscopic sample, it includes many electron spins interacting with themselves and the environment. The absorption rate in total is given by computing the number of spins per second that go from the lower energy to the upper [74]:

$$\frac{dE}{dt} = \Delta E p_{\pm}(N_- - N_+), \tag{1.6}$$

where N_+ and N_- are number of electrons on + and − energy levels respectively. The two terms both contribute to the rate since $p_{+\to-} = p_{-\to+} = p_{\pm}$ according to Eq. 1.5. It can also be justified by total spin momentum conservation. Therefore, the prerequisite of non-zero absorption in macroscopic system is an unbalanced spin number distribution (spin polarization): $n = N_- - N_+ > 0$.

Luckily, due to the Boltzmann distribution, the spin numbers should obey:

$$\frac{N_+}{N_-} = \exp(-\frac{g\mu_B B_z}{k_B T}). \tag{1.7}$$

The typical energy scale for $\Delta E = g\mu_B B_z$ (1 T) and $k_B T$ (100 K) is 5×10^{-6} eV and 10^{-2} eV. If we assume $g\mu_B B_z \ll k_B T$, we get:

$$N_- - N_+ \sim \frac{g\mu_B B_z}{k_B T} N_-. \tag{1.8}$$

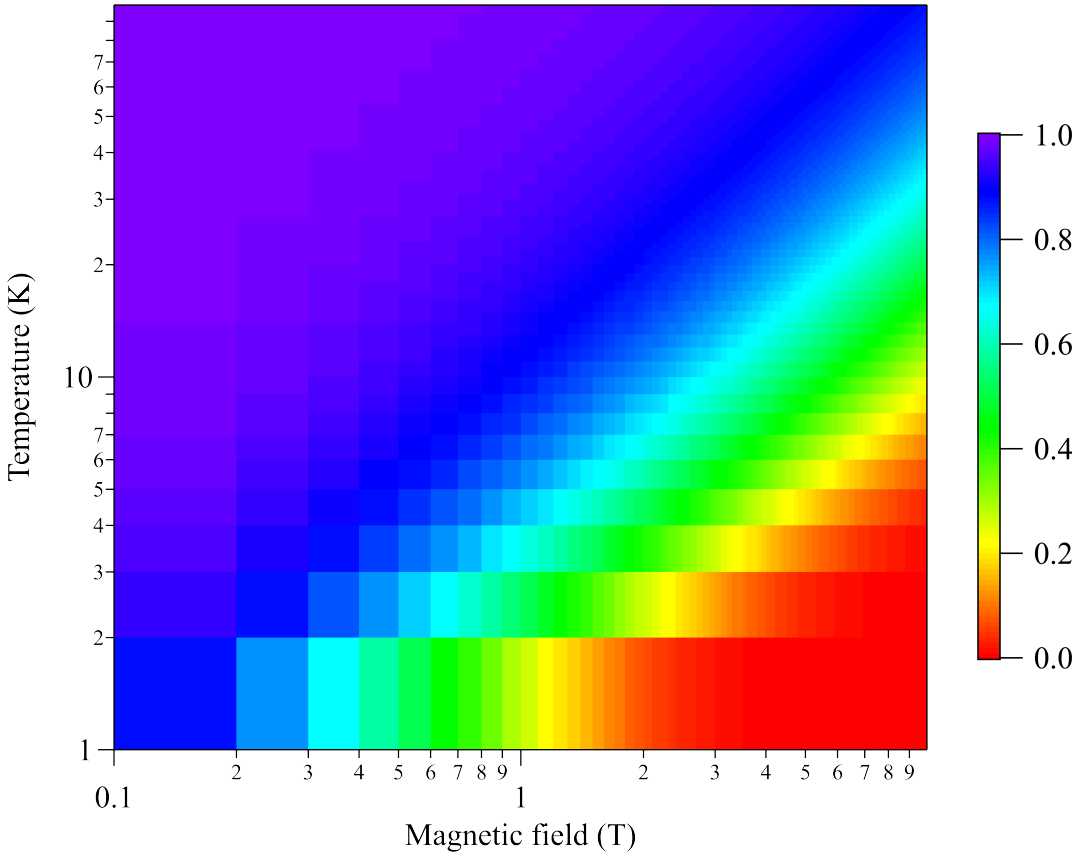

Figure 1.1: The population ratio of two-level system $\frac{N_+}{N_-}$ based on Boltzmann distribution. The x and y axis state different magnetic field and temperature.

Hence we can improve the spin polarization by either increasing external field **B** or lowering the temperature.

Unlike bulk measurements such as using a SQUID magnetometer, resonance measurements such as ESR reveal the local electron's properties, which can give insight into the electronic behavior. To be specific, the behavior of an electron spin S is controlled by its Hamiltonian:

$$H_{ESR} = H_{Zeeman} + H_{Quad} + H_{SS} + H_{SI}, \tag{1.9}$$

where Quad, SS and SI stand for electronic quadrupolar interaction, electron spin-spin

interaction and electron-nuclear spin interaction respectively [68]:

$$H_{Zeeman} = \mu_B \mathbf{B} \cdot \mathbf{g} \cdot \mathbf{S} \tag{1.10}$$

$$H_{Quad} = \mathbf{S} \cdot \mathbf{D} \cdot \mathbf{S} \tag{1.11}$$

$$H_{SS} = J \sum_{ij} \mathbf{S_i} \cdot \mathbf{S_j} \tag{1.12}$$

$$H_{SI} = \mathbf{S} \cdot \mathbf{A} \cdot \mathbf{I} \tag{1.13}$$

where $\mathbf{g}$ is the effective g-factor tensor, $\mathbf{D}$ is the electronic quadrupole tensor, $\mathbf{J}$ is the exchange constant, and $\mathbf{A}$ is the hyperfine coupling tensor. By studying ESR in certain materials, the information about these coupling parameters can be studied . These interactions lead to changes of resonance frequency, linewidth and lineshapes [41, 3]. ESR is widely used in biology, chemistry and physics.

1.2 Nuclei in solids

The nuclei in solids are rather more localized than electrons. They carry charge and are spatially confined, within a periodic ionic potential. Although they do not dominate most physical properties like electrons, they still have intrinsic magnetic moments:

$$\mu_{\mathbf{n}} = g_n \mu_n \mathbf{I}, \tag{1.14}$$

where g_n is the g-factor which varies for different isotopes and I is the nuclear angular momentum which is determined by the nuclear shell model [14].

The nuclear magneton $\mu_n = \frac{e}{2m_p c}$ is much smaller than Bohr magneton ($\frac{\mu_B}{\mu_n} = 1836.153$). Besides this, the other terms are the same as those of Eq. 1.1. Due to the Zeeman effect, the nuclear spin behavior should be the same as electron spin:

$$\mathcal{H}_{Zeeman} = \gamma_n \mathbf{I} \cdot \mathbf{B}, \tag{1.15}$$

where $\gamma_n = g_n \mu_n$ is the nuclear gyromagnetic ratio. Here we consider a nucleus with spin I = 1/2 and an external field $B = B_0 \hat{z}$. The energy levels can be written as:

$$\mathcal{E}_{\pm} = \pm \gamma_n B_z / 2 \tag{1.16}$$

$$\Delta\mathcal{E} = \gamma_n B_z \tag{1.17}$$

Similarly, the MW radiation can be absorbed if $h\nu_n = \Delta\mathcal{E}$. This phenomenon is called nuclear magnetic resonance (NMR). The macroscopic absorption rate is proportional to the spin polarization (Eq. 1.6), and the spin polarization can be approximate to be:

$$\mathcal{N}_- - \mathcal{N}_+ \sim \frac{\gamma_n B_z}{k_B T} \mathcal{N}_-, \tag{1.18}$$

where $\Delta\mathcal{E} = \gamma_n B_z$ (1 T) is about 10^{-7} eV. Due to the difference on magnetic moment, the nuclear spin polarization is roughly 1800 times weaker than electron spin polarization under same condition.

In general, nuclei as the center of ions behave as independent particles due to small magnetic moment and charge shielding from core electrons. Changes on the local magnetic environment will lead to changes on nuclear spin energy levels, which can be reflected in NMR spectroscopy.

The general nuclear spin Hamiltonian in a solid can be written as:

$$H_{NMR} = H_{Zeeman} + H_{Hyperfine} + H_{Quadrupole} + H_{Dipole}, \tag{1.19}$$

where H_{Zeeman} is the Zeeman interaction, $H_{Hyperfine}$ is the hyperfine interaction, $H_{Quadrupole}$ is the quadrupole interaction, and H_{Dipole} is the dipole interaction among nuclei. In the following sections, the hyperfine and quadrupole terms shall be introduced, as they are the most sigificant terms (in energy) that interact with local environments.

1.2.1 The hyperfine interaction

The interaction of a nucleus with the surrounding electrons is referred to as the hyperfine interaction and can be written as:

$$H_{hyperfine} = \mathbf{I} \cdot \mathrm{A} \cdot \mathbf{S}, \tag{1.20}$$

where $\mathcal{A}$ is the hyperfine coupling tensor which describes the strength and anisotropy of the coupling. This tensor can be broken down into dipolar, transferred, and contact terms. The contact term arises from unpaired s electron states which have a non-zero probability of being found at the nucleus. The transferred term arises when nearest neighbor orbitals hybridize with the s orbitals which in turn have wavefunctions that contact the nucleus. The dipolar term often dominates in insulator where electron magnets are localized and coupled to nuclear magnets via dipole field generation.

In metallic systems, the hyperfine interaction with the conduction electrons is known as the Knight shift. In insulating systems, the hyperfine coupling with ion electrons is called magnetic shift. For the second case, the dipole interactions create an effective local field at the nuclear site, which can be written as:

$$H_{onsite} = \gamma_n \mathbf{I} \cdot (\mathbf{B}_0 + \mathbf{B}_{local}) = \gamma_n \mathbf{I} \cdot (1 + \mathcal{K}) \cdot \mathbf{B}_0, \tag{1.21}$$

where $\mathbf{B}_0$ is the calibrated external field and $\mathcal{K}$ is the magnetic shift tensor which is defined as $\mathbf{B}_{local} = \mathcal{K} \cdot \mathbf{B}_0$. The magnetic shift is actually the sum of two contributions:

$$\mathcal{K} = \mathcal{K}_{\mathcal{L}} + \mathcal{K}_{\mathcal{S}}, \tag{1.22}$$

Here $\mathcal{K}_{\mathcal{L}}$ represents the contribution to the magnetic field seen at the nucleus due to the orbital susceptibility (the Van Vleck susceptibility) from unfilled shells. In many condensed matter systems, $\mathcal{K}_{\mathcal{L}}$ is temperature independent. The tensor $\mathcal{K}_{\mathcal{S}}$ represents

the contribution to the magnetic field due to the electronic spin susceptibility and usually is a function of temperature. In other words, if the electron local moment can be written as $\mathbf{M} = \mathbf{S} = \chi \cdot \mathbf{B_0}$, then it should obey:

$$\mathrm{B_{local}} = \mathcal{A} \cdot \mathbf{S} = \mathcal{K} \cdot \mathbf{B_0} \tag{1.23}$$

After cancelling $\mathbf{B_0}$, we find:

$$\frac{\mathcal{A} \cdot \chi}{g\mu_B} = \mathcal{K} \tag{1.24}$$

Therefore for insulating systems, the magnetic shift and electron spin susceptibility (without magnetic ordering) should exhibit a linear relation, and the ratio is determined by the hyperfine coupling. See Section 6.4 for more information on this relation.

1.2.2 The quadrupole interaction

For nuclear spins with $I \geq 1/2$, the quadrupole interaction describes the lowest order electrostatic coupling between electrons and nuclei. To be specific, for a point nucleus with a charge Ze, the electrostatic energy can be written as [1]:

$$W_E = \int\int \frac{\rho_e(r_e)\rho_n(r_n) d\mathbf{r_e} d\mathbf{r_n}}{|\mathbf{r_e} - \mathbf{r_n}|}, \tag{1.25}$$

where $\rho_e(r_e)$ and $\rho_n(r_n)$ are electron and nucleus charge distribution respectively (Born–Oppenheimer approximation is assumed). Using Laplace expansion of $1/|\mathbf{r_e} - \mathbf{r_n}|$, the energy can be rewritten as:

$$W_E = \sum_{l,m} A_l^m B_l^{m*}, \tag{1.26}$$

where

$$A_l^m = \int \sqrt{\frac{4\pi}{2l+1}} \rho_n(r_n) r_n^l Y_l^m(\theta,\phi) d\mathbf{r_n} \tag{1.27}$$

$$B_l^m = \int \sqrt{\frac{4\pi}{2l+1}} \rho_e(r_e) r_e^{-(l+1)} Y_l^m(\theta,\phi) d\mathbf{r_e} \tag{1.28}$$

For $l = 0$, the energy corresponds to electrostatic energy between point charges Ze, which is a uniform offset to all nuclear spins. For $l = 1$, the energy corresponds to interaction between nuclear electric dipole moment and electric field. Experimentally, the nuclear electric dipole moment is zero [87], hence this term does not exist. For $l = 2$, the energy corresponds to interaction between nuclear electric quadrupole moment and electric field gradient (EFG). To be exact, it can be written as:

$$H_{Quadrupole} = \sum_{m=-2}^{2} A_2^m B_2^{m*} = \sum_{j,k} Q_{jk} (\frac{\partial^2 V}{\partial x_j \partial x_k})_{r=0}, \tag{1.29}$$

where

$$Q_{jk} = \frac{eQ}{6I(2I-1)} (\frac{3}{2}(I_j I_k + I_k I_j) - \delta_{jk} I(I+1)) \tag{1.30}$$

is a traceless Cartesian tensor. If the coordinate axes are chosen so that the EFG tensor is diagonal:

$$(\frac{\partial^2 V}{\partial x_j \partial x_k})_{r=0} = \begin{pmatrix} V_{xx} & 0 & 0 \\ 0 & V_{yy} & 0 \\ 0 & 0 & V_{zz} \end{pmatrix}, \tag{1.31}$$

the quadrupole Hamiltonian becomes:

$$H_{Quadrupole} = \frac{\nu_c}{4}(3I_z^2 - I(I+1) + \eta(I_x^2 - I_y^2)), \tag{1.32}$$

where $\nu_c = \frac{eQV_{zz}}{I(2I-1)}$ and $\eta = \frac{V_{xx}-V_{yy}}{V_{zz}}$. We also utilize Laplace's equation that there is no electric charge near the nucleus: $V_{xx} + V_{yy} + V_{zz} = 0$.

As we can see, the information about the local electric field can be known by studying the quadrupole interaction. For example, one can measure the NMR spectra while rotating the sample. If the external field $\mathbf{B}_0$ does not lie along one of the principal axes of the EFG tensor, then the Hamiltonian becomes:

$$\begin{aligned} H_{Quadrupole}(\theta) &= \alpha\{I_x^2 V_{xx} + I_y^2(\cos^2\theta V_{yy} + \sin^2\theta V_{zz}) && (1.33)\\ &+ I_z^2(\cos^2\theta V_{zz} + \sin^2\theta V_{yy}) && (1.34)\\ &+ (I_y I_z + I_z I_y)\cos\theta\sin\theta(V_{yy} - V_{zz})\}, && (1.35) \end{aligned}$$

where $\alpha = \frac{eQ}{2I(2I-1)}$ and θ us the angle between $\mathbf{B}_0$ and the principal axis with the largest eigenvalue, V_{zz}. Assuming the quadrupole interaction is much smaller than the Zeeman splitting on the z direction: $\gamma_n B_z \gg \nu_c$, the quadrupole part can be treated as a first order perturbation. Taking $I = 1$ as an example, its energy levels at eigenstates become:

$$\begin{aligned} E_{+1} &= \gamma_n B_z + \frac{\alpha}{2}(\cos^2\theta V_{zz} + \sin^2\theta V_{yy}) && (1.36)\\ E_0 &= 0 - \alpha(\cos^2\theta V_{zz} + \sin^2\theta V_{yy}) && (1.37)\\ E_{-1} &= -\gamma_n B_z + \frac{\alpha}{2}(\cos^2\theta V_{zz} + \sin^2\theta V_{yy}) && (1.38) \end{aligned}$$

The NMR freqencies are:

$$\begin{aligned} f_+ &= E_{+1} - E_0 = \gamma_n B_z + \frac{3\alpha}{2}(\cos^2\theta V_{zz} + \sin^2\theta V_{yy}) && (1.39)\\ f_- &= E_0 - E_{-1} = \gamma_n B_z - \frac{\alpha}{2}(\cos^2\theta V_{zz} + \sin^2\theta V_{yy}) && (1.40) \end{aligned}$$

The splitting between two peaks is $2\alpha(\cos^2\theta V_{zz} + \sin^2\theta V_{yy})$. If the crystal has axial symmetry: $V_{xx} = V_{yy}$, then $V_{yy} = -\frac{V_{zz}}{2}$, and the splitting becomes:

$$\Delta f = 2\alpha(\cos^2\theta V_{zz} + \sin^2\theta V_{yy}) = \nu_c \frac{3\cos^2\theta - 1}{2} \quad (1.41)$$

In Section 6.4 we shall see that Eq. 1.41 also holds for spin $I = \frac{7}{2}$ systems.

1.3 Color centers in solids

Ideally, a crystal has perfect unit cell and the translation symmetry always holds. In practice, this is not always the case. One common types of defect is called a point defect, consisting of the absence of ions (or presence of extra ions). Such defects can profoundly alter a crystal's optical properties (and, in particular, their color) [4]. Fig. 1.2 shows different types of point defects in diamond and their color.

Sometimes substitution can lead to point defects, which may also unbalance the charge neutrality. It is also, however, possible to balance the charge with an electron localized in the vicinity of the point defect. Such an electron will have a spectrum of energy levels. Excitations between these levels produce a series of optical absorption lines analogous to those of isolated atoms. These kinds of defect-electron structures are known as color centers. Some recently studied color centers in semiconductors have been shown in Fig. 1.3.

In general, color centers have localized wavefunctions. Since the defect formation is just a minor change compared to the crystal lattice, the energy required to do so is rather small. Hence its energy level should be near the Fermi level E_f. Defect's electrons are ideal for ESR study, since they are localized with moderate energy scale, and the electrons are often unpaired with finite spin S.

1.4 Nitrogen vacancy centers in diamond

One types of color center we are particularly interested in, nitrogen–vacancy centers in diamond, have attracted broad attention as quantum sensors for both static and dynamic magnetic, electrical, strain, and thermal fields and are particularly attractive for quantum sensing, with wide-ranging application in the physical and life sciences

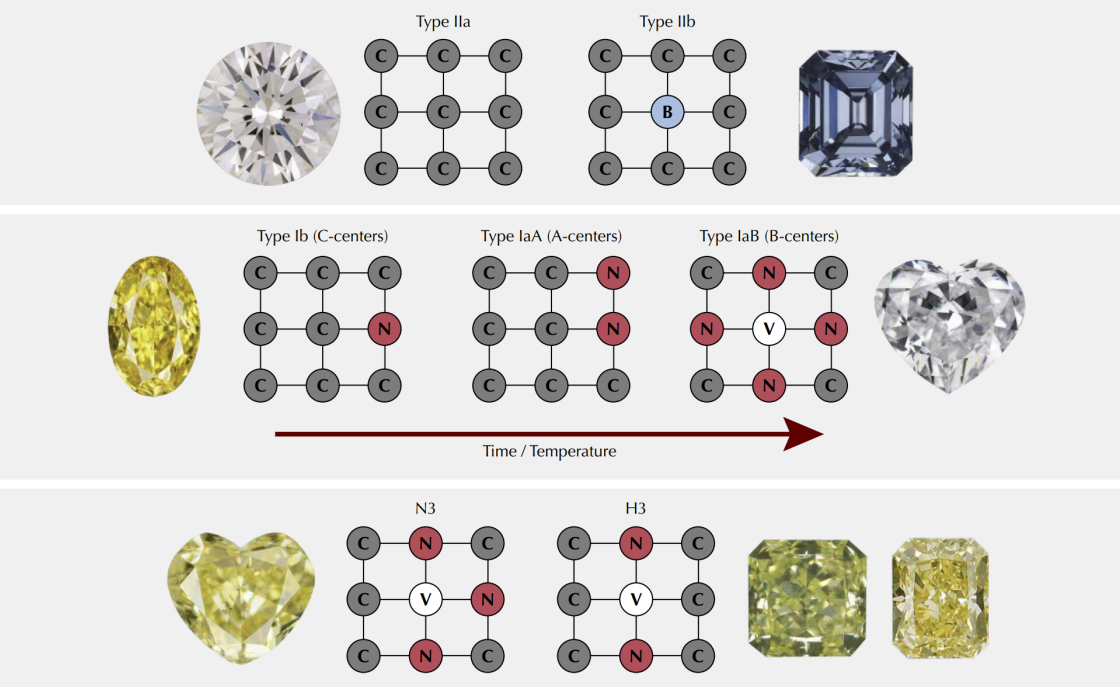

Figure 1.2: Atomic lattice defects cause different colors in diamond. Their configuration makes a significant difference in the color [13].

[24, 53, 16]. This color center consists of a vacancy adjacent to a nitrogen atom that replaces a carbon in the diamond structure. The defect center attracts an extra electron to have a net negative charge, so we abbreviate the center as NV^-.

Due to the tetrahedral bonding structure of carbon, there are four possible orientations of the nitrogen-vacancy axis:[111], $[\bar{1}\bar{1}1]$, $[\bar{1}1\bar{1}]$, and $[1\bar{1}\bar{1}]$ (Fig. 1.4(a)). The NV structure is constrained by the geometry of the diamond lattice to abide by C_{3v} symmetry (Fig. 1.4(b)). These symmetry properties in combination with six total electrons and various interactions give rise to a specific electronic structure.

1.4.1 Electronic states properties

The NV^- color center contains six electrons: five are from the nitrogen and the three carbons surrounding the vacancy and one from outside. As irreducible representations of the C_{3v} group, four orbital states a_1, $a_1^{'}$, e_x, and e_y can be formed, which are

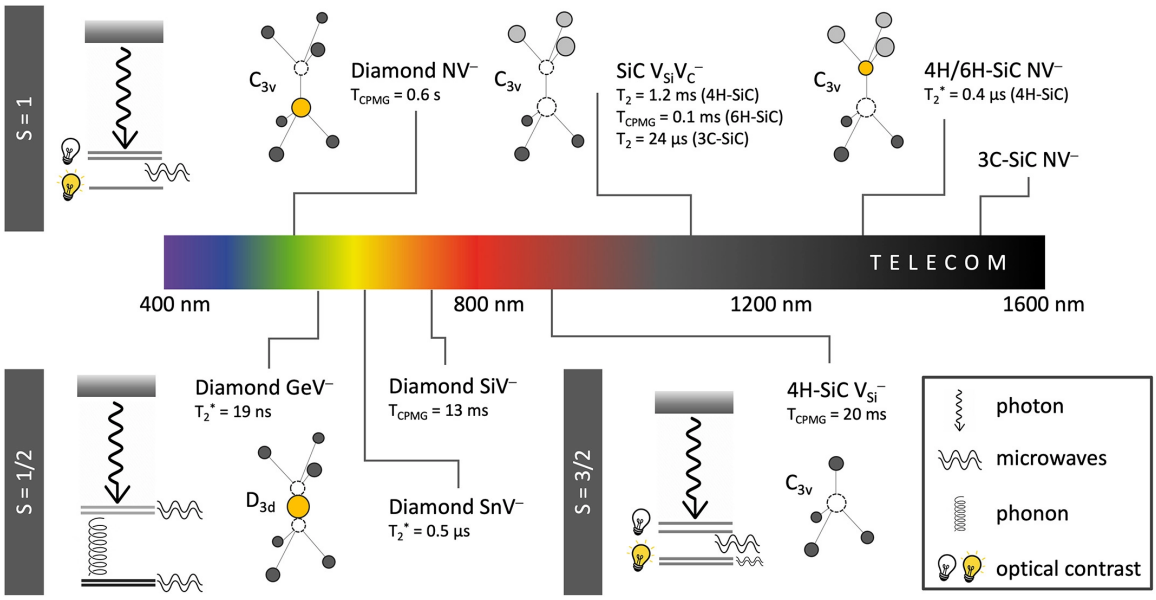

Figure 1.3: Prominently studied color centers in diamond and silicon carbide organized by the electron spin value which defines their energy scheme and associated interactions. The color centers are represented with their symmetry groups, crystal defect illustrations where yellow atoms represent foreign species and dashed outlines represent missing atoms, emission wavelength on the spectrum and the longest measured coherence times [62].

combinations of the four dangling bonds surrounding the vacancy (Fig. 1.5(a)).

In the ground state, the a_1 and $a_1^{'}$ states, which are lowest in energy, are filled by four electrons, as shown in Fig. 1.5(b). The remaining two electrons occupy the degenerate orbitals e_x and e_y. An antisymmetric combination of the orbital states minimizes the Coulomb energy and results in a spin-triplet ground state manifold:

$$\left|^3A_2\right\rangle = |E_0\rangle \otimes |m_S\rangle\,, \tag{1.42}$$

where $|E_0\rangle = |e_x e_y - e_y e_x\rangle$ indicates the orbital state has 0 angular orbital momentum and $|m_S\rangle$ represents electron spin $m_S = \pm 1, 0$ states. One comment on the ground states is that the electrons in the top energy levels are both unpaired, which is ideal for ESR studies.

The relevant excited state for the optical transitions of the NV center is a pair of

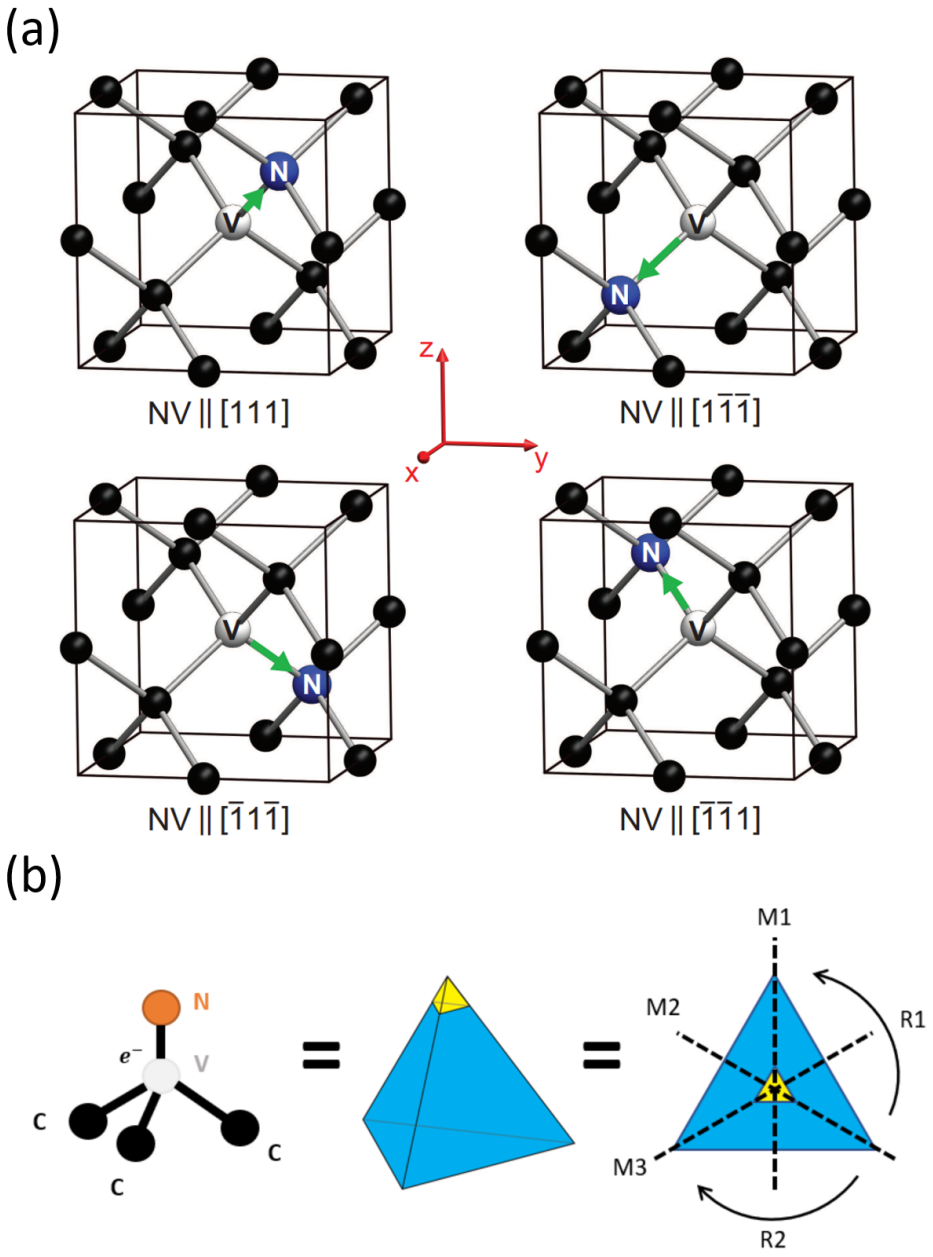

Figure 1.4: (a) Four orientations of the NV center in diamond. Carbon atoms are depicted in black, nitrogen (N) atoms in blue, and vacancies (V) in white. The NV electronic spin is indicated by green arrows[67]. (b) The NV has the same symmetries as a tetrahedron with a painted tip, or an equilateral triangle (restricted to 2-dimensional operations): reflections through mirror planes (M1, M2, M3), rotations by $\pm$ 120° (R1, R2), and the identity [59].

triplets which arises from the promotion of one of the electrons occupying the orbital a_1 to the e_x or e_y orbitals. By group theoretical analysis [54], a total of six states can be formed into two groups:

$$\left|^3E(m_S = \pm 1)\right\rangle = \begin{cases} |A_1\rangle \\ |A_2\rangle \\ |E_1\rangle \\ |E_2\rangle \end{cases} \tag{1.43}$$

$$\left|^3\mathrm{E}(m_S = 0)\right\rangle = \begin{cases} |E_x\rangle \\ |E_y\rangle \end{cases} \tag{1.44}$$

where these six energy levels are separated by spin-orbit and spin-spin interaction at the scale of GHz, which can all be excited by a 2.33 eV light. Since optical selection rules conserve the total angular momentum of the photon-NV center system, from now on we will only consider spin-conserving optical transitions.

1.4.2 Optical properties

One advantage of color centers is their optical absorption and emission are similar to isolated atoms, which is also the case for NV centers. The schematic energy levels of NV^- ground and excited states are shown in Fig. 1.6. The ground state $^3A_2$ and excited state ^3E are separated by a 637 nm zero-phonon line (ZPL), in the meantime the spin-spin interactions split the $|m_S = 0\rangle$ and $|m_S = \pm 1\rangle$ spin states to a zero-field splitting of $D_{gs} = 2.87$ GHz for the ground state and $D_{es} = 1.41$ GHz for the excited state. States $|^1A_1\rangle$ and $|^1E\rangle$ are excited states with $S = 0$, hence they cannot be reached by optical transitions.

At room temperature, the probability of electrons being at different m_S states is determined by the Boltzmann distribution: $\frac{p_{\pm 1}}{p_0} = \exp(-\frac{D_{gs}}{k_B T})$. Since $k_B T \gg D_{gs}$,

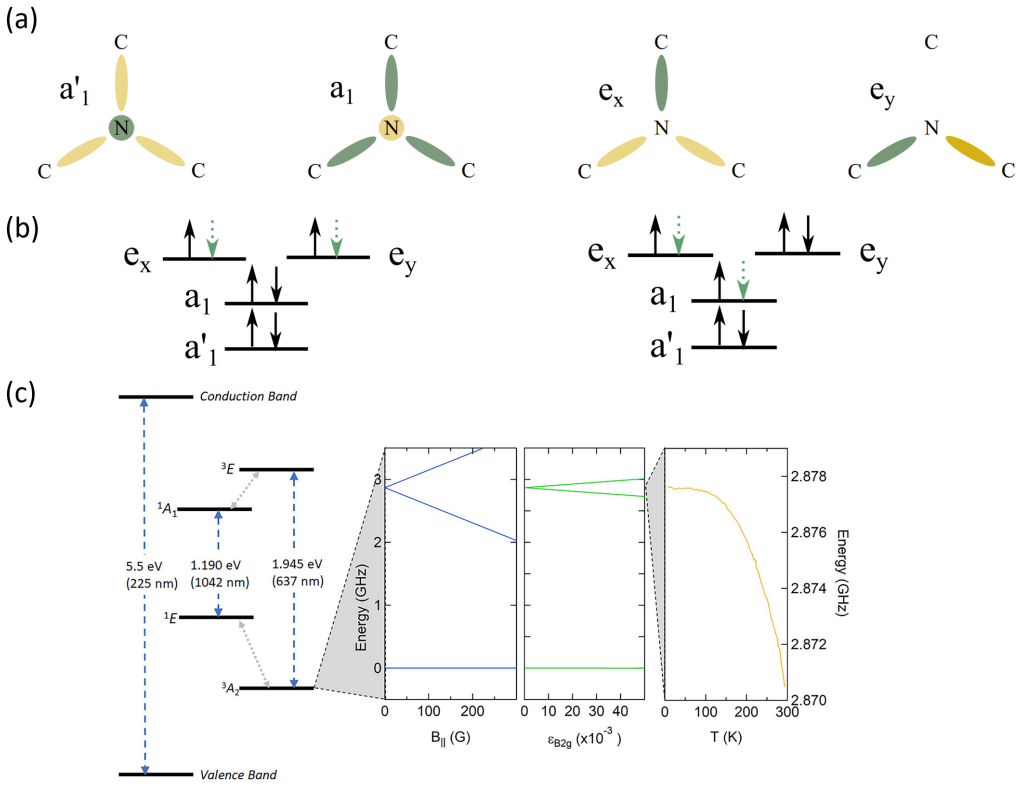

Figure 1.5: (a) Single electron orbitals of the NV center. The nitrogen and three carbons surrounding the vacancy are shown, and the perspective is along the NV axis. The color scale roughly represents the sign and occupation of each orbital. b) Ground states $^3A_2$ and excited states ^3E associated with the NV center's optical transitions. The four symmetrized states are filled by six electrons (black arrows), which can also be viewed as two holes (dashed arrows) [18]. (c) Energy levels of an NV^- center within the bandgap of the host diamond lattice. From left to right: the metastable singlet ground and excited state as a function of magnetic field (oriented parallel to the NV^- axis), anisotropic in-plane strain, and temperature. The temperature dependence has been magnified by a factor of 100 for clarity, indicated with green arrows [62].((a)(b) are reproduced from [18])

we find $p_{\pm 1} \sim p_0$, meaning electrons have equal probability to have different m_S values. With optical irradiation, $|^3A_2, 0\rangle$ will be excite to $|^3E, 0\rangle$ and $|^3A_2, \pm 1\rangle$ to $|^3E, \pm 1\rangle$ (with a smaller intensity [18]). After some time the excitations will decay and emit fluorescence at the ZPL (e.g. at 637 nm), which we can measure precisely. Although the radiative transitions between the $|^3A_2, 0\rangle$ and $|^3E, 0\rangle$ conserve electronic spin projection, there exists some spin non-conserving channels ($|A_1\rangle, |E_{1,2}\rangle \rightarrow |^1A_1\rangle$),

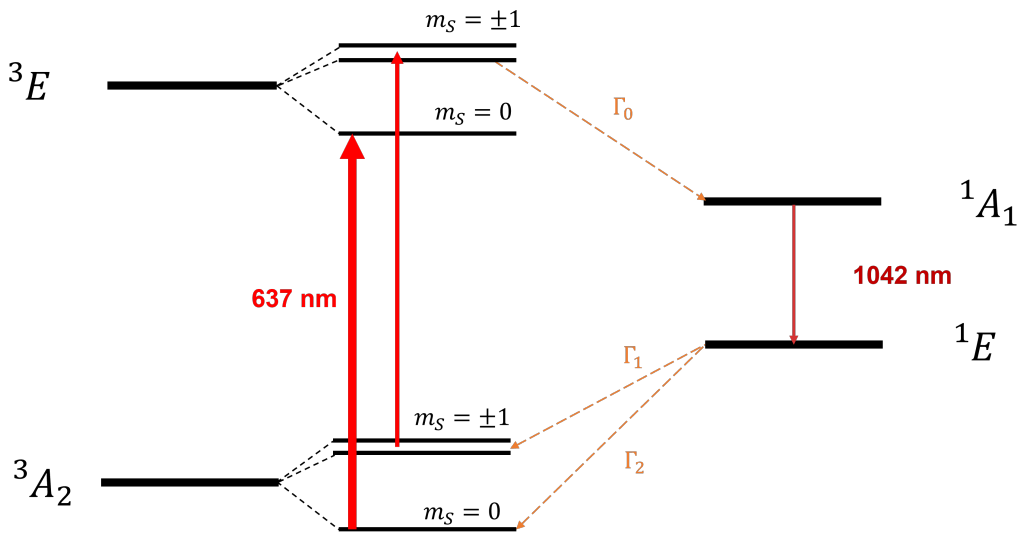

Figure 1.6: Schematic of the NV^- electronic structure including the $^3A_2$ and ^3E (room temperature) fine structure. The optical and infrared transitions are denoted by solid arrows and the spin non-conserving intersystem crossing (ISC) are denoted by dashed arrows [24, 34]

called intersystem crossings (ISC), that preferentially depopulates $|^3E, \pm 1\rangle$ into $|^1A_1\rangle$. Followed by a 1042 nm infrared decay, the $|^1A_1\rangle$ state shifts to $|^1E\rangle$ and eventually repopulates $|^3A_2, 0\rangle$ and $|^3A_2, \pm 1\rangle$ via ISC. The ratio of the ISC rates Γ_0, Γ_1, Γ_2 is roughly 53.3 : 0.98 : 0.73 and it varies between NVs [69, 80]. This whole ISC optical cycle takes a few hundred ns, which depopulates $|^3A_2, \pm 1\rangle$ due to ISC channel between $|^3E, \pm 1\rangle$ into $|^1A_1\rangle$.

After a few μs of optical irradiation, the ISC optical cycle already happens dozens of times, which can almost depopulate all the electrons in $|m_S = \pm 1\rangle$. Often, polarization can be in range of $80-90\%$ [69]. Taking 85% as average, we can convert the ratio into temperature using Boltzmann distribution, which is $T_{eff} \sim 0.31$K. Therefore, a well polarized initial state $|m_S = 0\rangle$ can be easily prepared at room temperature by optical pumping.

Another outcome of the ISC optical cycle is spin dependent fluorescence. As show in Fig. 1.7, when the state is prepared in $|^3A_2, 0\rangle$, no ISC will be involved – all the

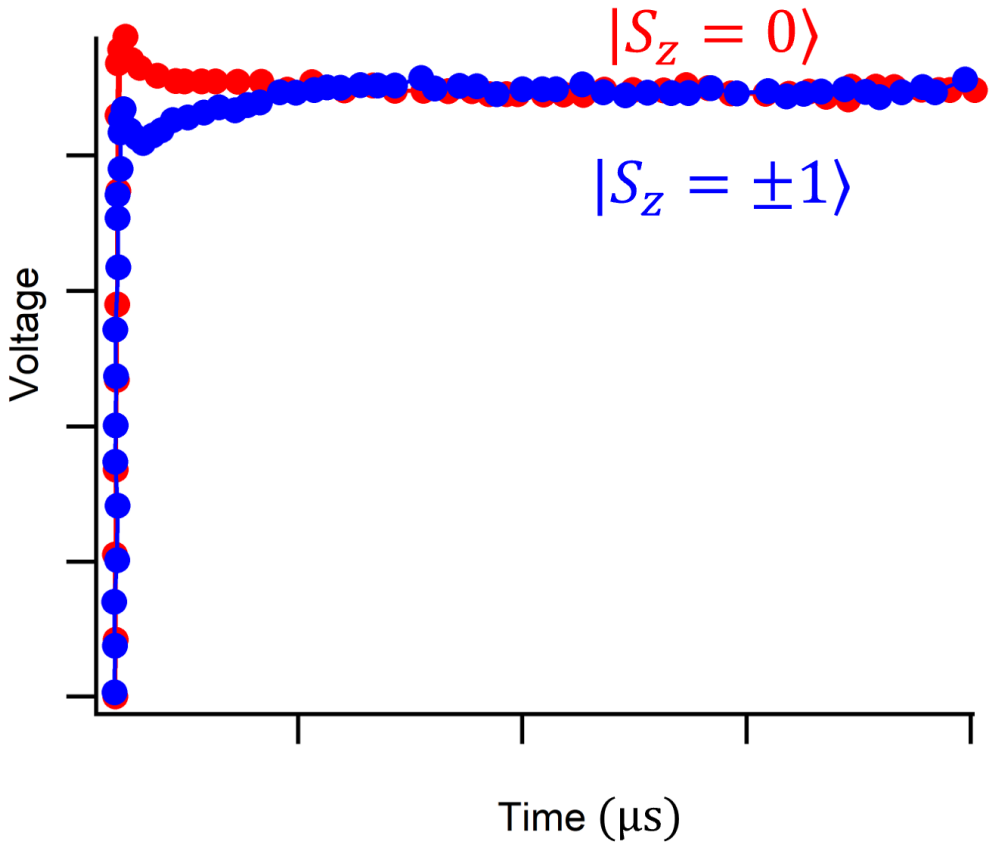

Figure 1.7: Examples of the time-dependent fluorescence I_ms for pure initial spin states ($m_S = 0, \pm 1$). The contrast in the fluorescence of the pure spin states is demonstrated in different colors (reproduced from [24])

states will emit 637 nm fluorescence; when the state is prepared in $|^3A_2, \pm 1\rangle$ (see next section), ISC will play a very important role which results in a lower intensity of the 637 nm fluorescence and more 1042 nm infrared emission. Hence by readout of the fluorescence intensity, the population ratio between $|0\rangle$ and $|\pm 1\rangle$ can be measured.

1.4.3 Optical detected magnetic resonance

In a magnetic field, the Hamiltonian of NV^- ground state electrons can be written as:

$$H_{NV^-} = DS_z^2 + \gamma_e \mathbf{B} \cdot \mathbf{S}, \tag{1.45}$$

where $D = 2.87\text{GHz}$ is the zero-field splitting between $|0\rangle$ and $|\pm 1\rangle$ and $\gamma_e = g\mu_B$ is the gyromagnetic ratio of electron. If the field is aligned along the NV axis: $\mathbf{B} = B_z\hat{z}$, the energy levels of three spin states are:

$$E_{+1} = \gamma_e B_z + D \tag{1.46}$$

$$E_0 = 0 \tag{1.47}$$

$$E_{-1} = -\gamma_e B_z + D \tag{1.48}$$

If there is MW radiation that matches $f_- = -\gamma B_z + D$ or $f_+ = -\gamma B_z + D$, the electron spin can move from $|0\rangle$ to $|\pm 1\rangle$ and the MW energy will be absorbed, which is the basic idea of ESR.

For the NV system, however, if the MW radiation matches $f_\pm$, the electrons will be moved to the $|^3A_2, \pm 1\rangle$ states, which takes ISC optical cycle and exhibit lower fluorescence output. In other words, by sensing the decay of fluorescence, one can determine the resonance frequency. This method is called optical detected magnetic resonance (ODMR).

One advantage of ODMR over ESR is that the optical sensing is much easier, whereas ESR is usually detected by observing a resonant cavity. The most straightforward application of NV ODMR is as a magnetometer – the splitting between two resonance frequencies, $\Delta f = 2\gamma B_z$, is proportional to the field intensity. In fact, we use NV centers as magnetometer to calibrate our magnets (see Section 2.2.3).

There are two broad approaches to NV ODMR: single site and ensemble measurements. The major difference between them is that single NV always have two resonance frequencies, whereas ensemble NV measures Avogadro's number of sites, which consists of four different orientations. Each orientation will have a different angle with the external field, therefore ensemble NV ODMR often has eight peaks,

indicating two transitions for each orientation (Fig. 3.2).

1.4.4 Strain effects

Using group theory [39], the first-order linear perturbation to the electronic states of a trigonal defect (NV^-) within a cubic crystal (diamond) due to stress can be understood. The NV^- Hamiltonian with mechanical-spin interaction can be written as:

$$H_{NV^-S} = (D_0 + \mathrm{M_z})S_z^2 + \mathrm{M_x}(S_x^2 - S_y^2) + \mathrm{M_y}(S_xS_y + S_yS_x) + \gamma_e \mathbf{B}\cdot\mathbf{S}, \tag{1.49}$$

where D_0 is the zero field splitting under ambient condition. $\mathrm{M_z}$, $\mathrm{M_x}$ and $\mathrm{M_y}$ refer to[8]:

$$\mathrm{M_z} = a_1(\sigma_{XX} + \sigma_{YY} + \sigma_{ZZ}) + 2a_2(\sigma_{YZ} + \sigma_{ZX} + \sigma_{XY}) \tag{1.50}$$

$$\mathrm{M_x} = b(\sigma_{XX} + \sigma_{YY} - 2\sigma_{ZZ}) + c(\sigma_{YZ} + \sigma_{ZX} - 2\sigma_{XY}) \tag{1.51}$$

$$\mathrm{M_y} = \sqrt{3}b(\sigma_{XX} - \sigma_{YY}) + \sqrt{3}c(\sigma_{YZ} - \sigma_{ZX}) \tag{1.52}$$

After diagonalizing the Hamiltonian, the energy levels of NV^- exhibit two distinct effects: one translates both transitions by $\mathrm{M_z}$; another splits transitions by $\sqrt{{\mathrm{M_x}}^2 + {\mathrm{M_y}}^2}$.

If we assume the pressure is normal to the cubic surface and no shear stress is

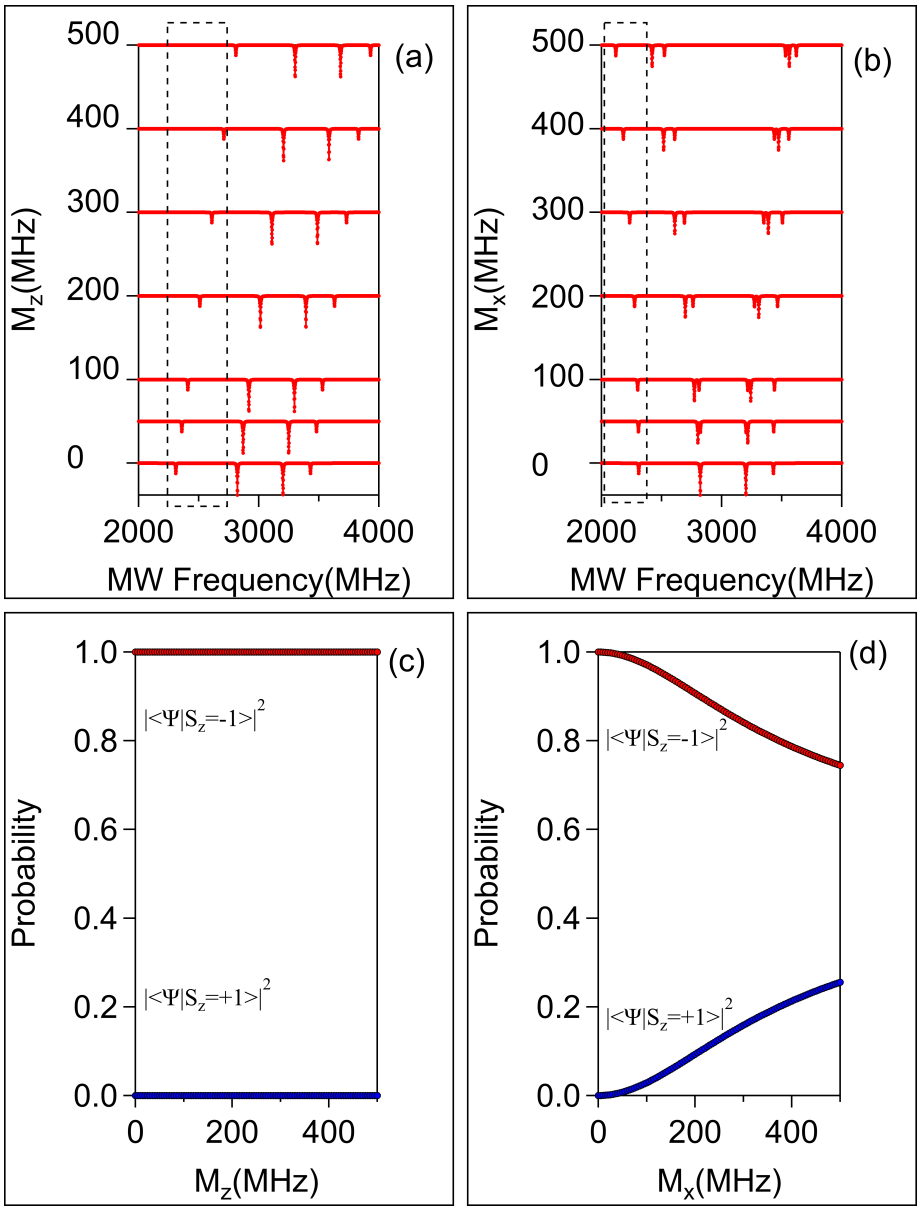

Figure 1.8: (a)(b) Calculated NV^- electron spin resonance (ESR) spectra dependence on strain component M_z and M_x;(c)(d) Calculated proportion of lowest energy transition (highlighted in dashed box) as M_z and M_x increases. As we can see, M_z does not effect the in-parallel NV^-'s transition proportion, which corresponds to hydrostatic pressure case. Meanwhile M_x tend to mix $|S_z = -1\rangle$ and $|S_z = +1\rangle$ together, which is a signature of shear stress. It is worth to note that mixing states also occur when the bias field B is misaligned from NV^-'s axis.

involved – $\sigma_{ij} \neq 0$ if and only if $i = j$, M_i (i = x,y,z) can be simplified as:

$$M_z = a_1(\sigma_{XX} + \sigma_{YY} + \sigma_{ZZ}) \quad (1.53)$$

$$M_x = 0 \quad (1.54)$$

$$M_y = 0 \quad (1.55)$$

These assumptions are reliable when the pressure is not extreme, where the pressure in the DAC is still quite hydrostatic (It might fail at Mbar pressure[38, 21]). Nevertheless, the hydrostatic pressure on NV^- will mostly contribute to the common shift, $\omega_{CM} \sim M_z$, which is shown in Fig. 1.8(a).

If the applied strain is pure shear strain – $\sigma_{ij} \neq 0$ if and only if $i, j = x, y$, then:

$$M_z = 2a_2\sigma_{XY} \quad (1.56)$$

$$M_x = -2c\sigma_{XY} \quad (1.57)$$

$$M_y = 0 \quad (1.58)$$

The shear strain not only contributes to common shift ω_{CM}, but also generates differential shift ω_{DF}, which is shown in Fig. 1.8(b). Besides, the shear strain will mix $|S_z = -1\rangle$ and $|S_z = +1\rangle$ together (Fig. 1.8(d)), which will reduce the fluorescence (FL) contrast. This might explain the signal intensity decay in the high pressure regime[21].

1.5 Pulsed magnetic resonance

The above mentioned magnetic resonance techniques, including ESR, NMR, and ODMR, require a continuous-wave (CW) MW. Under CW radiation, a non-thermal equilibrium polarization is reached and some MW energy is absorbed. In the 1970s, pulsed (FT) NMR was developed, which has become the most widely used magnetic

Experimental methods	detecting signal	Receiver
Electron spin resonance	Spin magnetization	High frequency resonator
Nuclear spin resonance	Spin magnetization	MW coil
Optical detected magnetic resonance	Fluorescence	Photodiode

Table 1.1: Various pulsed magnetic resonance methods and their detecting signals

resonance technique.

The basic idea of pulsed magnetic resonance (MR) is as follows: after a net polarization between energy levels is initialized, a short pulse at the resonance frequency is applied, which perturbs the polarization from equilibrium. A detection occurs immediately after the radiation (various detection method for different magnetic resonance has been stated in Table 1.1). After the perturbation, the system will relax to equilibrium over time.

There are two major advantages of pulsed MR:

1. Better signal to noise ratio (SNR). By repeating measurement cycles N times and signal averages, the effective SNR should increase as $\sqrt{N}$.

2. Extracting dynamical information. During CW MR, the information one can get comes mostly from the spectra, which renders resonance frequencies and lineshape. These quantities describe static properties of the local environment. For pulsed MR, one can also measure polarization changes as it relaxes back to equilibrium. These relaxation processes contain dynamical properties of the local environment (see next section).

1.5.1 Rotating frame

For a two level system (also called qubit), if we assume the MW pulses happen during $0 < t < t_{MW}$, then its Hamiltonian during that time is:

$$H_{Qubit-MW}(t) = \gamma S_z B_0 + \gamma B_1(\cos(\omega_{rf}t + \phi)S_x + \sin(\omega_{rf}t + \phi)S_y), \tag{1.59}$$

where the S_i's are spin 1/2 operators, γ is the gyromagnetic ratio of the spin, H_0 is the static magnetic field intensity, and H_1, ω_{rf}, and ϕ are the intensity, frequency, and phase of the MW pulse respectively.

We assume the initial state density matrix is $\rho_0 = |0\rangle\langle 0|$, indicating a perfect polarization in the lowest energy state. If we apply a unitary transformation:

$$U = \exp(-i\omega S_z t), \tag{1.60}$$

the transformed Hamiltonian (in the so-called rotating frame) becomes:

$$\begin{aligned} \tilde{H}_{Qubit-MW} &= U^\dagger H_{Qubit-MW} U + i\frac{\partial U^\dagger}{\partial t} U \\ &= (\gamma B_0 - \omega) S_z + \gamma B_1 (\cos((\omega_{rf} - \omega)t + \phi) S_x \qquad (1.61) \\ &+ \sin((\omega_{rf} - \omega)t + \phi) S_y) \qquad (1.62) \end{aligned}$$

If $\omega = \omega_{rf}$, the Hamiltonian becomes time-independent:

$$\tilde{H}_{Qubit-MW} = \gamma \mathbf{B}^{'} \cdot \mathbf{S} \tag{1.63}$$

where the effective field $\mathbf{B}^{'}$ is:

$$\begin{aligned} B_x^{'} &= B_1 \cos(\phi) \\ B_y^{'} &= B_1 \sin(\phi) \qquad (1.64) \\ B_z^{'} &= B_0 - \omega_{rf}/\gamma \end{aligned}$$

Consider the magnetization, defined as $\mathbf{M} = \mathrm{Tr}(\rho \mathbf{S})$, in the laboratory frame. Initially it is along the z-direction. The MW field $\mathbf{B}_{mw} = B_1 \cos(\omega_{rf} t + \phi)\hat{x} + B_1 \sin(\omega_{rf} t + \phi)\hat{y}$ rotates around the z axis with angular frequency ω_{rf}. If we choose a reference frame that is rotating along the z axis at frequency ω_{rf}, then the MW field

in the new frame is static. If the MW is on resonance: $\omega_{rf} = \gamma B_0$, the magnetization will rotate along the MW field direction, which causes $\mathbf{M}$ to change direction. This is the reason why this unitary transformation U is called the rotating frame.

Solving the time-independent Hamiltonian in the rotating frame, then transforming it back to the laboratory frame, one can get a two-level wavefunction at $0 < t < t_{MW}$ $(S = 1/2)$:

$$
\begin{aligned}
|\Psi_l(t)\rangle &= U^{\dagger} |\Psi_r(t)\rangle && (1.65)\\
&= U^{\dagger} \exp(-i\gamma \mathbf{B}^{'} \cdot \mathbf{S}t) |\Psi(0)\rangle && (1.66)\\
&= \begin{pmatrix} e^{-i\omega_{rf}t/2}(\cos(\Omega t/2) - \frac{iB_z^{'}\sin(\Omega t/2)}{B^{'}}) \\ e^{i\omega_{rf}t/2}\frac{(-iB_x^{'}+B_y^{'})\sin(\Omega t/2)}{B^{'}} \end{pmatrix}, && (1.67)
\end{aligned}
$$

where $\Omega = \gamma B^{'}$ and $B^{'}$ denotes the intensity of the effective field given in Eq. 1.64.

In practice, $\omega_{rf} \gg \Omega$. Sometimes the dwell time δt during the measurement can be relatively long such that $\delta t \sim \frac{2\pi}{\Omega} \gg \frac{2\pi}{\omega_{rf}}$, hence the exponential phase from U is not affecting the wavefunction: $e^{i\omega_{rf}t/2} \sim const$. In such case we can consider that the measured system is already in the rotating frame [64]. More discussion on two level systems and the double quantum rotating frame can be found in Section 3.3 and 5.2.

1.6 Relaxation process

1.6.1 Bloch equation

If we consider the density matrix for an $S = 1/2$ system, the Liouville equation describes the time evolution:

$$\frac{\partial \rho}{\partial t} = -i[H, \rho], \tag{1.68}$$

where:

$$\rho = \begin{pmatrix} \rho_{00} & \rho_{01} \\ \rho_{10} & \rho_{11} \end{pmatrix} \tag{1.69}$$

Defining unitless magnetization $\mathbf{M} = \mathrm{Tr}(\rho\mathbf{S})$, it turns out that Eq. 1.68 can be rewritten as a differential equation of $\mathbf{M}$ [76]:

$$\begin{aligned} M_x &= \gamma(\mathbf{M} \times \mathbf{B})_x \\ M_y &= \gamma(\mathbf{M} \times \mathbf{B})_y \\ M_z &= \gamma(\mathbf{M} \times \mathbf{B})_z, \end{aligned} \tag{1.70}$$

which is also known as the Bloch equations [11]. The magnetization defined here is proportional to the bulk magnetization, so these describe macroscopic behavior of spins under magnetic field.

In fact Eq. 1.70 pictures the ideal case where a single spin is isolated. In a real system due to the spin-spin interaction and spin-lattice interaction, the magnetization can be strongly effected by the local environment. The Bloch equations also include relaxation terms:

$$\begin{aligned} M_x &= \gamma(\mathbf{M} \times \mathbf{B})_x - \frac{M_x}{T_2} \\ M_y &= \gamma(\mathbf{M} \times \mathbf{B})_y - \frac{M_y}{T_2} \\ M_z &= \gamma(\mathbf{M} \times \mathbf{B})_z - \frac{M_0 - M_z}{T_1}, \end{aligned} \tag{1.71}$$

where T_1 is the spin-lattice relaxation time, T_2 is the spin-spin relaxation time, and $M_0 = \chi_0 B_0$ is the initial nuclear magnetization in equilibrium.

Here T_1 describes the time scale for magnetization M_z to relax to equilibrium M_0, and T_2 describes the time scale for magnetization in the plane, $M_{x,y}$, to decay to

0. These variables are only phenomenological parameters, and do not elaborate the specific relaxation mechanisms.

1.6.2 T_1 relaxation

T_1 describes the decay of the magnetization component $M_z(t)$, and $M_z(t)$ is determined by the population at each energy levels. The total nuclear spin Hamiltonian can be defined as:

$$H = H_0 + H_1(t), \tag{1.72}$$

where H_0 is the static terms such as Zeeman interaction and quadrupolar interaction, and $H_1(t)$ takes into account local environment fluctuations [79]. Defining $\mathbf{P}(t)$ as the population vector of the different energy levels with $\mathbf{P}(0)$ being the equilibrium value, the population time evolution can be understood as a master equation:

$$\mathbf{P}(t) = \mathbb{W}(\mathbf{P}(t) - \mathbf{P}(0)), \tag{1.73}$$

where $\mathbb{W}$ is the relaxation matrix, which in second-order perturbation is given by [1]:

$$W^{\alpha\beta}(\alpha \neq \beta) = \int_{-\infty}^{\infty} d\tau \exp(i\omega_{\alpha\beta}\tau)\overline{\langle\alpha| H_1(\tau) |\beta\rangle \langle\beta| H_1(0) |\alpha\rangle} \tag{1.74}$$

$$W^{\alpha\alpha} = -\sum_{\alpha\neq\beta} W^{\alpha\beta}, \tag{1.75}$$

where $|\alpha\rangle$, $|\beta\rangle$ are eigenstates of H_0 and $\omega_{\alpha\beta} = \langle\alpha| H_0 |\alpha\rangle - \langle\beta| H_0 |\beta\rangle$ are transition frequencies. Ensemble averages are denoted by $\overline{\langle\cdots\rangle}$.

In short, the relaxation rate between energy levels is controlled by fluctuations that can flip the energy levels. There are two typical fluctuations able to achieve this: fluctuating magnetic fields which couples $|n\rangle$ to $|n \pm 1\rangle$ and fluctuating EFGs which couples $|n\rangle$ to both $|n \pm 1\rangle$ and $|n \pm 2\rangle$. The relaxation matrices originated

from these two fields can be written as:

$$
\begin{aligned}
W_m^{\alpha\beta}(n \to n+1) &\sim \frac{\gamma^2}{2}\int_0^\infty (\langle h_x(\tau)h_x(0)\rangle + \langle h_y(\tau)h_y(0)\rangle)e^{-\omega_{\alpha\beta}\tau}d\tau \\
W_{Q1}^{\alpha\beta}(n \to n+1) &\sim (eQ)^2\int_0^\infty \langle V_{+1}(\tau)V_{-1}(0)\rangle e^{-\omega_{\alpha\beta}\tau}d\tau \\
W_{Q2}^{\alpha\beta}(n \to n+2) &\sim (eQ)^2\int_0^\infty \langle V_{+2}(\tau)V_{-2}(0)\rangle e^{-\omega_{\alpha\beta}\tau}d\tau,
\end{aligned}
\tag{1.76}
$$

where $H_{x,y}(t)$ are fluctuating magnetic field in plane components, and $V_{1,2}(t)$ component of the fluctuating EFG in the basis of spherical harmonics (Eq. 1.28). The total relaxation is the combination of the three: $\mathbb{W} = \mathbb{W}_m + \mathbb{W}_{Q1} + \mathbb{W}_{Q2}$ [79, 82].

Utilizing the fluctuation-dissipation theorem [42], the correlations in Eq. 1.76 can be linked to the imaginary part of the Fourier transform of the susceptibility $\mathrm{Im}\chi(\omega)$. The spin-lattice relaxation rate is given by [61]:

$$
T_1^{-1} = \gamma^2 k_B T \lim_{\omega\to 0}\sum_{\mathbf{q}} |F(\mathbf{q})|^2 \frac{\mathrm{Im}\chi(\mathbf{q},\omega)}{\omega}, \tag{1.77}
$$

where $F(\mathbf{q})$ is the form factor which is the Fourier transform of the hyperfine coupling and $\mathbf{q}$ is the wave vector summed over Brillouin zone. See more discussion about T_1^{-1} in Section 6.5.1.

1.6.3 T_2 relaxation

T_2 (T_2^*) relaxation describes decay of the in plane magnetization $M_{x,y}$. In quantum language, the state of a two-level system:

$$
|\psi\rangle = \frac{1}{\sqrt{2}}(|0\rangle + e^{i\phi}|1\rangle) \tag{1.78}
$$

is strongly related to the macroscopic magnetization. The decay of $M_{x,y}$ can be understood as losing coherence in the quantum level. Naively, the loss of coherence

can happen in two ways: bit flip between $|0\rangle$ and $|1\rangle$, and phase variation [22]. Using Redfield theory, if the fluctuating source is pure magnetic field, the T_2 of the system can be written in terms of T_1 [74]:

$$\frac{1}{T_2} = \frac{1}{2T_1} + \gamma^2 S_{zz}(0), \tag{1.79}$$

where $S_{zz}(0)$ is the correlation of magnetic field in z direction $h_z(t)$. In this equation, the first term is flipping the states and the second term is varying the phase.

What we also can learn from Eq. 1.79 is that T_2 is often much shorter than T_1 due to the phase varying term. In order to extend T_2, in other words extend the coherence, it is important to secure the phase. Different methods such as spin echo, dynamical decoupling and spin-locking are developed in order to achieve this. The upper bound of T_2 should be in the same order as T_1. See more details for extending coherence in Section 3.6.

Chapter 2

Experimental methods

In order to sense nearby environment using NV^- centers in diamond, a quantum diamond spectrometer with certain resolution and sensitivity is required. In this chapter, the details about spectrometer constructions and development will be presented, including that for ambient pressure and GPa pressure in a diamond anvil cell (DAC). The conventional NMR cryogenic system will also be introduced.

2.1 NV diamond samples

We employed two sets of NV^- diamond crystals. Sample A is from the Pines lab in UC Brekeley. It is a type Ib [100] diamond which is grown by HPHT methods from SUMITOMO (it usually contains nitrogen defects from 10 to 100 ppm), and then it is irradiated with electrons at 3 MeV, with a fluence of 10^{18} cm^{-2} [5]. The NV concentration is typically in the range of 100 - 500 ppm. Its T_2 measurement is displayed in Fig. 2.1(a).

Sample B is DNV-B1 from element six. It is a [100] CVD grown diamond with much fewer NV concentration – about 300 ppb. Its typical T_2 at ambient condition

Sample	A	B
growth method	HPHT	CVD
NV^- concentration	100 $\sim$ 500 ppm	0.3 ppm
T_2	0.8 μs	85.1 μs

Table 2.1: NV diamond sample A vs B

is displayed in in Fig. 2.1(b). The modulation on the decay is due to the AC signal generated by ^{13}C nuclear spin under bias field – its frequency is $\gamma_{^{13}C}H_0$. More details about T_2 will be discussed in chapter 3.6.

In order to utilize the NV diamond inside a DAC, it needs to be reshaped down to μm size. Thus we asked Delaware Diamond Knives to cut a 100 μm part then polish down to about 20 μm for both A and B samples. The film can then be broken down to smaller chips so as to fit them into the gasket hole, which is usually in the order of 150μm.

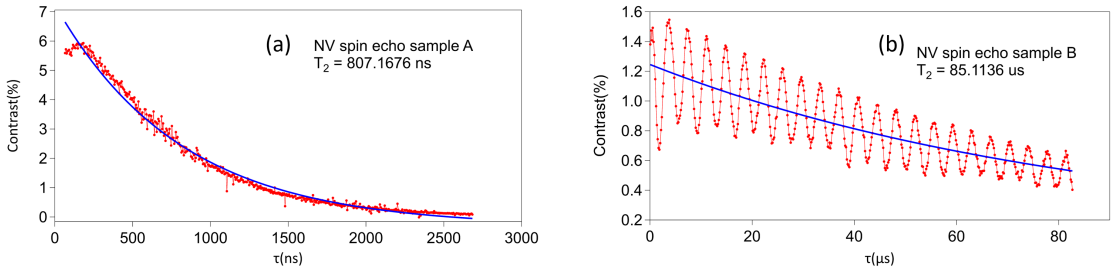

Figure 2.1: (a) The spin echo contrast vs τ for sample A. The curve does not have modulated oscillation might because decoherence is dominating by NVs interaction; (b) The spin echo contrast vs τ for sample B. The T_2 is about 100 times longer and curve has modulated oscillation corresponding to AC magnetic field generated by ^{13}C spins in the diamond lattice at 250 Gauss.

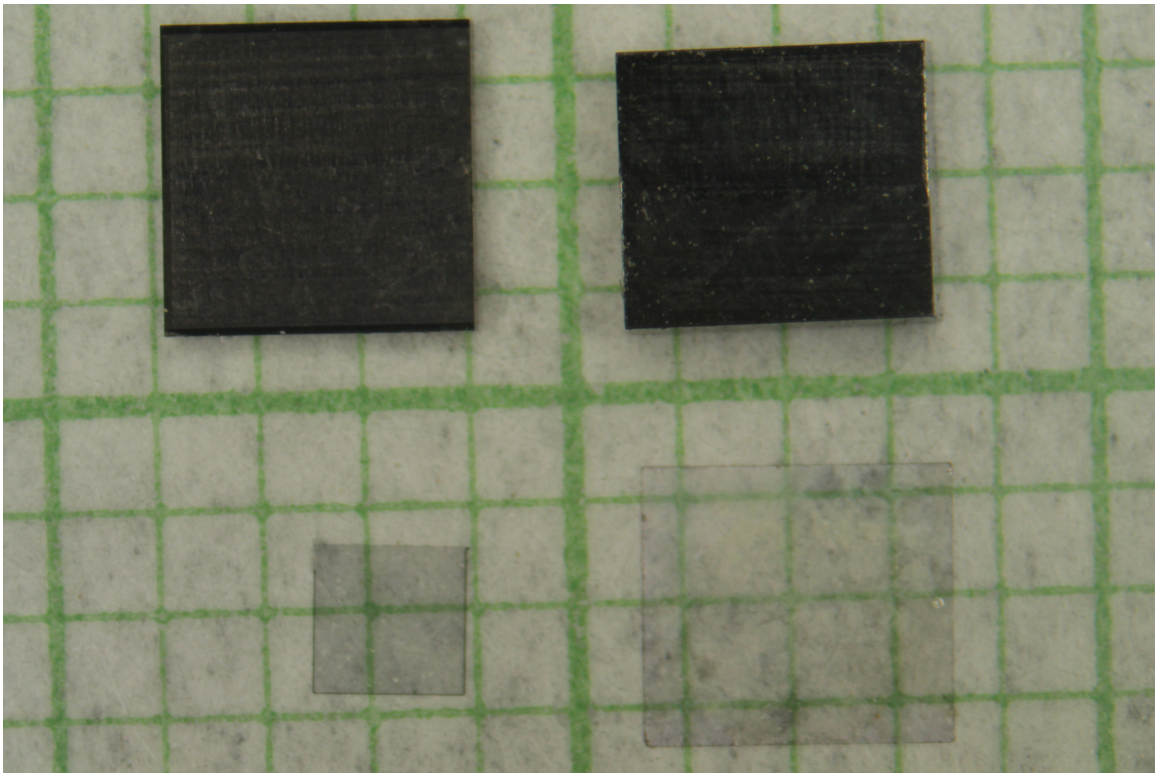

Figure 2.2: Top left: HPHT hundreds ppm diamond; Top right: CVD 300 ppb diamond; the look becomes darker after the laser cut(it is possible that extra NVs are generated during the cutting process); Bottom left: diamond chip cut from HPHT diamond; Bottom right: diamond chip cut from CVD diamond.

2.2 NV center quantum spectrometer for ambient pressure

The first version of NV diamond quantum spectrometer is adapted from the previous continuous-wave(CW) quantum spectrometer with lock-in techniques[78]. The improvements include a stable floating optical table, a powerful solid state laser and synchronization between light, microwave(MW) and data acquisition. The schematic diagram is shown in Fig. 2.3.

Optical setup

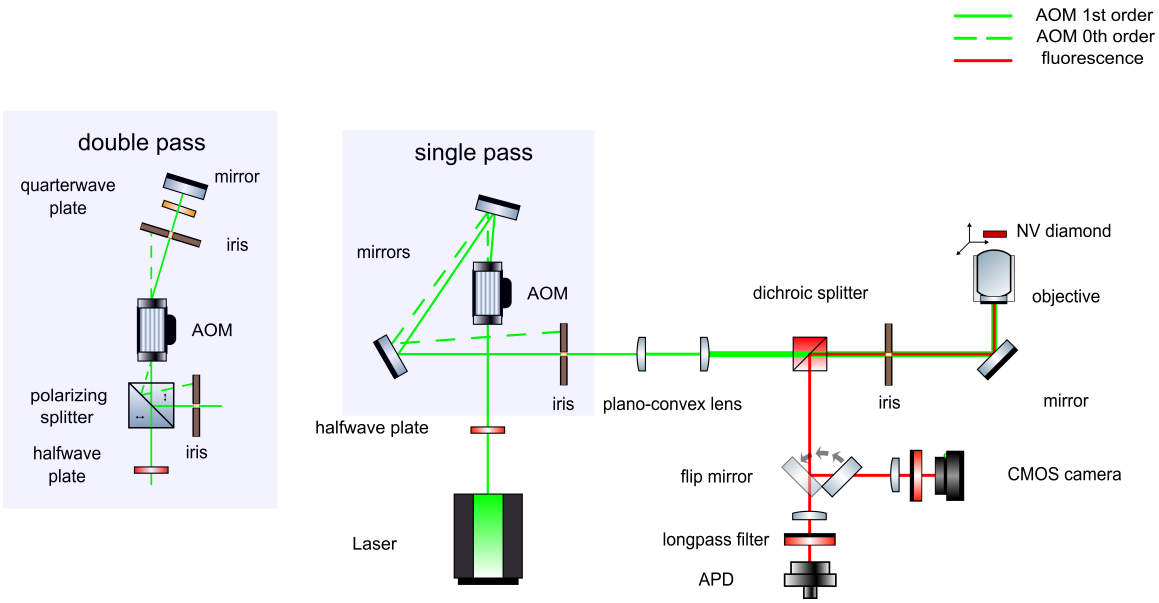

Figure 2.3: Schematic of NV center quantum spectrometer. Note that the light paths for both zero and first order of AOM are shown, and only the first order light can pass onto collimation and detection. The two setups in blue box are exchangeable. The NV sample and antenna are mounted on a translation stage.

2.2.1 Optical system

The whole system is constructed on Newport research series plus optical table. The 500 mW solid state laser (GEM 532 Novanta Photonics) and aluminum heat sink is mounted on an adjustable lab jack(Newport Lab jack 271). The outcome light from laser module is already linear polarized. The direction of polarization vector $\vec{A_0}$ is controlled by a 1" half wave plate (HWP Thorlabs WPH10M-532) on a rotating mount (Thorlabs RSP1). To be specific, the HWP has perpendicular fast and slow axes. The projection onto fast axis stays unchanged while projection onto show axis has an extra π phase introduced by the HWP. As a result, the angle between incident light and output light is 2θ, where θ is the angle between $\vec{A_0}$ and the fast axis (Fig. 2.4). Afterwards, the beam passed through an Acousto-Optic Modulator (ISOMET

M1201-SF40-1.7 AOM) which is driven by a 40 MHz MW driver (ISOMET 521C-2 RF Driver).

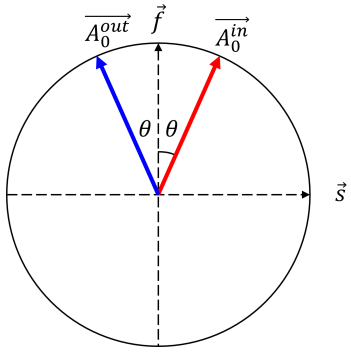

Figure 2.4: The in plane view of HWP and laser beam incident and output polarization vector $\vec{A_0^{in}}$ and $\vec{A_0^{out}}$. Here $\vec{f}$ and $\vec{f}$ denote the HWP's fast and slow axis respectively.

The purpose of the AOM is to turn on and off the beam freely. The AOM is a device that uses the acousto-optic effect to diffract light using sound waves. A piezoelectric transducer is attached to glass in the device. The driver creates an oscillating electric signal to vibrate the glass, which generates sound waves in the material. These can be thought of as moving periodic planes of expansion and compression that change the index of refraction. Incoming light scatters off the resulting periodic index modulation and interference occurs similar to Bragg diffraction like in Fig. 2.5. To angle the device properly, the incoming beam and the glass interface should be perpendicular and off by the Bragg angle(for our AOM it is about 3 mrad). When the device is misaligned, one usually can observe diffraction pattern up to the 4th order; when the device is aligned, most beam power is in the 0th and one of the 1st orders.

There are two ways to set up the AOM: one way is passing the device once – after two 1" kinetic mirrors' reflection, the 0th and 1st order beams will be distinguishable;

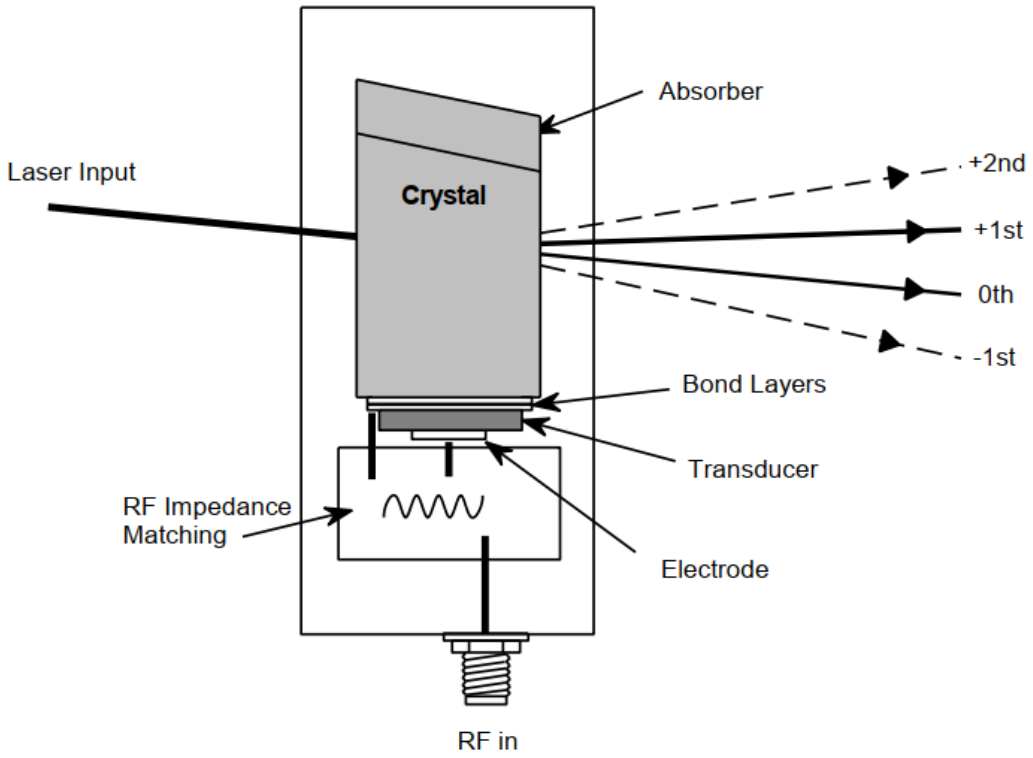

Figure 2.5: AOM schematic plot (Reproduced from ISOMET manual)

another way is passing the device twice – the 1st order will be reflected backwards so that it is the new incoming light. As a result, the second 1st order will be distinguishable and also its polarization is rotated by 90 degrees after passing the quarter wave plate(Thorlabs WPQ10M-532) twice. Eventually the beam will be reflected by the polarizing plate beamsplitter (Thorlabs PBSW-532).

The advantage of double-pass is it increases the on/off contrast of the fluorescence signal. The AOM is not perfect, so there will have slight amount of residue light on the 1st order even when the driving has not been applied. The power of residue light I_1 linearly depending on the incoming light I_0: $I_1 = r\ I_0$. For double-pass, since the beam passes the AOM twice, the final residue light will be $I_1 = r^2\ I_0$. This improve-

ment on residue light can be crucial when the laser power is relatively large and NV concentration is relatively high – the residue light can interact with the NVs during the dark time.

After the AOM, the beam will next be collimated and aligned onto the pupil of the objective lens (Nikon M Plan 100x ELWD). For collimation purpose there are two plano-convex lens with different focal length (Thorlabs LA1131-A and LA1951-A) – the beam will be expanded. A shearing Interferometer(Thorlabs SI035) is used to check the collimation. Since Rayleigh length of the Gaussian beam out of the laser is not long enough to cover the whole optical system, it is important to collimate the beam before it enters the objective. As for expansion, it is better to let the beam cover the whole pupil area instead of cover part of it – It pushes the resolution down to the diffraction limit.

The NV sample usually sits on a transparent platform (cover glass for example) which is mounted on a translation stage (Newport ESP300) whose actuator (Newport 850G-LS) has encoder resolution 7.985 nm. Therefore it allows us to locate the sample precisely within about 1 μm.

The fluorescence emitted by NVs in diamond is collected by the same objective, sharing the same light path as the green laser until it reaches the dichroic mirror (Edmond optics 69-216). Fluorescence will be directed and focused either to the CMOS camera (Thorlabs DCC1545M) or the avalanche photodetector (Thorlabs APD120A2/M APD) controlled by a flip mirror (Thorlabs FM90). Longpass filters (BLP01-594R-25 EdgeBasic) are used to block the residual green light.

2.2.2 Microwave delivery

The MW signals to control NVs in the diamond are generated by an 6Gs/s arbitrary waveform generator (Tabor SE5082 AWG). The output signal is sent to an 16 Watts amplifier (mini circuits ZHL-16W-43-S+), an circulator (Pasternack PE83CR1004) to avoid the reflected power back to the amplifier and finally the antenna (Fig. 2.6).

A simple MW 'antenna' (MW transmitter) could be a copper wire connecting between center and ground of an SMA connector or a PCB strip with a hole in the middle (Fig. 2.7). The one we usually use is a copper strip electroplating onto a cover glass. The pattern consists of two straight line and a loop at the end. A male SMA connector is attached to straight lines by the sliver epoxy. A female SMA wall mount is attached on the translation stage so that the antenna can be connected onto the stage freely.

Unlike in conventional NMR, the tank circuit is fine tuned to the target resonance frequency using capacitors, here the circuit impedance Z at target frequency is much greater than 50 Ω so that the reflection coefficient

$$\rho = \frac{Z - 50\Omega}{Z + 50\Omega} \tag{2.1}$$

is almost 1, which means most of the power has been lost during the transmission. Still the residual MW power is able to generate 5 MHz Rabi power and higher, which is sufficient for control the NVs for our purpose.

2.2.2.1 Higher harmonics generation

All kinds of dynamical decoupling (DD) sequences are generated by AWG during the experiment. AWG can read user defined waveforms – usually a discrete array of

signal levels, then it can convert the digital input into analog output by interpolating between those signal levels. The interpolation depends on the sampling mode.

In order to create different phases in the MW pulses, there must be enough sampling points in one period of the signal. One way to achieve this is generate higher harmonics. Technically, the output of AWG contains multiple harmonics from different Nyquist zones and the target harmonics output is usually weaker than signal in the first Nyquist zone. Hence a bandpass filter (mini circuits VBF and VBFZ series) and a pre-amplifier (mini circuits ZX60-53LN+) are applied to select the desired Nyquist zone and also increase the power. The filtered and boosted signal will then be transmitted to the 16 Watts amplifier.

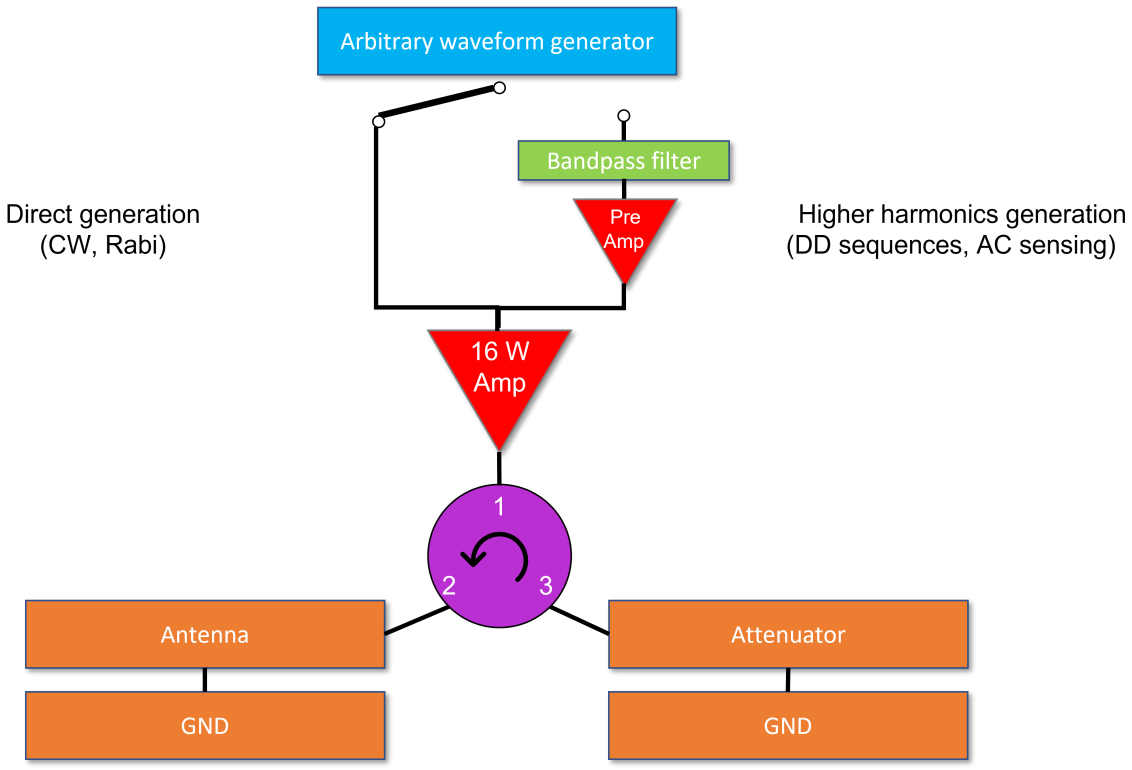

Figure 2.6: MW delivery schematic plot

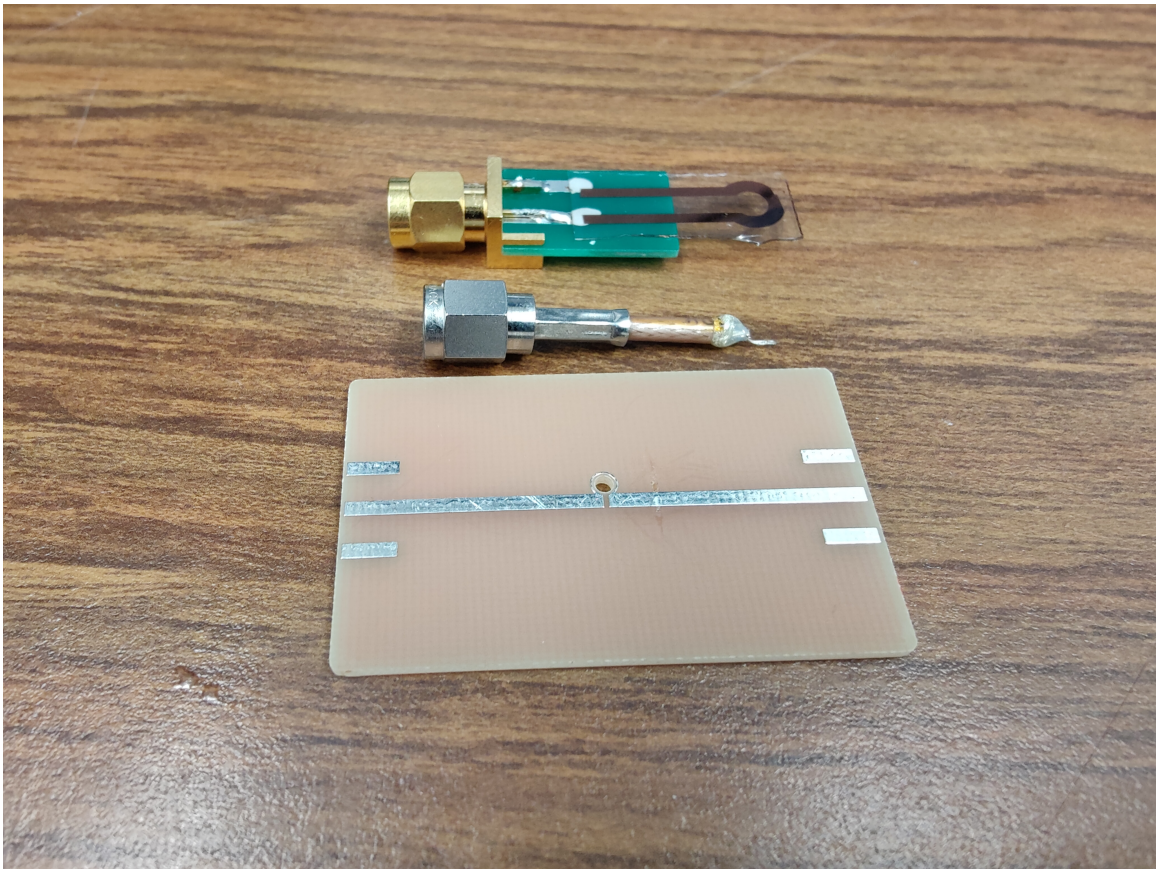

Figure 2.7: three possible antennas to deliver MW. Top: a electroplating copper structure on the cover glass is connected to a PCB which has a soldered SMA connector. Middle: A wire loop connecting between center and ground shield of a coaxial cable. Bottom: A specially made PCB with a loop and hole

2.2.3 Static field generation

A static magnetic field is applied so as to separate one of the NV- orientations from the other three in the spectra (details are discussed in 3.2). The field needs to be applied parallel to one of the NV^-' orientations – [111] for an example, where the angle between the field direction and the z axis of the NV diamond is $\theta_{NV} = 54.74°$. Since the NV^-'s gyromagnetic ratio is quite large (28025 MHz/T), the NV^-"s energy level will have a significant response to field in the order of Gauss. The field range for our system is 10 to 300 Gauss.

2.2.3.1 Electromagnet

One way to apply the field is to use an electromagnet. We constructed a special mount from aluminum to meet the right angle of the field – a copper coil is held in the mount aligned with the NV axis (Fig. 2.8(a)). The whole mount is surrounded by cooling water to dissipate the heat (Fisher). The current in the coil is controlled by a 600 Watt DC power supply (FAST-PS 3020-600).The mount sits on the objective so that the NV diamond will be at the most homogeneous region of the field (Fig. 2.8(b)). The resulting field measured by NV continuous wave (CW) spectra depends linearly on the current. The field can be tuned continuously from 5 to 60 Gauss (Fig. 2.8(c)). It is challenging to increase the current further since the cooling power reaches its threshold. Besides, the cooling power is fluctuating especially with big current (¿ 15 A), which renders unstable coil temperature and magnetic field.

2.2.3.2 Permanent magnet

Another way to apply the field is using permanent magnets, which have stable magnetic field properties. Neodymium magnets are chosen because they are inexpensive and easily available. Similar to the electromagnet we constructed, a special mount 3D printed to align the field with the NV axis – magnets can be stacked in the hole on each side (Fig. 2.9(a)). The 1" disc magnets (Mcmaster-Carr 5862K Fig. 2.9(b)) with thickness ranging from $\frac{1}{16}''$ to $\frac{1}{2}''$ can generate static field from 50 to 300 G approximately (Fig. 2.9(c)). Though easy to manipulate, field from permanent magnet is not as homogeneous as that from the electromagnet. The field also cannot be tuned continuously.

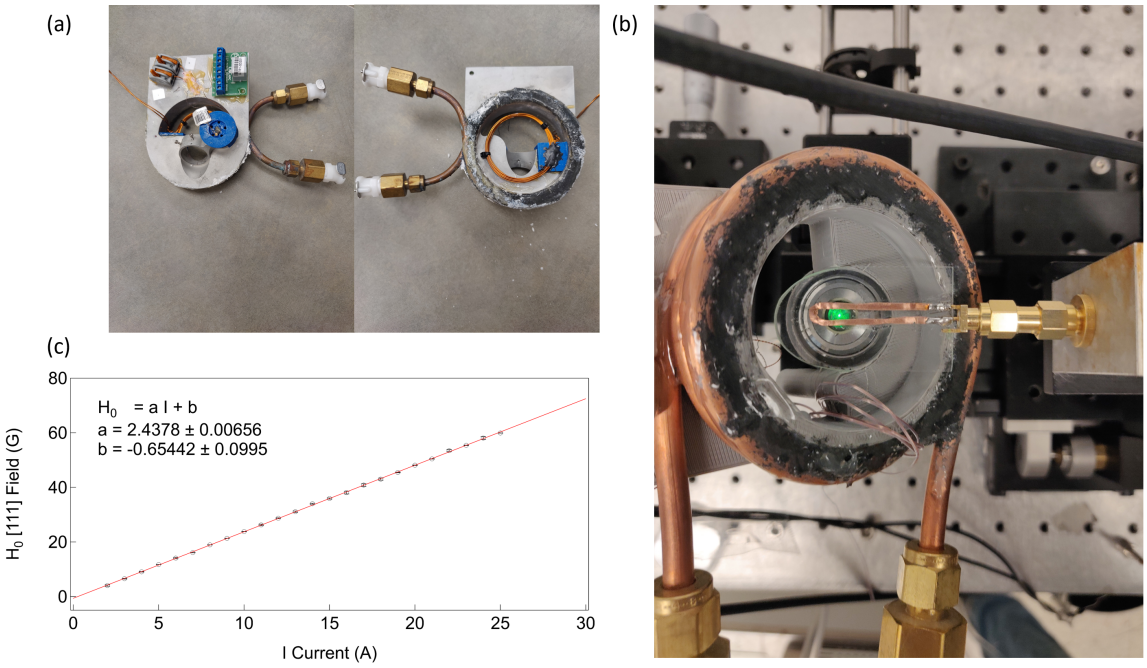

Figure 2.8: (a)The electric magnet structure: conducting wire is wrapped around an aluminum mount with a special angle. The cooling water is running in a copper tube outside of the coil. A Hall sensor and a test coil is also attached to the mount. (b)The magnet mount is in align with objective and antenna. (c)The field intensity measured by NV CW spectra fit vs applied current on the coil.

2.2.4 Fluorescence signal process

The fluorescence intensity varies with different NV samples. To be specific, the Silicon Avalanche photodetector we are using has a minimum detecting power P_{RMS} as 1.5 nW, which is $n_{min} = P_{RMS}/h\nu = 4.0 * 10^9$ photons per second. Assumptions are the following: (a) all the NVs under the objective focus are responsible for the signal contrast and the laser power is strong enough to saturate all of them; (b) the lifetime of the excited state Γ^{-1} is 10 ns; (c) the branch ratio to the dark state P_{dark} is 0.3; (d) The focusing volume V_f is about 1 μm^3. Then the NV photon density can be written as:

$$n_{NV} = \frac{\Gamma P_{dark} \rho_{NV} V_f}{4}, \tag{2.2}$$

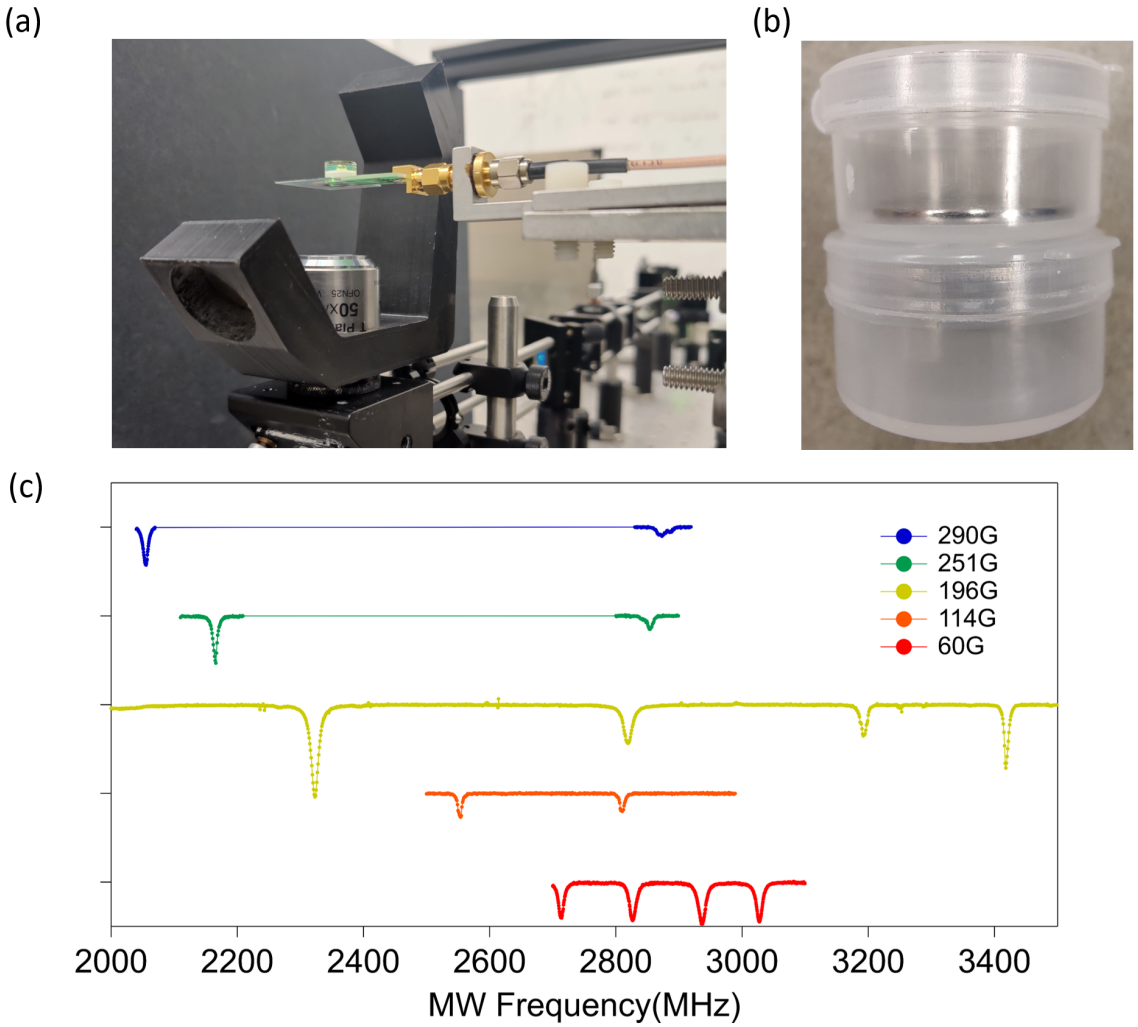

Figure 2.9: (a)The 3D printed magnet mount in align with objective and antenna. The mount has two cylinders to load permanent magnets. (b)The 1" diameter and $\frac{1}{16}$" thickness cylinder Neodymium magnets (c)NV CW spectra vs different permanent magnets

The factor of $\frac{1}{4}$ accounts for one out of four orientations. The minimum detectable NV density ρ_{min} can be reached when $n_{NV} = n_{min}$. The calculation shows $\rho_{min} = 7.0{*}10^{14}$ cm^{-3}, which is also 4.0 ppb ($\rho_C = 1.76 * 10^{23}$ cm^{-3}).

Likewise, the maximum detectable power P_{max} is 1.5 μW, which corresponds to NV density 4.0 ppm. Considering the NV density of our samples, the APD has no problem to detect sample A and B except for sample A it needs a neutral-density

filter (Thorlabs NE10A-A) to avoid the saturation.

The output of APD is a voltage signal ranging from few mV(RMS noise) to few Volts. This time dependent analog voltage can be observed via oscilloscope directly, or it can be converted into digital signal via a data acquisition card (National instrument USB-6361 DAQ) which is necessary to measure the fluorescence temporally.

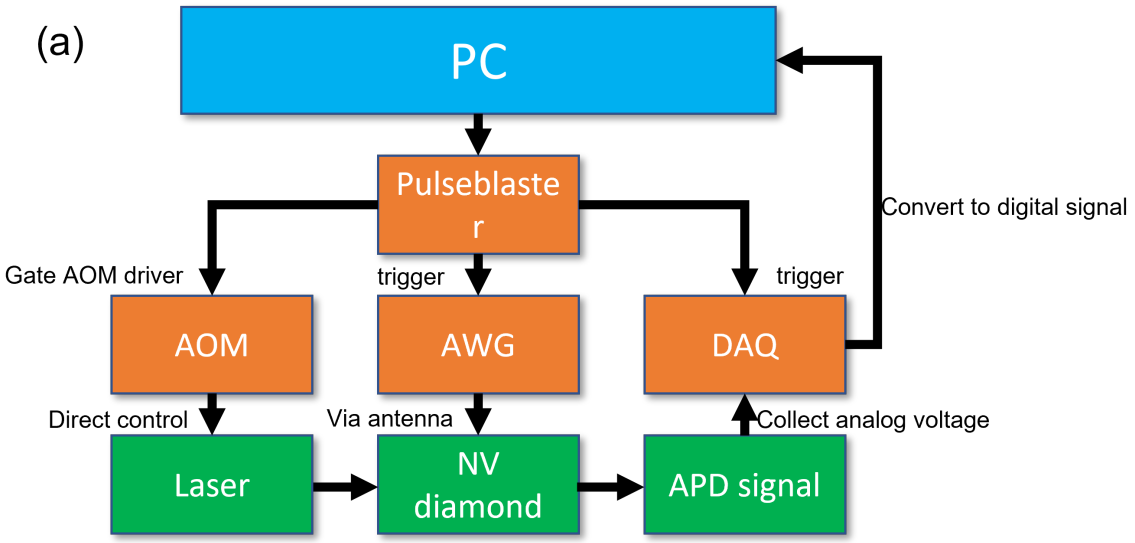

Figure 2.10: Synchronization control schematic diagram

2.2.5 Synchronization control

The basic of AC field detection is controlling the NV spin temporally, which requires the synchronization between laser excitation, MW sequence control and fluorescence voltage readout. A schematic diagram is shown in Fig. 2.10(a). The AOM driver, AWG and DAQ require proper trigger signals, hence the timing is governed by a third trigger source – a TTL trigger board (Spincore PBESR-PRO-300 pulseblaster). As the heart of the timing control, the shortest the pulse TTL board can generate is

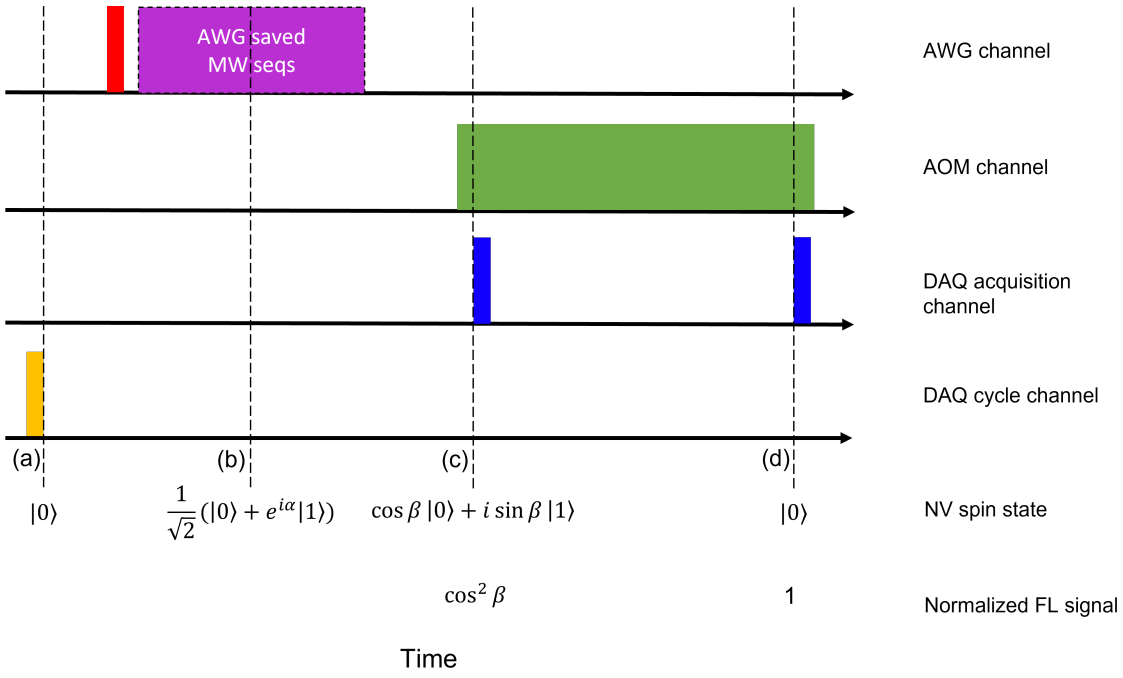

Figure 2.11: Triggers controlled by TTL trigger board. Ideally, the NVs are initialized to $|0\rangle$ at the beginning. After AWG is triggered, the pre-programmed MW sequence will transform the state into superposition state $\frac{1}{\sqrt{2}}(|0\rangle + e^{i\alpha}|1\rangle)$ (α is a certain phase during the MW manipulation). Before shining the green laser the final state is $\cos\beta\,|0\rangle + \sin\beta\,|1\rangle$. Utilizing the laser pump, the fluorescence can be detected and it contains information about final phase β. By the end of the laser pulse, NVs are re-initialized to $|0\rangle$ ready for the next cycle. The timing in the plot is schematic.

$\frac{1}{\Omega_{clock}} = 3.333$ ns. In the meantime, it has multiple channels which can be programmed in the same time.

A typical measurement sequence consists of four channels: AOM channel, AWG channel, DAQ channel and DAQ cycle channel. The first trigger is the DAQ trigger to count the number of cycles; after that the AWG is triggered to output a pre-programmed MW sequence; lastly there is the AOM gate to shine green light upon the NV diamond both for measuring spin states and re-polarizing them back to the ground states. Meanwhile two DAQ triggers are high at the beginning and the end of the laser gate. The two voltages V_{spin} and V_{laser}, which give ratio $\frac{V_{spin}}{V_{laser}}$, represent the NV population on the ground state $|\langle 0|\psi\rangle|^2$ after and before MW manipulations.

One cycle takes tens of μs and one measurement usually takes tens of thousands of cycles. A standard cycle is displayed in Fig. 2.11).

2.3 NV diamond quantum spectrometer for a diamond anvil cell

After constructing and demonstrating the NV diamond quantum spectrometer in ambient conditions, the system was upgraded for high pressure measurement. Several changes have been adapted to the spectrometer regarding the diamond anvil cell (DAC).

2.3.1 Diamond anvil cell (DAC)

The DAC we used in the system is a commercial Beryllium Copper cell originally designed for micro-Raman spectrosopy (Fig. 2.12). There is a 52° measuring window and the gasket is enclosed inside the cell so as to stay heat conducting with the whole cell. The diamond anvils we choose are type IIac since they contain fewer Nitrogen defects. The culet diameter is 500 μm, also it has no bevel and no extra NV implantation. The gaskets we used are metallic disks made from beryllium copper.

In order to probe the AC field under pressure using NV centers, a diamond chip (sample B) is positioned in the middle of the gasket hole. The hole is filled by the pressure media, Daphne oil 7575, which is a transparent liquid at ambient condition. The typical gasket thickness and hole size after pre-indentation is 150 μm and 200 μm and the NV chip size is roughly 80 μm.

Based on the gasket material, the diamond shape and the pressure media, the

maximum pressure one can reach with this setup is approximately 20 GPa.

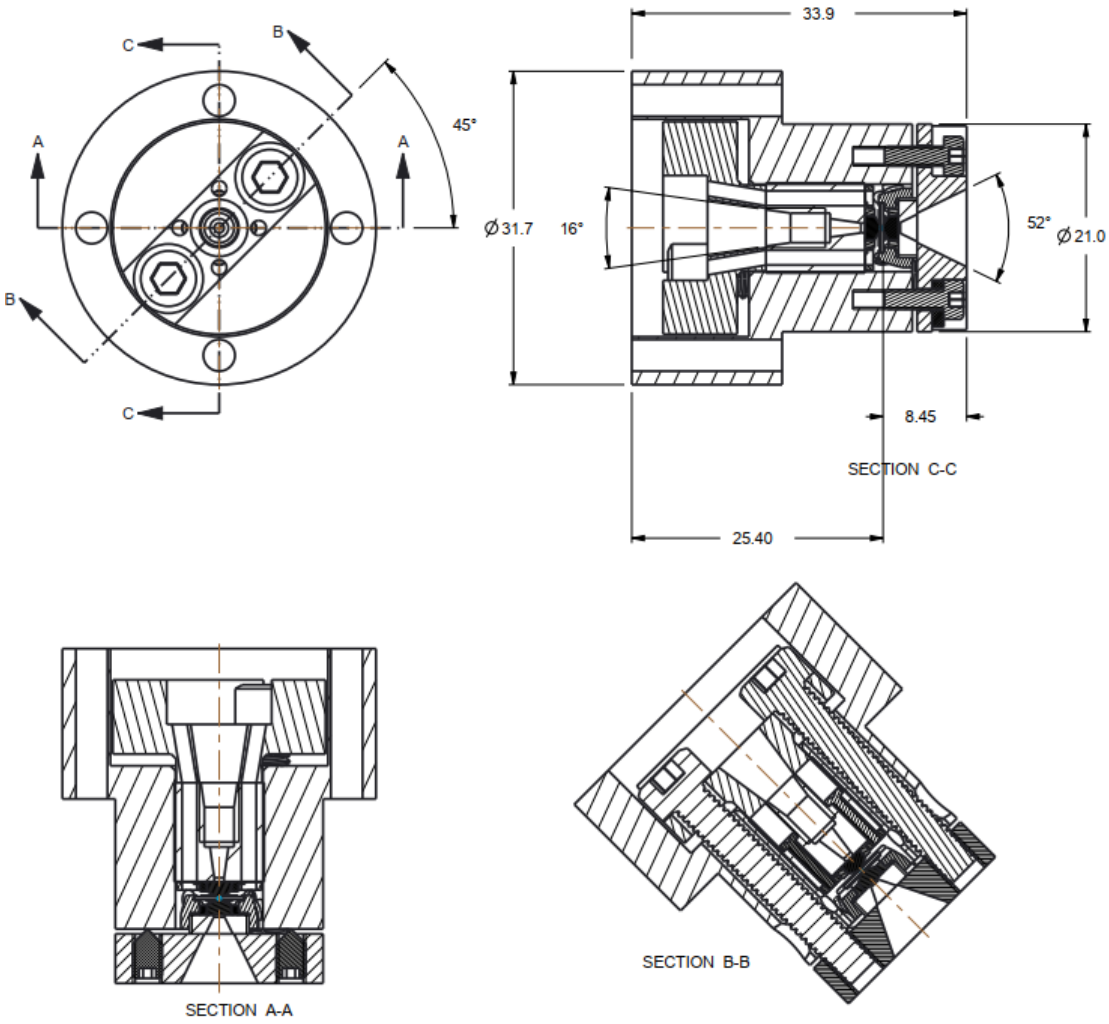

Figure 2.12: CryoDAC-ST DAC Orthographic projection drawings from Almax easylab

2.3.2 Optical adjustment

The DAC enables the possibility to measure NV under extreme pressure, however at high pressure, optical detection is difficult. The DAC has a 8.5 mm working distance to the sample which precludes the use of a high Numerical aperture (NA) objective,

which will result in larger focus volume, lower power density and smaller fluorescence collecting angle. The objective (Nikon CFI T Plan Epi SLWD 50X Objective NA 0.4) current used has a long working distance (22 mm), which approximately doubles the diffraction limit. The minimum detectable NV density is proportional to the focusing volume, therefore the minimum NV density in DAC ρ_{min}^{DAC} becomes to be 4.0×2^3 ppb, which is not far from sample B's NV concentration. Hence the NV contrast signal is rather small in the cell, and it takes longer time to get trustworthy results.

Another issue is the alignment of the NV chip. It is challenging to determine the laser focus point on the chip in x, y and z direction within the DAC. It is hard to apply the bias field on the [111] direction compared with ambient condition where the diamond orientation is more obvious. It turns out that the best approach is the CMOS camera. After the camera is aligned with fluorescence, the laser focus point can be chosen by translating the chip until it generates a clear image on the camera (Fig. 2.13). Also the image can be used to determine the diamond orientation. By combining the NV CW spectra and NV chip's fluorescence image, the bias field can be positioned in the right direction.

2.3.3 Antenna design

The approaches to transmit MW power into the DAC have always being challenging. Some attempts have been done such as μm induction coils[44], designer anvil with embedded antenna[77] and Lenz lens resonator[57]. Though they might be very effective in some circumstances, these methods are convenient to introduce enough MW power while it is invariant under pressure. Another issue is the RF screening of metallic gasket, which make it almost impossible to use the antenna on the outside of the gasket. Due to these concerns, we decided to fabricate gold MW strips and

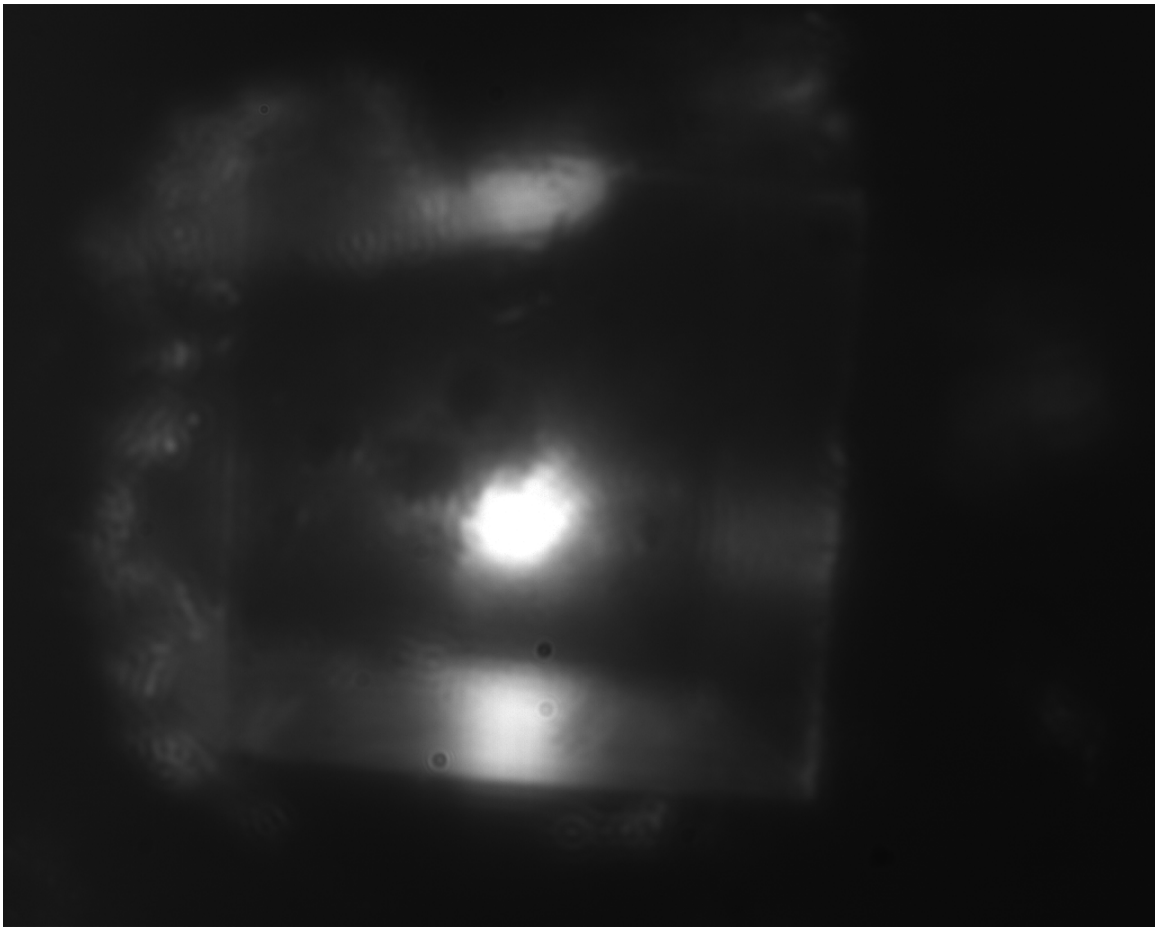

Figure 2.13: CMOS camera fluorescence image from a micro diamond chip in the DAC. The brightness on the picture indicates red fluorescence intensity. The laser focusing point is the brightest spot in the middle, which is approximately 10 μm. There is also some amount of fluorescence glowing on the edge of the diamond chip.

let them pass directly into the gasket hole region (Fig. 2.14). More details with be discussed in 4.1.1.

2.3.4 DAC preparation

The DAC preparation is essential before the real experiment. Success under pressurization mainly depends on the treatment of each detail of the preparation – a single mistake in one of the procedures might cause a series of problems afterwards. It is

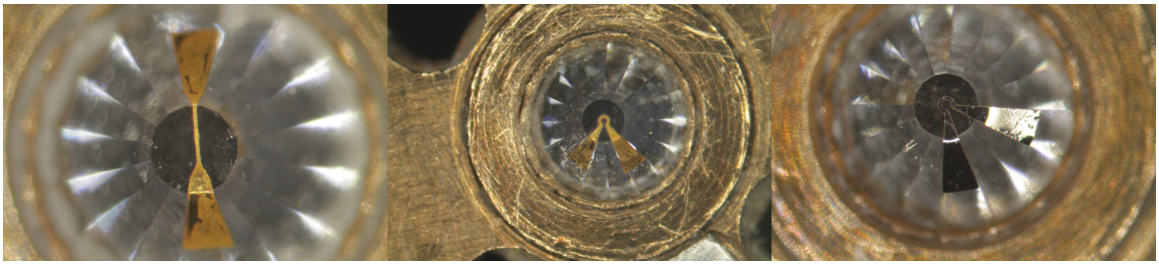

Figure 2.14: Left: straight antenna conducting layer. Middle: loop antenna conducting layer. Right: loop antenna insulating layer

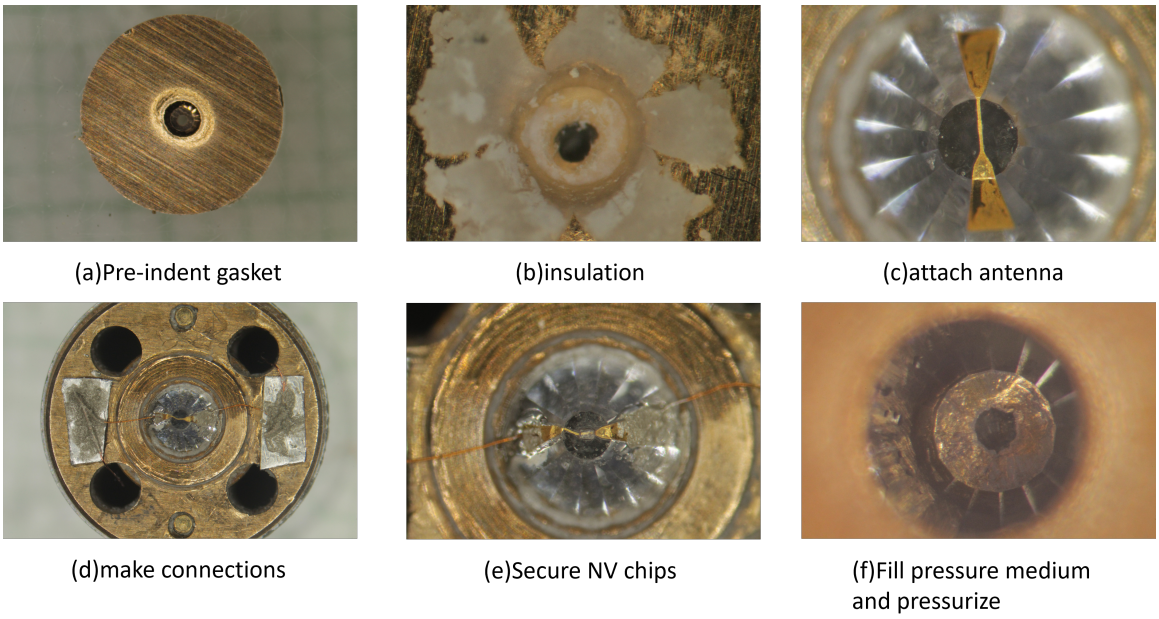

Figure 2.15: Procedures to prepare the DAC before pressurization

beneficial to slow down and check each step carefully, so a week time line is recommended (take several rests and always have steady hands!). Here is a protocol we used for this work[84] and it took us more than five attempts to get it work.

2.3.4.1 DAC diamond alignment (1st day)

The purpose of alignment is to make sure the two anvil diamonds are aligned perfectly so that the pressure applied is uniform and it won't damage the anvil. A microscope and a single color light source is needed.

First, push the piston into the cell but leave a space of about 0.2 mm between the two anvil faces and focus microscope on the diamond – diamond interface. In general, the two anvil faces will not be coincident. Using the four lateral screws on the side, bring the two faces into coincidence. Tighten all four screws, checking that the alignment is not disturbed.

Second, turn on the lamp and push gently on the piston so that the two anvil surfaces are brought into contact. Viewing down the microscope, coloured fringes should be seen. Use the two sets of screws on the bottom to move the fringe pattern in the direction of fewer fringes until, eventually, the field of view is uniformly coloured. At this point the anvils are accurately aligned for tilt.

2.3.4.2 Gasket preparation (1st $\sim$ 2nd day)

First, pre-indent the gasket in the DAC. Before applying the pressure, try to make a mark on the gasket, which will show which side of the gasket is facing up, and will help ensure the gasket is put back in the same orientation after being taken out of the DAC. Then put in the piston and align it with the mark on the DAC and apply a small amount of pressure (less than 3 GPa) where you just begin to feel some resistance when turning the screws. After pressurizing take the gasket off and check both sides of the gasket, making sure the material is pushed away from the center region and the surface in the middle looks uniform.

Second, drill a hole through the center of the pre-indented region using Electric Discharge Machining drilling system (Hylozoic EDM). The size of the hole is determined by the size of the tool to discharge (copper wire). The tool used in this experiment is 260 μm. Fill in fluids to overflow the gasket and center the tool to the middle. Record the thickness of the pre-indented region based on the readings. The

thickness we measured is ranging from 150 to 200 μm. The final gasket should look like Fig. 2.15(a).

2.3.4.3 Gasket insulation (2nd $\sim$ 3rd day)

First, prepare some stycast 1266. The part A and B needs to be in ratio of 100 : 28 to behave the best after it cures. So try to use analytical balances while weighing the two. Adding part B directly into part A is recommended. After mixing the epoxy for 5 minutes until they look as a whole, pump on the mixture until all the bubbles come out.

Next, add insulating powder into the epoxy. Wash the tools with methyl alcohol and dry them in the fume hood. Start to add powder into the mixed epoxy – the powder can either be micro-size aluminum oxide (50 μm) or cubic boron nitride. The epoxy can actually take a large amount of powder, so it often takes two to three times to add the powder and mix well. Gradually the mixture becomes stiffer, hence some tools like mortar could be helpful. Eventually the mixture becomes brittle and looks like flakes as the amount of powder increases. The ideal stage for insulation is between 'the dough' and 'the flake' – since the mixture won't stick onto the anvil completely and won't be easy to be ripped off from the gasket as well.

Lastly, press the insulation onto the gasket. The pressure applied on the piston cannot be bigger than pre-indent pressure – usually just finger pressure without the screw. It'd be better to press some mixture inside the DAC and check on the status of the residue. If it is still opaque, it probably means it is not dense enough. Before the final press, put some insulating powder above the mixture so that it is less likely to stick onto the anvil. After finger tightening on the piston, let the insulation cure

in an oven around 70°C overnight.

Take out the DAC next day, and the insulation should mostly stick onto the gasket like Fig. 2.15(b). Use a micro drill (similar to the size of hole) to tap a hole (careful the drill is brittle). The insulation should not be too brittle and not be too stiff either. Clean the anvil on the piston at the end.

2.3.4.4 Antenna and NV attachment (4th $\sim$ 5th day)

The purpose of insulation is to separate the antenna from the conducting gasket. The insulation is attached against the piston anvil where the antenna should be attached. The antenna strip consists of two large conduction pads joined by a narrow strip. It has two sides: one side is the coating layer and the other side is the gold layer.

Firstly, secure the middle structure onto the anvil using the stycast. Try not to flatten the whole strip onto the culet surface but leave some room to let the strip relax under the pressure. Bend the pads towards the side surface of the anvil and secure them down flatly after the first batch stycast is cured. The final look will be like Fig. 2.15(c).

Secondly, make the connection: stick some conducting tape onto the piston surface to guide the conducting wires. The MW eventually come through a SMA connector, and a special PCB board is made to join the antenna and SMA connector. There will be two bigger wires (AWG 36) connecting from PCB strips to the connecting tape through the tunnels on the piston, and will also be two smaller wires (AWG 44) connecting from the tape to the antenna. The connections are made by silver epoxy (MG Chemical 8331) on conducting tapes and pads. The wires will be soldered onto

the PCB strips. Usually the resistances between pads are around 1 Ohm and the total resistance from PCB SMA connector is about 2 to 3 Ohms. Next, Secure the micro NV chip onto the bottom anvil (make sure the gasket can still sit onto the bottom anvil after the NV chip is glued). It should look like Fig. 2.15(e).

Finally, put on the gasket and add in some pressure medium. In principle the bottom culet and pre-indent gasket should hold a closed space which pressure medium goes into. The liquid level should be more than half filled but should not leak onto top pre-indent surface. Lastly, insert in the piston with antenna attached, check the connection between DAC shell and SMA leads as the piston is inserted further. If they are shorted, take the piston out and check the insulation. Otherwise, cap the piston and tap in the screw gently. The DAC is ready to pressurize(Fig. 2.15(f)).

2.4 Solid state NMR system

The Oxford magnet(Fig. 2.16(a)) is the main instrument for $TmVO_4$ angular dependence measurement. It is a high homogeneity warm bore magnet with a fixed field. The field last measured on 1/22/2014 is 11.7285 T and the homogeneity at its center is about 1.1 ppm. The magnet is coupled with a closed cycle Janis cryostat (model SHI-950T) which is controlled by a compressor (Sumitomo F-50L) and temperature controller (Lakeshore 340 cryogenic). The available temperature range is 300K - 4K, and down to 1.5K with a vacuum pump. NMR measurements are performed with a spectrometer (Tecmag Apollo 37723) and a 55 db pulsed RF amplifier (CPC 5T300M). The Oxford is vacuum and nitrogen jacketed, and used in a fixed field configuration.

The dual-axis goniometer NMR probe (Fig. 2.16(b)) [72] enables fine angular control for both in plane (ab) and out of plane (c) direction of a tetragonal crystal. There is a fast axis (1 : 30) and a slow axis (1 : 600). For our purpose the slow axis is used to control the angle between the external field and the crystal c axis. The sample is wrapped by a silver coil and glued onto a sample holder which is inserted onto the probe.

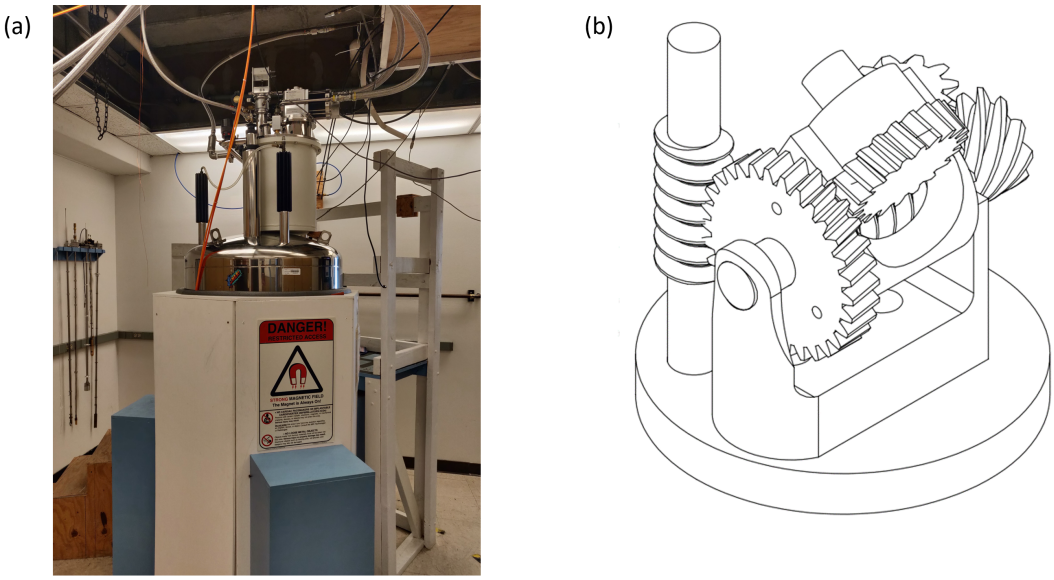

Figure 2.16: (a) Oxford magnet and cryogenic system; (b) Goniometer probe head drawing

Chapter 3

Quantum sensing with NV ensemble

In recent years, the field of quantum sensing has become a distinct and rapidly growing branch of research within the area of quantum science and technology. The sensing protocols in fact can be implemented on any qubit systems, and ac signals can originate from different sources that couple to the qubits [62]. Ultimately, our goal is utilizing these quantum sensing methods on NV^- centers platform to achieve very small volume ac optical detected magnetic resonance (ODMR). For conventional NMR, which is also a successful sensing method for ac signal detection of nuclear spin polarization, a solenoid around the sample is used to pick up ac fields via Faraday induction. On the other hand for ODMR, the nuclear spin ac signal is captured by phase accumulation of nearby NV^- centers. Depending on the strength of the coupling of the coherent precession, nuclear spins for this case, ODMR can achieve ultra high sensitivity even for nano volume samples [33], which could not be measured using traditional pulsed NMR techniques.

In this chapter, some important sensing protocols and their experimental realization of ODMR is discussed, starting with the comparison between continuous and

pulsed scheme.

3.1 Continuous vs Pulsed

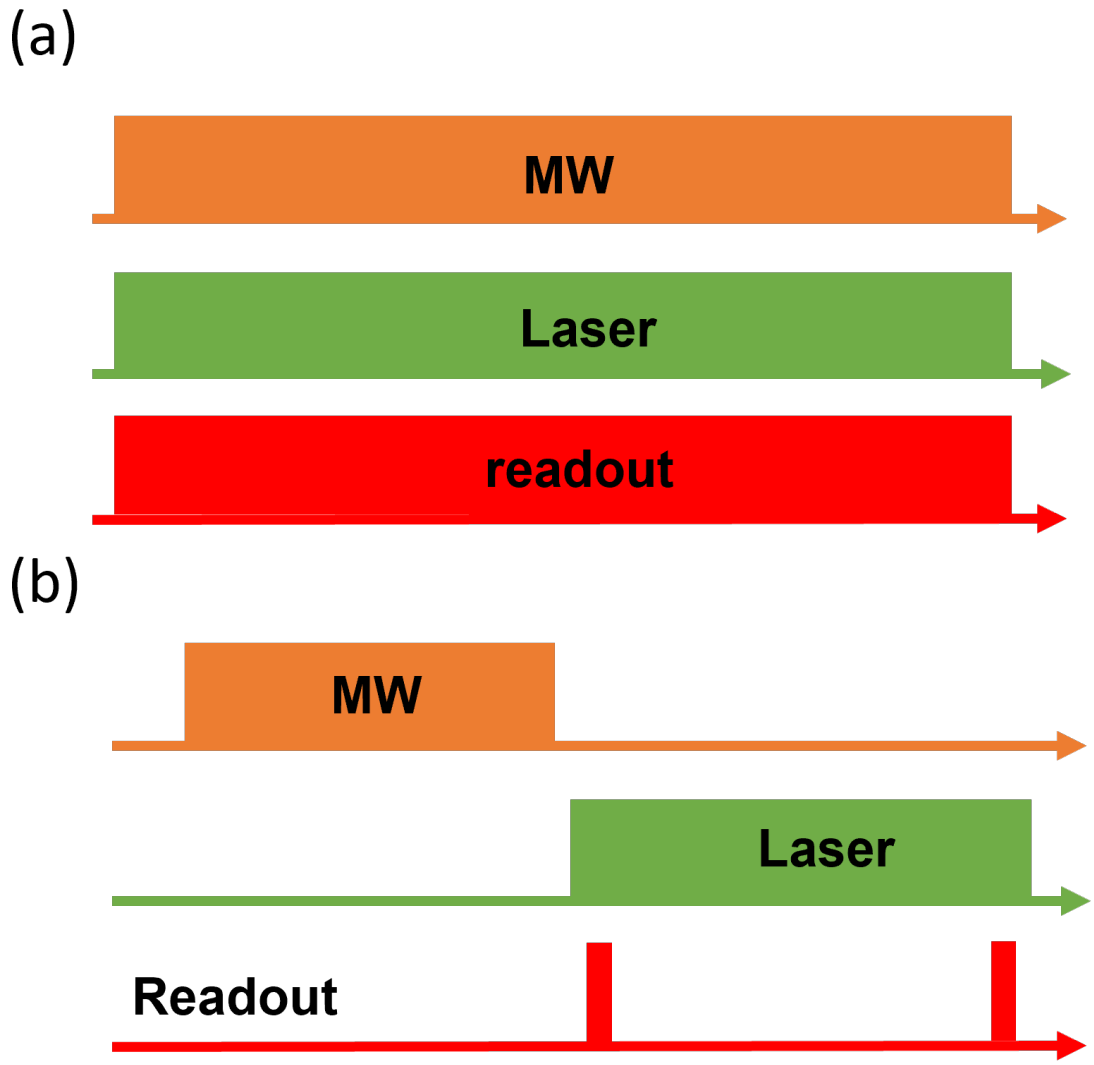

Figure 3.1: The schematic plot of CW-ODMR (a) and pulsed ODMR (b) magnetometry protocols

The continuous wave (CW) ODMR is a simple, widely employed magnetometry method. Unlike pulsed ODMR, its implementation does not require synchronization control; the technique is therefore technically easier to implement than pulsed measurement schemes. The schmatic plot is shown in Fig. 3.1(a).

However, CW-ODMR is not envisioned for many high sensitivity applications for multiple reasons. First, CW-ODMR usually has weak fluorescence (FL) contrast even with lock-in amplification [77], Second, unlike pulsed ODMR whose resolution is determined by decoherence time T_2^* (Fig. 3.1 (b)), CW-ODMR methods suffer from MW and optical power broadening which is usually beyond the scale of $(T_2^*)^{-1}$.

Despite poor resolution, CW ODMR is a powerful tool to understand NV center energy levels and orientations, which is useful prior to more subtle measurements. In order to achieve AC sensing ODMR, pulsed control of NV^- centers is required.

3.2 CW NV ODMR

Exposing the NVs to 532 nm excitation light for a few microseconds is sufficient to initialize all the NVs to their ground state and FL should be at I_0 (Section 1.4.2). If the CW microwave field at the frequency of the $|0\rangle \leftrightarrow |\pm 1\rangle$ transitions are turned on while the laser is pumping, a different equilibrium is reached and the FL signal I_1 should be reduced from I_0. Therefore the FL contrast, $\Delta I = (I_0 - I_1)/I_0$, which is typically on the order of a few percent at room temperature depending on the laser power and NV density, can be used to characterize the microwave transitions. In other words, $\Delta I \neq 0$ only when f_{MW} is close to NV $|0\rangle \leftrightarrow |\pm 1\rangle$ transitions. By sweeping f_{MW}, the energy spectra, or so called electron spin resonance (ESR), of NV centers can be obtained.

Fig. 3.2 displays some ESR spectra under various conditions. When there is no external magnetic field, the energies of tje $|\pm 1\rangle$ states are degenerated – therefore a single transition at zero field splitting $D = 2.87$ GHz is expected (red curve). With the non-zero external magnetic field, if the NV centers are misaligned from one of four possible NV axis ([111] for example), there are eight peaks in total indicating response from each NV orientation (blue). If the field is aligned, there are four peaks

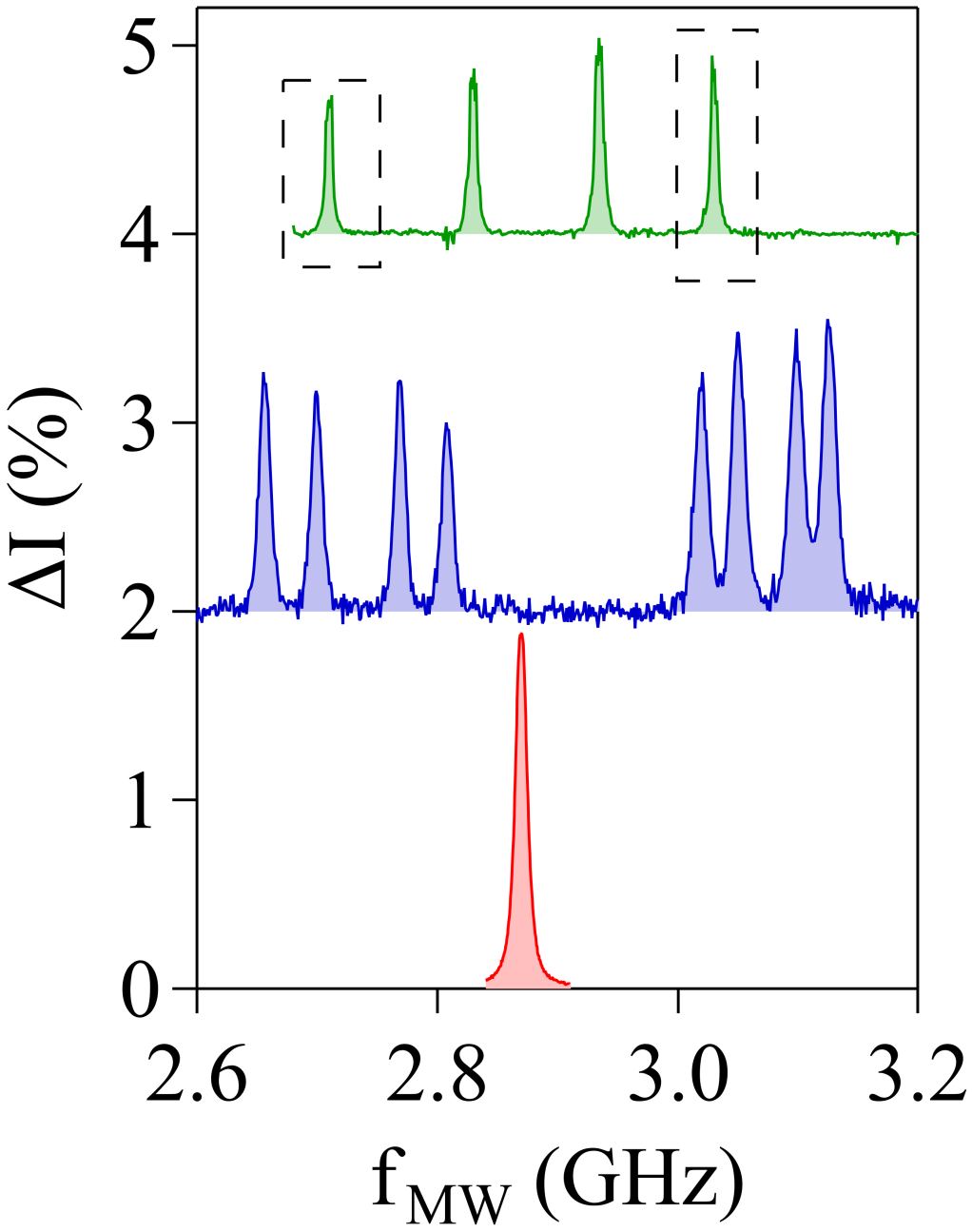

Figure 3.2: NV ensemble ESR spectra intensity ΔI versus f_{MW} with external field: 0 mT (red), 11 mT (blue) and 6 mT (green). The 11 mT field is misaligned with NV center axis.

due to the symmetry (green). The outermost transitions (in dashed box) are $|\pm 1\rangle$ transitions in parallel with the external field.

In practice, ODMR has better performance if a clean two-level system is chosen. By introducing an external magnetic field, one particular orientation of the NV ensemble can be distinguished from the other three. A sub two-level system can be realized by choosing two energy levels from $|0\rangle$ and $|\pm 1\rangle$, which all belong to one type orientation NV center.

3.2.1 Light polarization effect

The equilibrium ΔI is proportional to the optical transition rate between ground state $|^3A_2\rangle$ and excited state $|^3E\rangle$:

$$\begin{aligned} p_{dipole} &\sim |\left\langle {}^3A_2\right| \vec{A_0}\cdot\vec{r}\,|E_x\rangle\,|^2 + |\left\langle {}^3A_2\right| \vec{A_0}\cdot\vec{r}\,|E_y\rangle\,|^2 \\ &= |\vec{A_0}\cdot(\langle a_1|\,\vec{r}\,|e_x\rangle\,|^2 + |\vec{A_0}\cdot(\langle a_1|\,\vec{r}\,|e_y\rangle\,|^2 \end{aligned} \tag{3.1}$$

where $\vec{A_0}$ is the exciting laser's polarization vecter, $|a_1\rangle$ is the second highest orbital ,and $|e_x\rangle$, $|e_y\rangle$ are the highest orbitals of the NV electric ground manifold (Fig. 1.5). The excitation raises one of the electrons from $|a_1\rangle$ to $\left|e_{x(y)}\right\rangle$. Due to the C_{3v} symmetry, $|e_x\rangle$ and $|e_y\rangle$ have non-zero transition dipole moment [18]:

$$\langle a_1|\,\vec{x}\,|e_x\rangle = \langle a_1|\,\vec{y}\,|e_y\rangle := D, \tag{3.2}$$

and the dipole directions for x and y are $[\bar{1}\bar{1}2]$ and $[1\bar{1}0]$ respectively[27]. Assuming the polarization vector $\vec{A_0} = \{\cos(\phi_0 + 2\phi), \sin(\phi_0 + 2\phi), 0\}$ (light is propagating to NV diamond via z axis), the transition rate can be simplified to be:

$$p_{[111]} \sim \frac{|D|^2}{3}(2 - \sin(4\phi + 2\phi_0)), \tag{3.3}$$

where ϕ_0 is the initial laser polarization angle and ϕ is the angle between initial polarization and half-wave plate's fast axis (Section 2.2.1). Similarly, the transition

rate for the other three NV orientations can be written as:

$$
\begin{aligned}
p_{[\bar{1}\bar{1}1]} &\sim \frac{|D|^2}{3}(2-\sin(4\phi+2\phi_0)) \\
p_{[1\bar{1}\bar{1}]} &\sim \frac{|D|^2}{3}(2+\sin(4\phi+2\phi_0)) \\
p_{[\bar{1}1\bar{1}]} &\sim \frac{|D|^2}{3}(2+\sin(4\phi+2\phi_0))
\end{aligned}
\tag{3.4}
$$

Fig. 3.3(a) shows the ESR contrast ΔI versus ϕ. Indexes 1 2 3 4 represent four orientation of NV centers. Since the NV crystal is misaligned, four orientations make up eight peaks in total. As expected, two orientations 1 and 3 have similar behavior whereas 2 and 4 show the opposite (Fig. 3.3(b)). The period of $\pi/2$ is due to the nature of HWP: ϕ rotation on fast axis leads to a 2ϕ rotation on the output polarization direction.

While the NV diamond is aligned with external field, one orientation is separated from the other three. As a result, there are two groups of peaks (Fig. 3.2 green line). Despite different offsets, the polarization angle has opposite effects on two groups. To be specific, when the outer satellites reach maximum ΔI, the inter peaks should be minimum.

3.2.2 Hyperfine coupling to ^{13}C

The NV center is a prefect local probe since its Hamiltonian contains not only the NV electron and the spin interactions but also hyperfine coupling to nearby nuclear spins. The strongest coupling happens between the NV spin and its nearby carbon nuclear spin. The carbon element has two stable isotopes ^{12}C and ^{13}C, whose abundance are 98.9 % and 1.1 % respectively. Though ^{12}C has zero nuclear spin, ^{13}C has $I = 1/2$. Thus it can couple to NV electron spins.

Fig. 3.4 shows ESR spectra containing NV coupling to ^{13}C spins. The two satel-

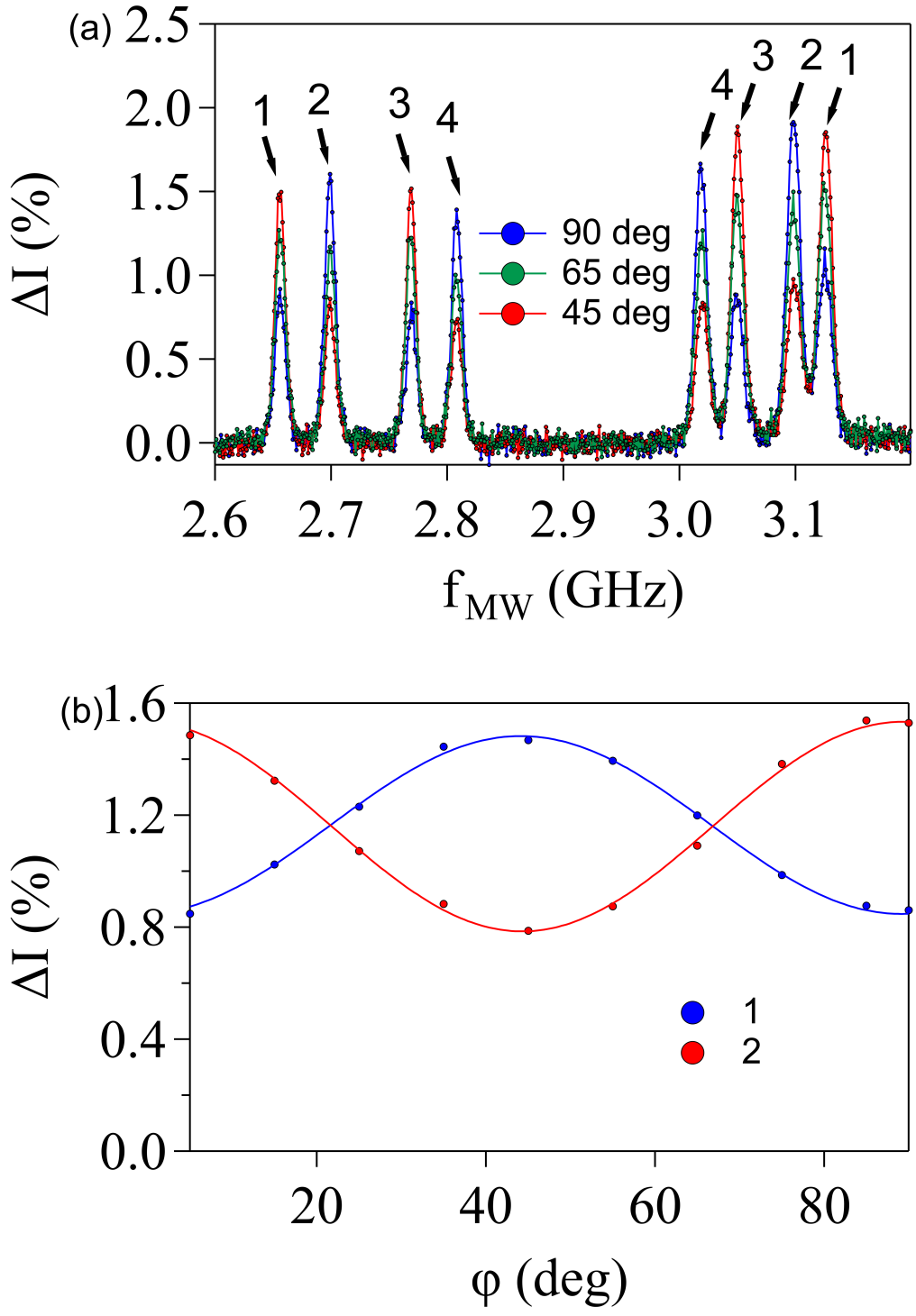

Figure 3.3: (a) Misaligned ESR spectra versus HWP's fast axis angle ϕ (b) Signal contrast ΔI at NV 1 and 2 versus HWP's rotation angle. The solid curves are fittings using Eq. 3.4. $H_0 = 11$ mT.

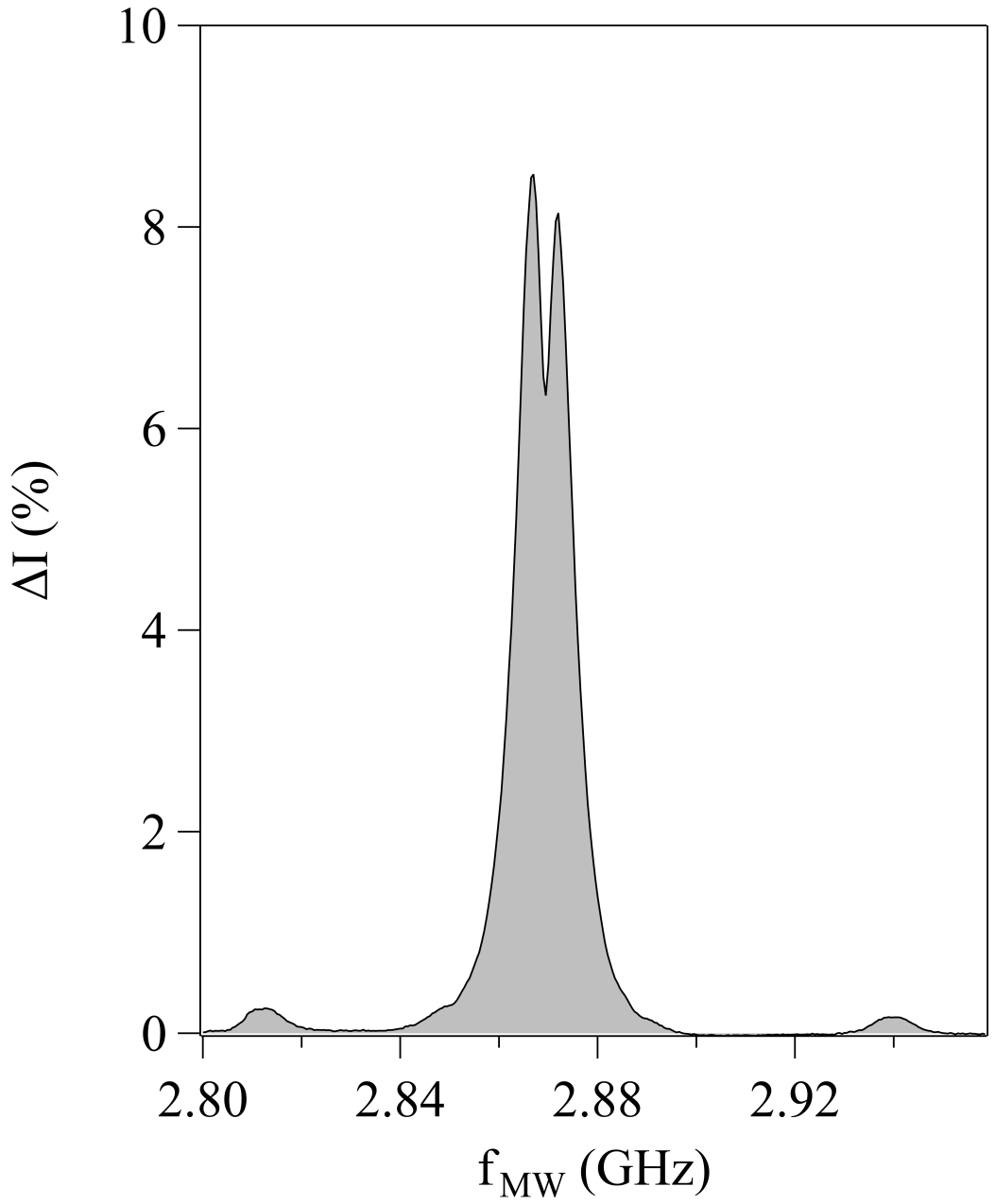

Figure 3.4: NV ensemble ESR spectra with zero external field. The two satellites at 2.812 and 2.941 GHz are due to NV electron spins coupling to their closest ^{13}C neighbor

lites below (2.812 GHz) and above (2.941 GHz) zero-field splitting frequency (2.87 GHz) are attributed to hyperfine coupling. The area ratio of ^{13}C peak and the total spectra is about 3.15 %, which is in the same order as ^{13}C abundance.

If we assume hyperfine coupling $S^{'} \cdot A^{'} \cdot I^{'}$ between ^{13}C and NV has axial symmetry [73], the tensor $A^{'}$ should be like:

$$A^{'} = \begin{pmatrix} A_{\perp} & 0 & 0 \\ 0 & A_{\perp} & 0 \\ 0 & 0 & A_{||} \end{pmatrix}. \tag{3.5}$$

In order to combine it with the NV Hamiltonian, a rotation is needed to transform tensor and nuclear spin into NV axis. Define $R = R_y(109.47°)$, then $A = R \cdot A^{'} \cdot R^{\dagger}$ and $S^{'} \cdot A^{'} \cdot I^{'} = S \cdot A \cdot I$. The full ^{13}C-NV Hamiltonian can be written as:

$$H_{NV^{-13}C} = DS_z^2 + E(S_x^2 - S_y^2) + S \cdot A \cdot I, \tag{3.6}$$

where D is the zero-field spiltting and E is the residue stress term that splits the $|\pm 1\rangle$ transition.

Solving the energy level and fitting them into experimental data, we find $A_{||} = 389$ MHz and $A_{\perp} \sim 0$. The result is different from pervious EPR results ($A_{||} = 198.2$ MHz $A_{\perp} = 120.8$ MHz [30]). A potential explanation is that zero field NV ESR is mainly dominated by strain effect whereas NV EPR is dominated by magnetic field applied at certain axis. A proper understanding to explain both NV ESR and NV EPR data is still uncovered.

3.3 Pulsed NV ODMR

Unlike ESR measurements, the pulsed approaches require a relative short MW pulse ($t_{MW} \ll T_1$) and the NV spin state readout happens immediately after the MW pulse train. Measurements such as Rabi, Ramsey and other dynamic decoupling sequences are probing a non-equilibrium spin state, whereas ESR measurements are probing spin state in thermal equilibrium. More importantly, NV ODMR is based on the

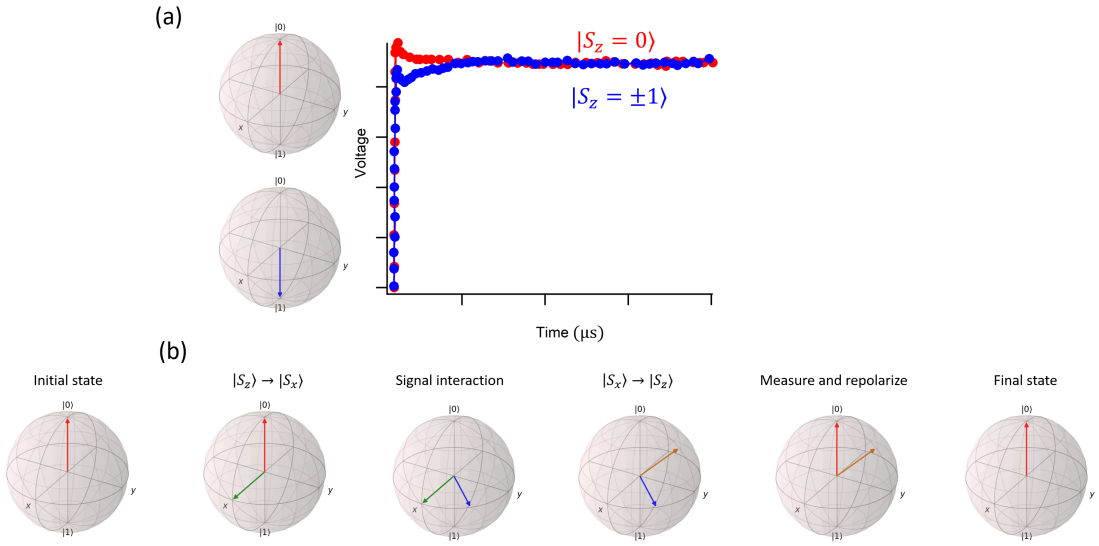

Figure 3.5: (a) The sub-system qubit of NV and its measured signal (b) General sensing protocol. Most of quantum sensing method can be divided into these steps: initialization, basis transformation, signal interrogation and detection.

qubit nature of NV ground state – the sensing information is stored in the phase ϕ of a qubit: $|\psi\rangle = \frac{1}{\sqrt{2}}(|0\rangle + e^{i\phi}|1\rangle)$.

A map between NV spin states and qubit states and general sensing protocol is shown in Fig. 3.5. We know that the target signal is proportional to the ground state density $\rho_{00} = \langle 0|\psi\rangle \langle\psi|0\rangle$ (Section 1.3). Initially, the qubit is prepared in $|0\rangle$. Then with the help of the MW pulse, the qubit is transferred from S_z basis to S_x basis. During the interaction period, if the target signal is coupled to qubit S_z, the in-plane phase evolves from ϕ to ϕ'. Eventually, by reversing the basis transformation, the new phase is projected onto $|0\rangle$ and ρ'_{00} can be obtained when the qubit is measured and re-polarized using the laser.

In the following sections, different sensing protocols will be introduced in combination with the Bloch sphere picture and experimental data.

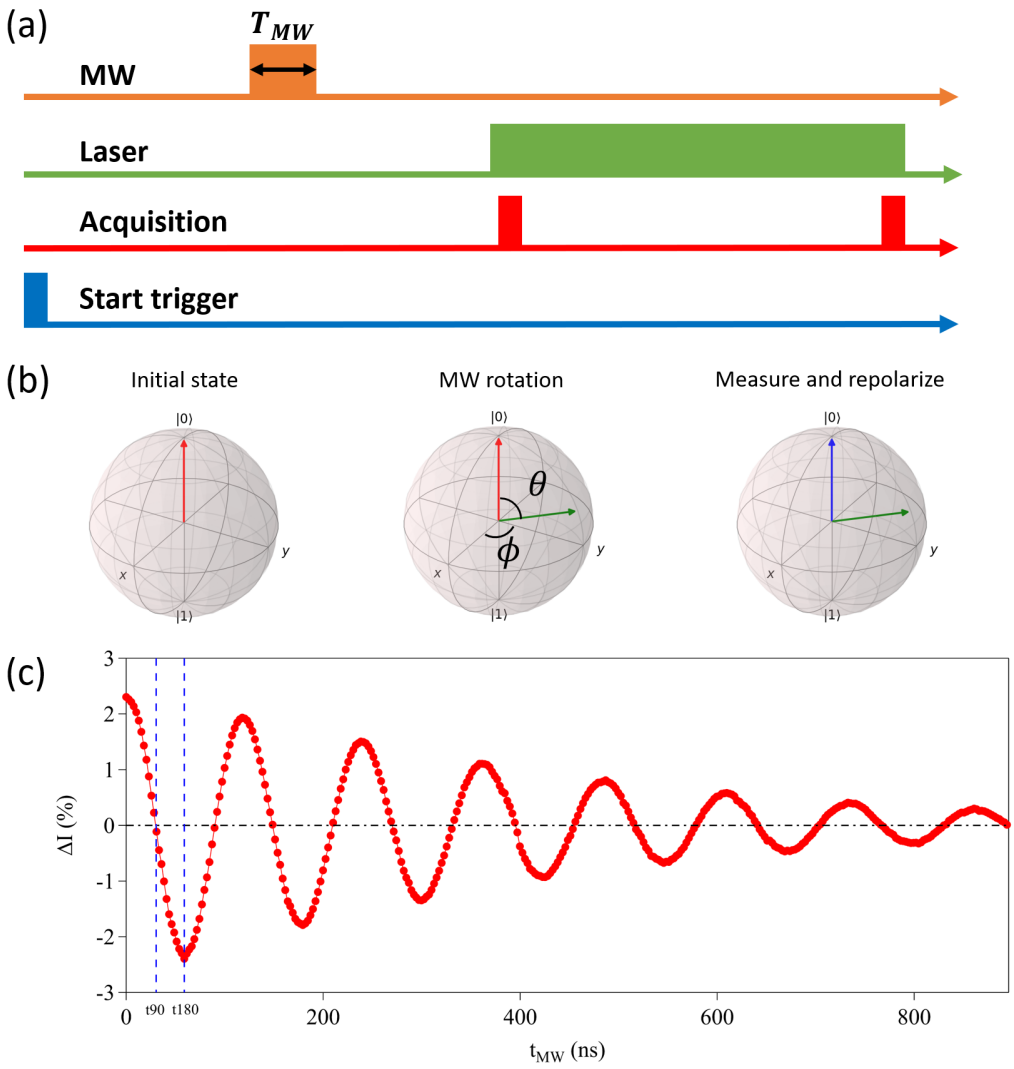

Figure 3.6: (a) Rabi oscillation timing sequence (b) NV spin state in Bloch sphere as time evolves. The rotation angle is determined by the driving MW field. (c) A typical Rabi oscillation of NV ensemble.

3.4 Rabi oscillation

In general, the Rabi oscillation is defined as the cyclic behaviour of a two-level quantum system in the presence of an oscillatory driving field. In Fig. 3.6(b), the NV spin is firstly initialized in $|0\rangle$ qubit state. By controlling the duration and power of the resonant MW pulse, the state is driven into a superposition state:

$|\psi\rangle = \cos(\theta/2)\,|0\rangle + \sin(\theta/2)e^{i\phi}\,|1\rangle$, where:

$$\theta = \gamma H_{MW} t_{MW} \tag{3.7}$$

$$\phi = \phi_0, \tag{3.8}$$

and the MW field is $\mathbf{H_{MW}}(t) = H_{MW}\hat{z}\sin(\omega_\Delta t + \phi_0)$ (ω_Δ is the energy gap of two-level system) and γ is the gyromagnetic ratio of NV. Some unitary transformations such as 90° and 180° rotation at certain axes i – $U^i_{\pi/2} = e^{-iS_i t_{90}}$ and $U^i_\pi = e^{-iS_i t_{180}}$ in rotating frame – can be realized if H_{MW}, t_{MW} and ϕ_0 are chosen properly. Hences Rabi oscillations, also known as Rabi calibrations, are often used to determined the proper MW duration and power in both ODMR and NMR.

Fig. 3.6(c) displays a standard Rabi oscillation in experiment. The oscillation can be described by constant oscillating frequency $\Omega = \gamma H_{MW}$ and exponential decay. There are several reasons causing the decay: one is the MW inhomogeneity over the NV ensemble. Since each NV sees a slightly different MW power and so oscillates with a slightly different Rabi frequency, the total signal is the sum of the oscillation with a distribution of frequencies set by the gradient of the MW power. Another reason is the MW excitation window. Since the MW is a pulse with duration t_{MW}, its Fourier transform has a width on the order of MHz. The off-resonance oscillation also has slightly different Rabi frequency and give rise to a MW distribution. To conclude, these factors result in a dephasing effect that is usually characterized by T_2^*.

3.4.1 Rabi power dependence

Fig. 3.7 shows Rabi oscillations as the MW amplitude H_{MW} increases. The Rabi frequency is increasing monotonically as the power grows, which is consistent with $\Omega = \gamma H_{MW}$. Moreover, the variance of Rabi frequency gets larger when power grows,

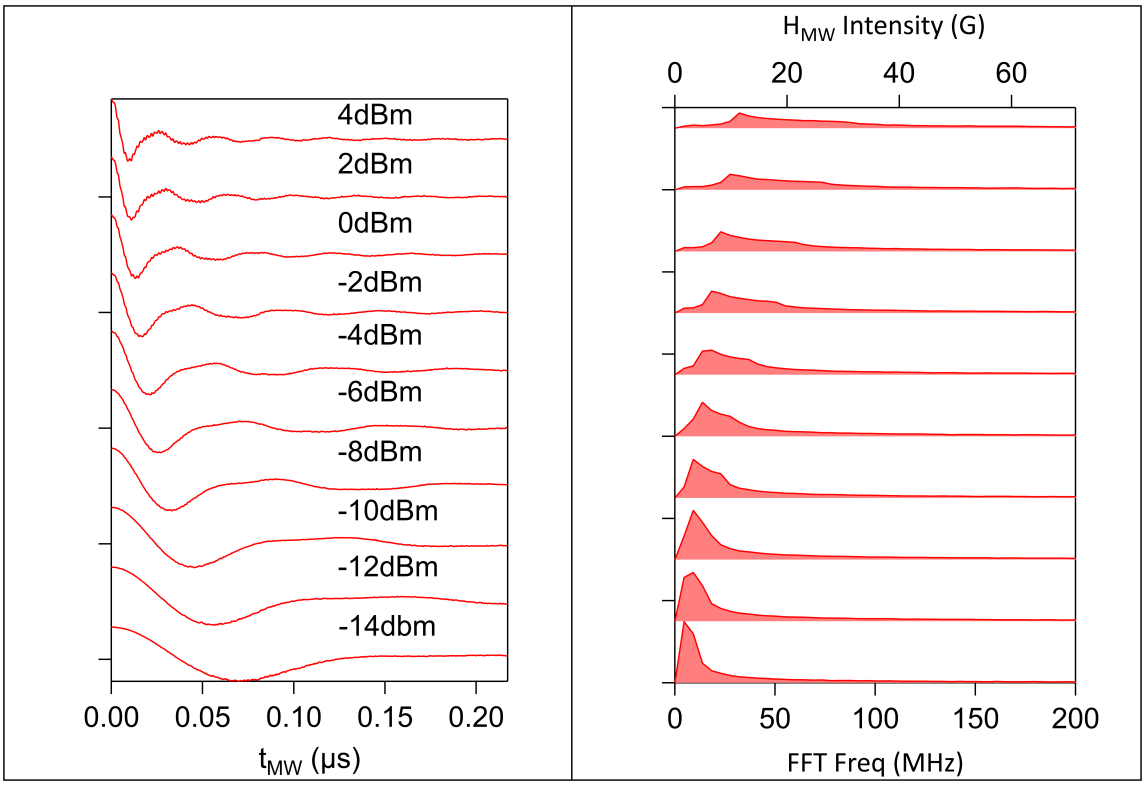

Figure 3.7: Rabi oscillations versus driving MW field intensity H_{MW} and their Fourier transforms of the Rabi oscillations, which indicate the distribution of H_{MW}. The Rabi frequency increases as the microwave power is increased. The distribution is broadened because the H_{MW} field from the microwave antenna is not homogeneous.

which reflects the gradient of the MW power. Here we demonstrate that Rabi oscillation is a ideal tool to investigate the MW field homogeneity. In practice, we want to have sufficient Rabi frequency to generate short MW pulses to create as homogeneous a response as possible. Therefore for a certain MW antenna design, the MW power can be optimized using this approach.

3.4.2 Rabi imaging

The Rabi oscillations can provide information about the MW field homogeneity. For a larger region (in the scale of hundred μm), with sufficient optical resolution, the MW field homogeneity can be directly measured using a scanning technique. Fig. 3.8 shows representative scans of the Rabi frequency, Ω, and the fluorescence intensity

FL. The spot size of the laser is less than 20 μm. Based on the result, we find that FL is uniform across the whole sample, indicating a uniform NV center distribution in the diamond. The MW power is peaked in the middle of the sample and decays to zero as it approaches to the edge of the NV sample. Thus we can infer the position of the antenna by observing the MW power spatial distribution. In principle, this method can be applied to observe the MW power variation due to changes on physical environment near the NV sample [55, 83].

3.5 Ramsey interferometry

Thanks to Rabi oscillation, the MW pulse duration for $U_{\pi/2}$ ($\pi/2$ pulse) and U_{π} (π pulse) rotations can be determined to be t_{90} and t_{180} (Fig. 3.6(c)). After initialization, a $\pi/2$ pulse rotates the qubit magnetization into the xy plane: $\frac{1}{\sqrt{2}}(|0\rangle + e^{i\phi_0}|1\rangle)$. During the free evolution period, the phase ϕ_0 can change due to two factors: the gap ω_Δ between the two-level, also called the Larmor frequency, and any interactions between the NV and target sources (for example ^{14}N nuclear spin in the diamond), which turn ϕ_0 into $\phi_0 + \omega_\Delta\tau + f(\tau)$, where $f(\tau)$ describes interaction over time τ. Finally by applying a second $\pi/2$ pulse, the qubit state can be measured and the final result is called Ramsey interferometry (Fig. 3.9(b)). A typical Ramsey interference versus interrogation time τ is shown in Fig. 3.9(c). The signal contains a fast oscillating component originated from the Larmor frequency ω_Δ. It also shows a slow envelope modulation which arises from interaction $f(\tau)$. It is worthwhile to mention that the signal contrast drops exponentially as τ increases. This is due to dephasing effect which is characterized by T_2^*, which is similar to free induction decay in NMR.

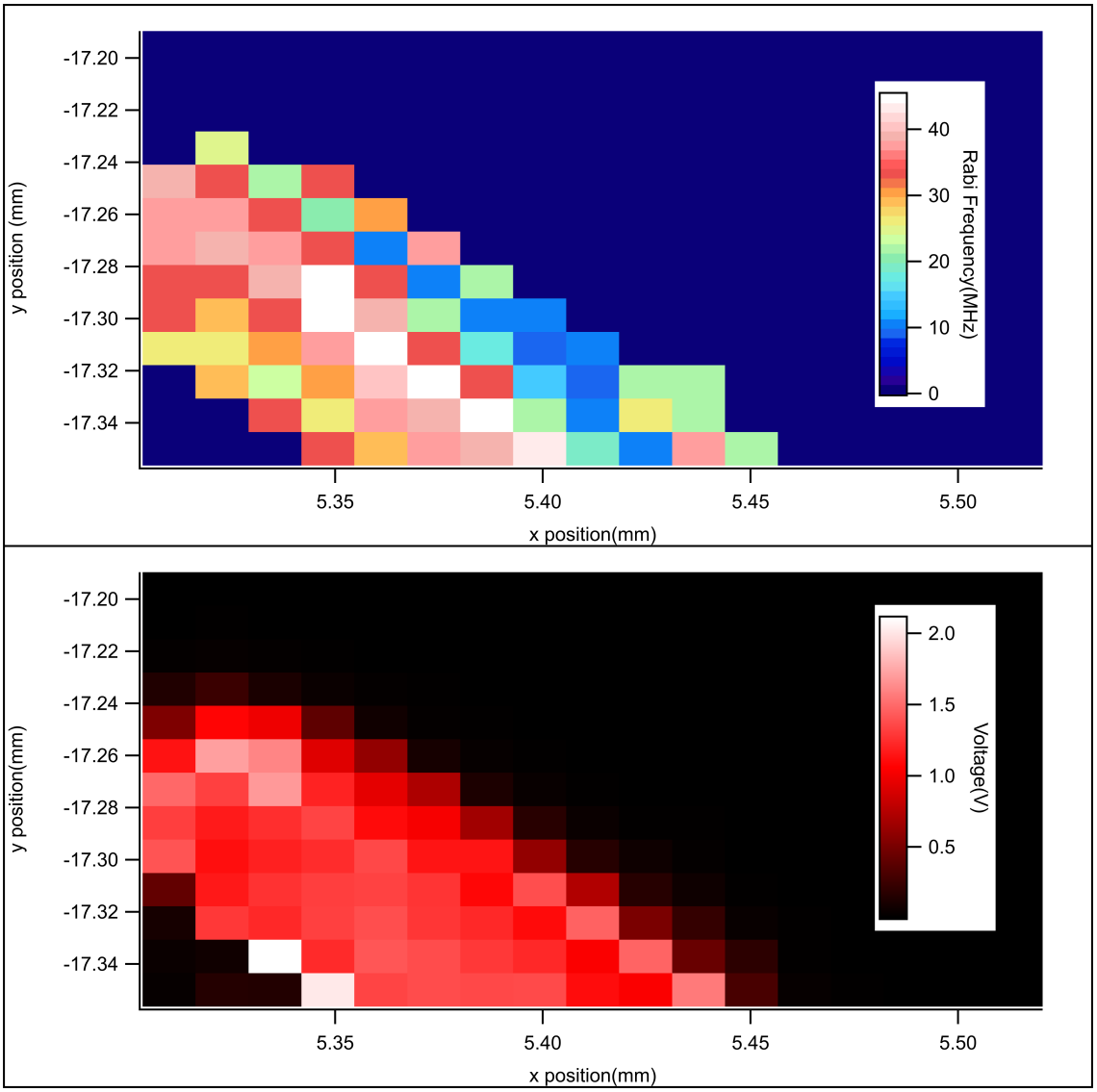

Figure 3.8: The Rabi frequency and fluorescence intensity measured as a function of the position in an diamond sample with NV centers located within a diamond anvil cell. The scanning step size is 20 μm or the scale of the individual squares on the map.

3.5.1 Quadrature detection

Besides the MW pulse duration, the pulse initial phase is also controllable, which affects the $U_{\pi/2}$ rotation axis (Eq. 3.7). By controlling the phase of the second pulse relative to the first, one can project either $\langle S_x \rangle$ or $\langle S_y \rangle$ onto the z axis (See table 3.1). Collecting data for both phases enables quadrature detection and hence the

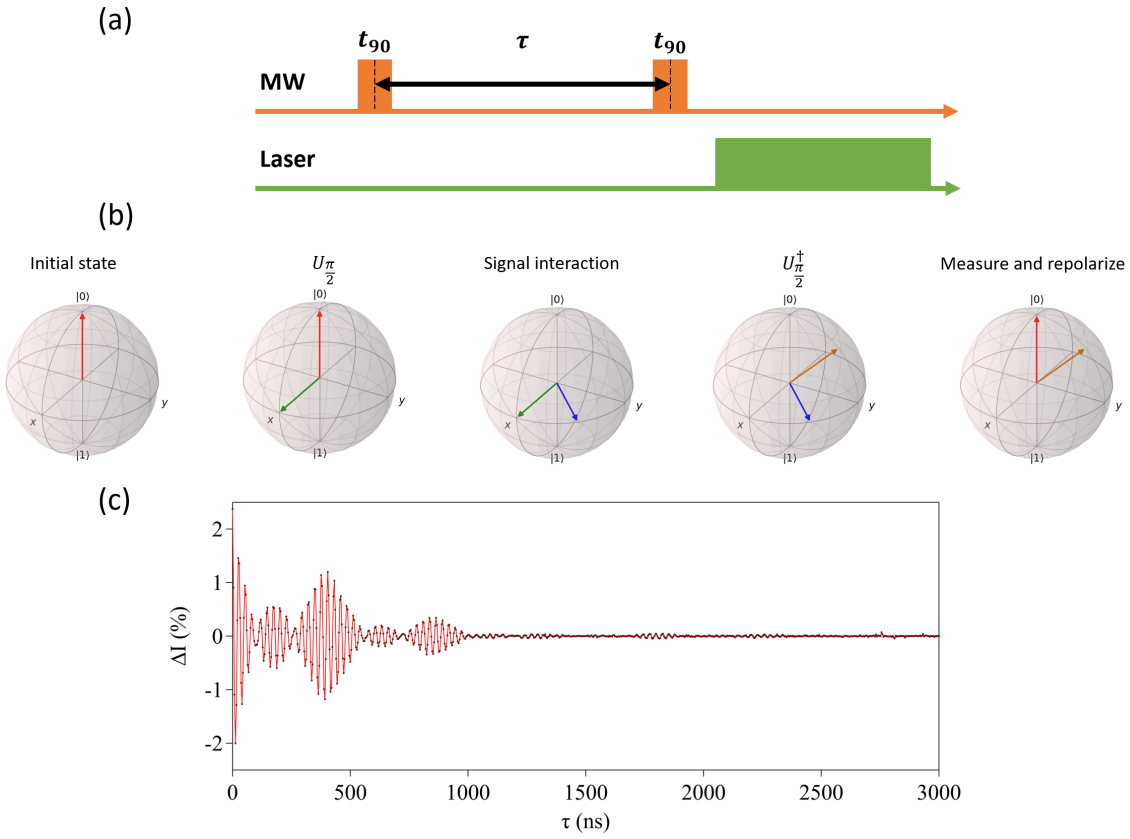

[!htb]

Figure 3.9: (a) Ramsey interferometry time sequence (b) NV spin states in Bloch sphere (c) A typical Ramsey interference of NV ensemble. T_2^* is about 700 ns.

Pulse 1	Pulse 2	ρ_{00}
x	x	$\cos^2(\omega\tau/2)$
x	-x	$\sin^2(\omega\tau/2)$
x	y	$(1+\sin(\omega\tau))/2$
x	-y	$(1-\sin(\omega\tau))/2$

Table 3.1: Ramsey result for some possible MW pulse phase configurations without interaction (ω is the Larmor frequency)

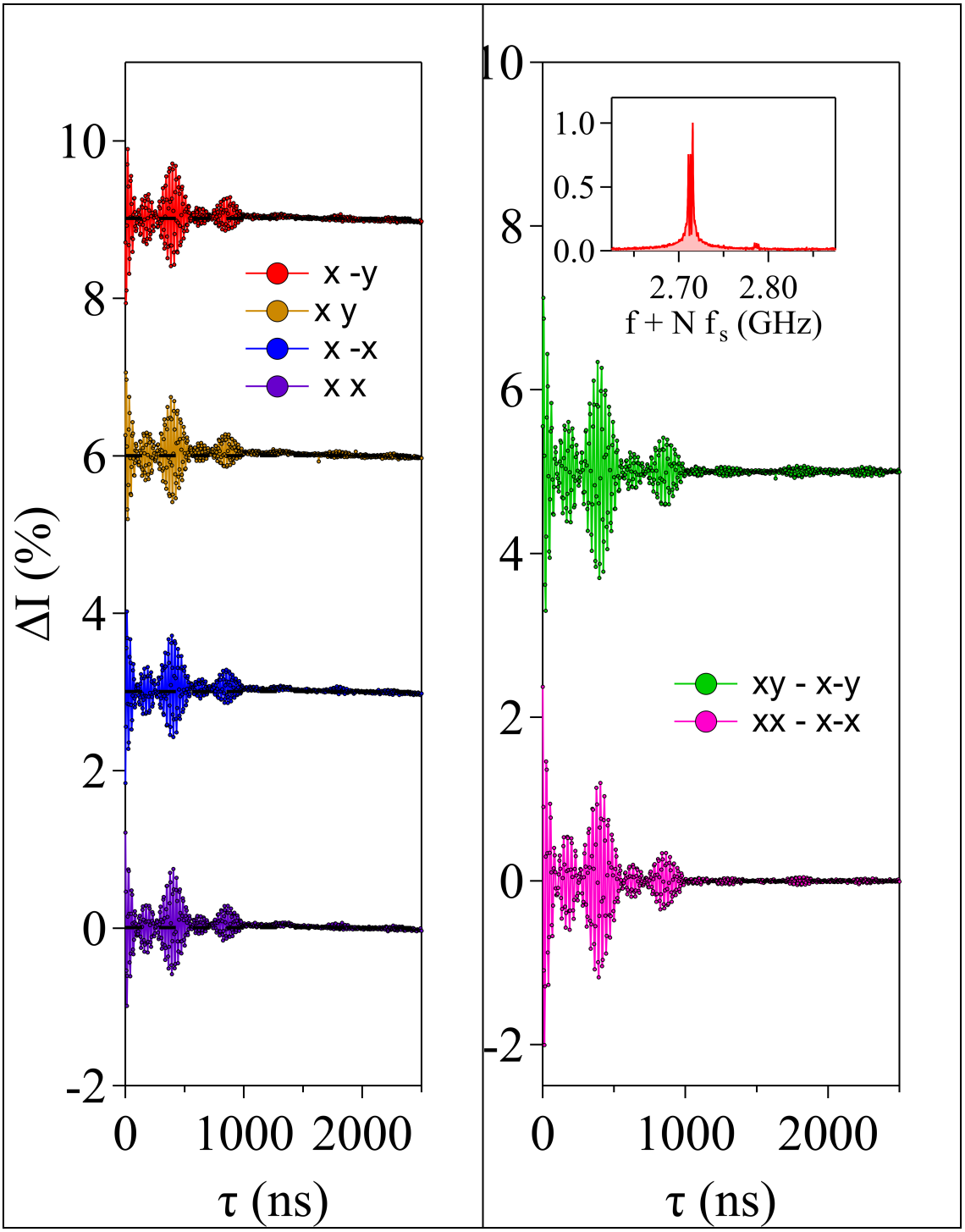

Figure 3.10: Left: four types of relative phase Ramsey interference. Right: Two quadrature components by subtracting four measurements on the left. Inset: complex FFT of the quadrature Ramsey interference. The FFT frequency is shifted due to insufficient sampling rate.

full complex Fourier transform can be obtained. It is also useful to implement phase cycling to improve the signal-to-noise ratio (SNR). Spurious noise, misalignments of the microwave pulses, and astigmatism in the phase response of the microwave sources can all contribute to noise in the measured fluorescence contrast, and similar approaches are regularly used in conventional NMR [6]. By cycling the phases of the first and second MW pulses so that the NV spin is rotated alternately to the $\pm x$ and $\pm y$ directions and back to the $\pm z$ direction, one can either add or subtract the measured contrast to remove background noise. Fig. 3.10 demonstrates this approach. By subtracting different phase Ramsey measurements according to table 3.1, the baseline of ΔI is canceled. Also, a complex FFT is permitted by both sin and cos components, which is peaking at Lamour frequency 2.713 GHz for 0 to $|-1\rangle$ transition.

3.5.2 Hyperfine coupling to ^{14}N

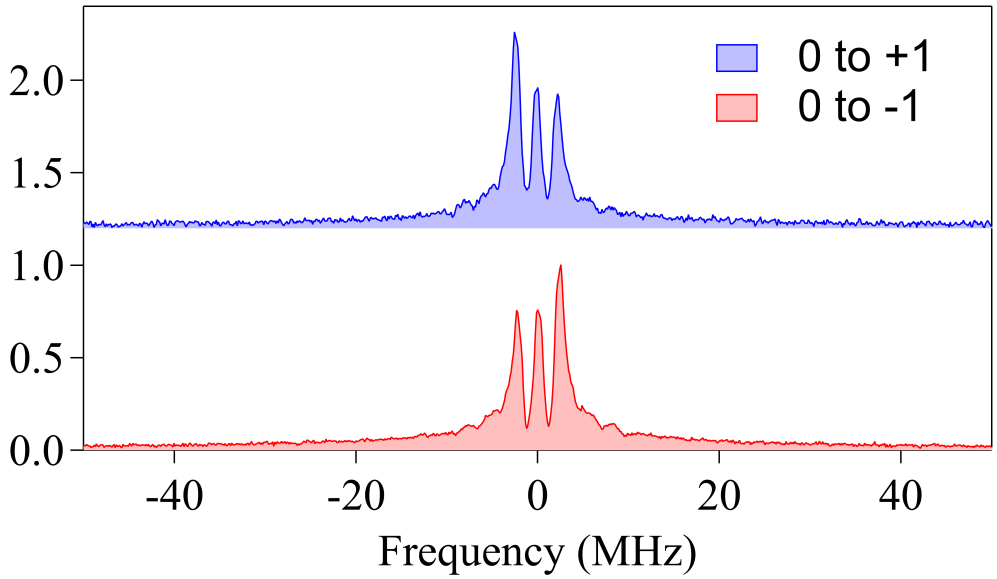

Figure 3.11: Ramsey spectra for both $|m_S = 0\rangle$ to $|m_S = \pm 1\rangle$ transitions. The three peaks are attributed to hyperfine coupling between ^{14}N nuclear spins

Note that the complex FFT spectrum of Ramsey reveals three separate peaks,

which arise due to the hyperfine coupling between the NV spin, S, and the ^{14}N nuclear spin, $I = 1$ (natural abundance 99.6%). The hyperfine coupling is given by $\mathcal{H}_{hf} = \hat{\mathbf{S}} \cdot \mathbb{A} \cdot \hat{\mathbf{I}}$, where the coupling tensor $\mathbb{A}$ is diagonal along the NV-axis with components $A_{||} = 2.1$ and $A_{\perp} = 2.3$ MHz [30].

For simplicity, we just consider secular parts (diagonal terms in the S_z basis [74]) for now. Then the full ^{14}N-NV Hamiltonian can be written as:

$$H_{NV-^{14}N} = DS_z^2 + \omega_S S_z + A_{||} S_z I_z + QI_z^2 + \omega_I I_z, \tag{3.9}$$

where $D = 2870$ MHz, $Q = -5.01$ MHz, ω_S is in the order of 100 MHz and ω_I is in the order of 100 kHz.

For optical transitions between ground and excited state, since it is mainly dominated by NV electron transition dipole moment [18], the nuclear spin m_I should be preserved during the transitions. Therefore the three transitions from $m_S = 0$ to $m_S = -1$ are:

$$E_{m_I=-1} = D - \omega_S + A_{||} \tag{3.10}$$

$$E_{m_I=0} = D - \omega_S \tag{3.11}$$

$$E_{m_I=+1} = D - \omega_S - A_{||} \tag{3.12}$$

The three lines are in consistent with the results in Fig. 3.11, which corresponds to a hyperfine field of 0, ± 2.1 MHz. Likewise, the $m_S = 0$ to $m_S = +1$ transitions are the same structure except the hyperfine field has the opposite sign. If we focus on the intensity of three peaks, we can find that the $m_I = -1$ always has a higher contrast. This is due to the laser pumping leads to higher probability of lowest energy state $|m_S = 0, m_I = -1\rangle$. In other words, the laser pumping not only polarize the NV spin, it also polarizes the nearby ^{14}N nuclear spin in some levels, which plays an important

role in quantum computation [81].

Note that the quadruple interaction Q does not contribute to the ^{14}N hyperfine structure. It also prevents Ramsey interference modulation from misaligned transverse magnetic field. For a ^{15}N enriched NV sample, the Ramsey signal has electron spin echo envelope modulation (ESEEM) since ^{15}N has $I = 1/2$ [64].

3.5.3 Off-resonance response

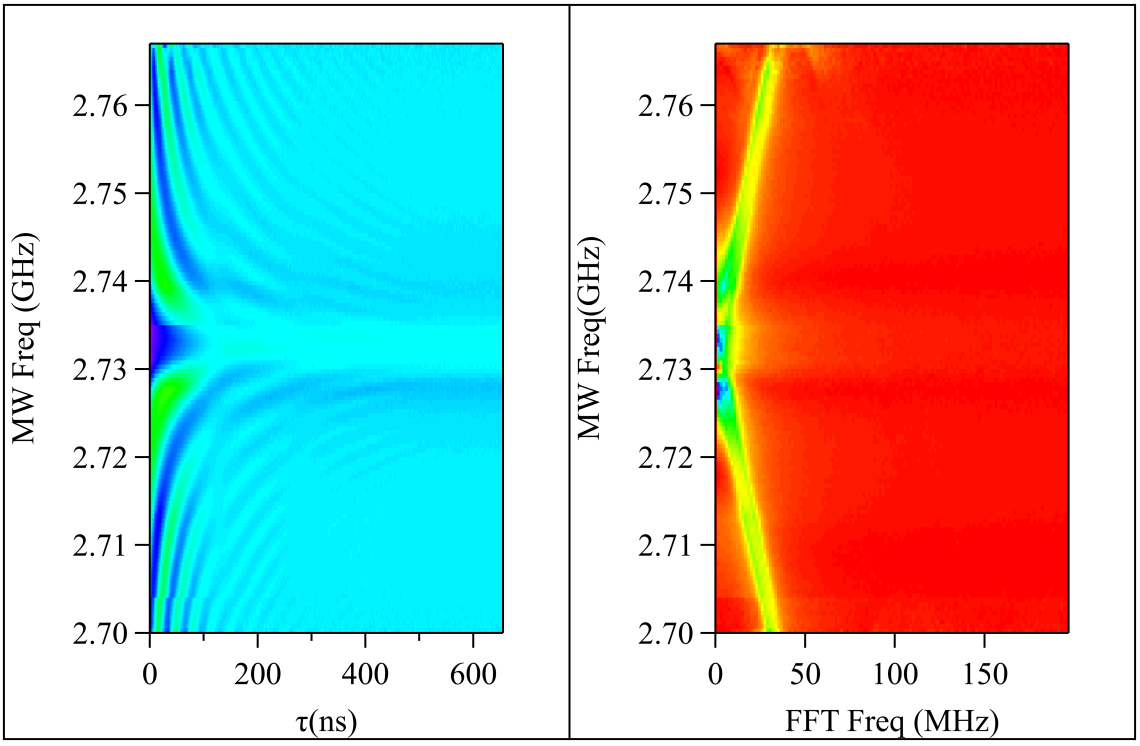

Figure 3.12: Left: Ramsey interference versus τ at different MW pulse frequency. The color indicates the signal contrast ΔI. The data is measured in rotating frame by choose proper τ steps. Right: FFT of τ at different MW frequencies.

The discussions in previous sections assume that the MW pulse frequency matches the two-level energy gap. In practice, it is common that these two frequencies are mismatched: $\delta\omega = \omega_\Delta - \omega_{MW} \neq 0$. In the rotating frame, the qubit phase can be represented as $\phi' = \omega_\Delta \tau - \omega_{MW}\tau = \delta\omega\tau$. As a result, the Ramsey interference should vary as $\sin(\delta\omega\tau)$, which is shown in Fig. 3.12. The Ramsey fringes increase

as the absolute value $|\delta\omega|$ grows, and the FFT indicates that Ramsey frequency is linearly proportional to $|\delta\omega|$. Besides frequency, the signal contrast drops as $|\delta\omega|$ grows, which is due to that the excitation window in the frequency domain decays like a sinc function.

3.6 Dynamical decoupling sequences

3.6.1 Spin echo

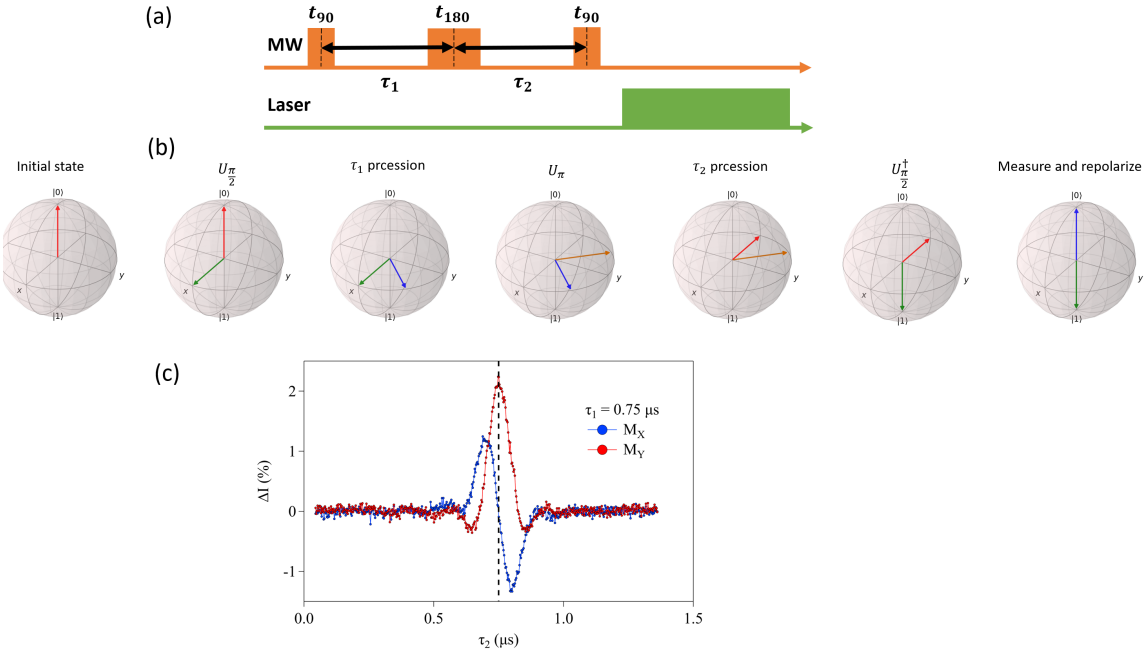

Figure 3.13: (a) Spin echo time sequence (b) NV spin state in Bloch sphere as time evolves (c) Typical spin echo τ_2 sweep with fixed τ_1. The echo appears when $\tau_2 = \tau_1$. Blue and red data are two quadrature channels.

One effective method to extend the coherence time is the spin echo, which is widely used in NMR and MRI. The difference between a Ramsey (Fig. 3.9(a)) and a spin echo sequence (Fig. 3.13(a)) is an extra π pulse in the middle of two $\pi/2$ pulses. The NV spin evolution is shown in Fig. 3.13(b). If the dephasing arises from a static field H_0 inhomegenity, it makes some of the NVs evolve faster and some slower. The

π pulse inverses all the NV spins so that they are refocused to the same phase when $\tau_1 = \tau_2$. This idea is demonstrated in Fig. 3.13(c). The signal contrast starts to rise when τ_2 approaches τ_1. Although the peak width in τ_2 is still dominated by T_2^*, the overall coherence time (peak position) has been extended.

The spin echo can also be used to measure the new coherence time T_2 with less dephasing – by sweeping $\tau = \tau_1 = \tau_2$. The T_2 measurements for different NV diamond sample are displayed in Fig. 2.1. Although T_2 is no longer affected by static and slowly-varying inhomogeneities, it is still limited by fast varying fields originated from dipolar coupling to other spins (NVs, ^{14}N). The coupling usually can be reduced by decreasing the NV conceration [7].

3.6.2 Carr-Purcell-Meiboom-Gill (CPMG) sequences

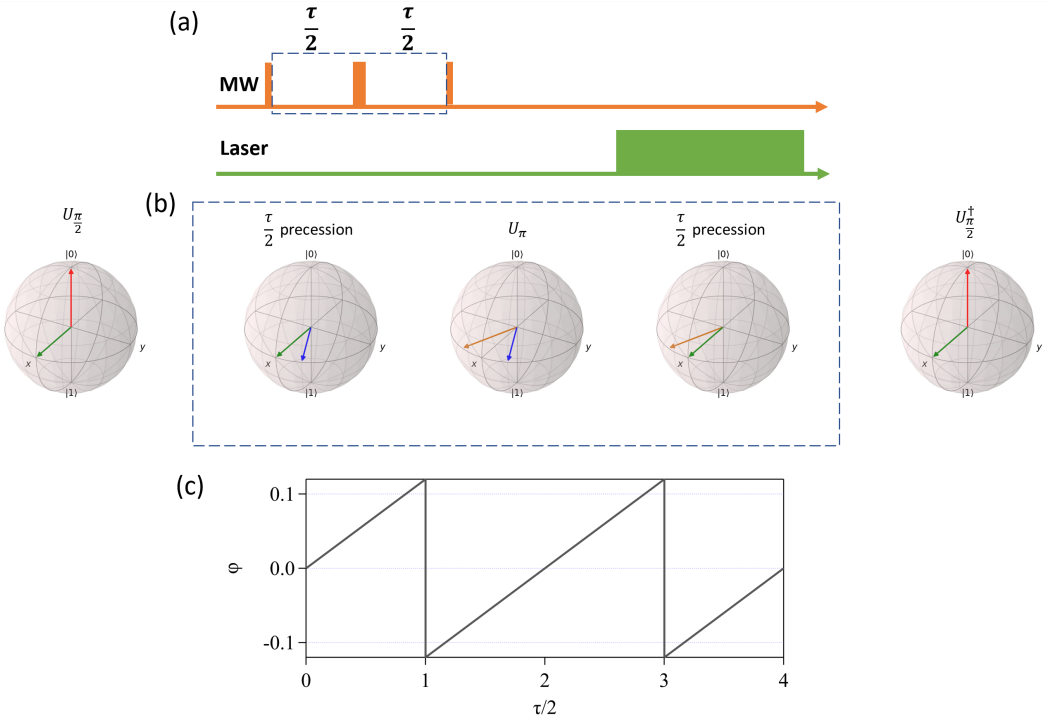

Figure 3.14: (a) CPMG-N time sequence (b) NV spin state MW manipulation in Bloch sphere. The dashed box is repeated by N times (c) The qubit phase ϕ as time evolves under static magnetic field when $N = 2$. The pulse is ideal so that $t_{MW} \to 0$

As we have already seen, the spin echo can extend the coherence time from T_2^* to T_2. This advantage can be amplified by introducing more π pulses in the middle of the sequence. These kind of MW sequences with multiple refocusing are called CPMG-N sequences [17, 56], where N is the repeating number of π pulses. The MW sequences for CPMG-N is shown in Fig. 3.14(a). the interrogation time between π pulses is τ whereas time between π pulse and $\pi/2$ pulse is $\tau/2$. During the cycles (dashed box in Fig. 3.14(a)(b)), the NV spin keeps refocusing and retains the initial phase at the end of the cycle under the static field. In other words, the dephasing contributing to T_2^* is removed by repeating the refocusing. In principle, the coherence time of CPMG T_2^{CPMG} should obey $T_2^{echo} < T_2^{CPMG} < N * T_2^{echo}$, which extends the coherence even longer. To be specific, the CPMG is a form of dynamical decoupling sequence, which can seperate the NV spin from its environment. On the other hand, phase can be accumulated in the presence of an oscillating magnetic field, and the sensitivity is proportional to the repeat time reciprocal $1/N$. More details will be discussed in next section.

3.6.3 XY8-n sequences

Besides CPMG, there are other types of dynamical decoupling sequences such as XY8-n [35]. As shown in Fig. 3.15(a), the XY8-n sequence consists of multiples of a sub-sequence of eight π pulses. Here, n is the number of cycles indicating that the repeat number $N = 8n$. The refocusing π pulses are imposed on either the x or y axis in a symmetric way, whereas CPMG sequences only apply them along a single direction (Fig. 3.15). It turns out that the multi-axis refocusing can reduce the effect of pulse errors and maintain a good coherence performance for different repeat number N [2]. In practice, we find that XY8-n sequences indeed have a much longer coherence time per pulse (T_2/N) for larger repeat number ($N \sim 50$).

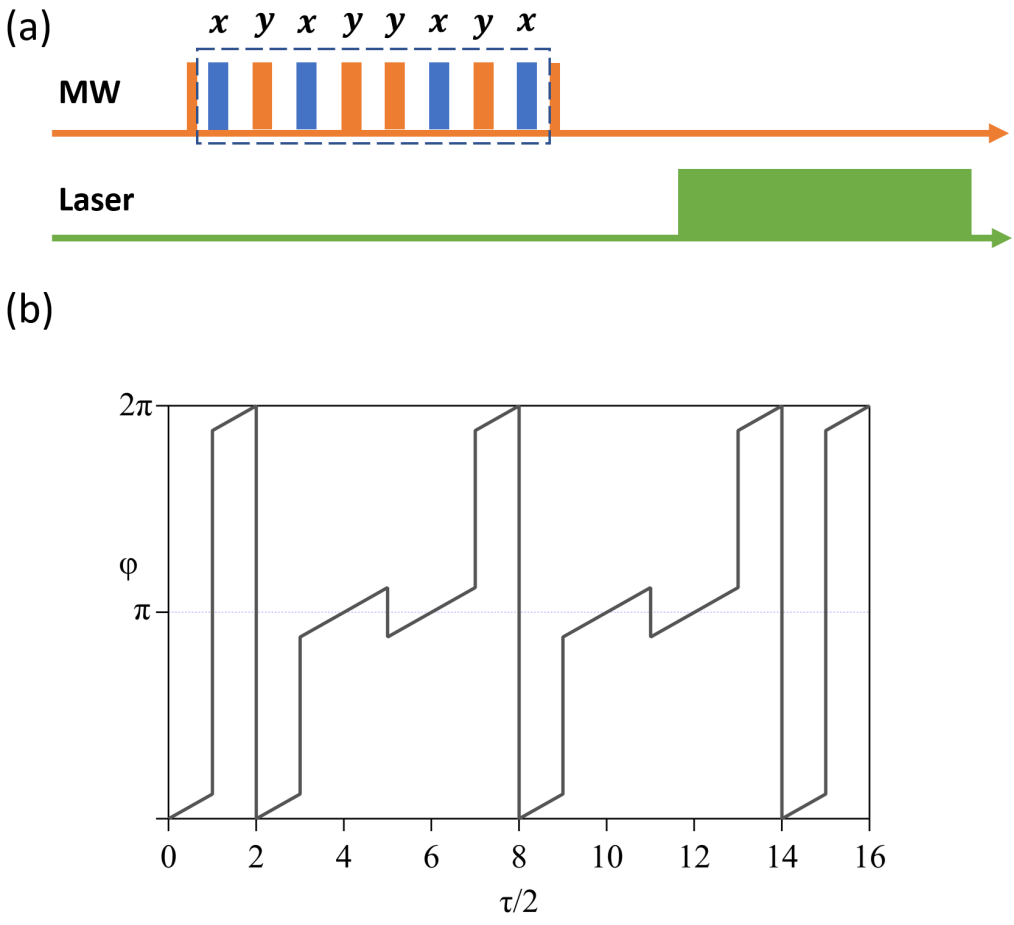

Figure 3.15: (a) XY8-n time sequence. The dashed box is repeated by n times. The spacing between π pulses is τ while that between π and $\pi/2$ pulses is $\tau/2$. (b) The qubit phase ϕ versus evolution time τ under static magnetic field during the dashed box cycling. The pulse is ideal so that t_{MW} is infinitely-narrow in time

3.6.4 Coherence extension

Fig. 3.16 shows the coherence time for different MW sequences. For the dense concentrated NV sample (sample A), its coherence time has been extended from 100 ns (Ramsey) to 1 μs (spin echo) and 20 μs (XY8-n). Meanwhile for low concentrated NV sample (sample B), its coherence time under spin echo T_2 is already 80 μs, and we should expect its coherence time with XY8-n to be in ms scale (black line), which, however, is beyond the memory of the arbitrary waveform generator. The significant dip on the curve is due to the oscillating field from ^{13}C nuclear spin, which is going

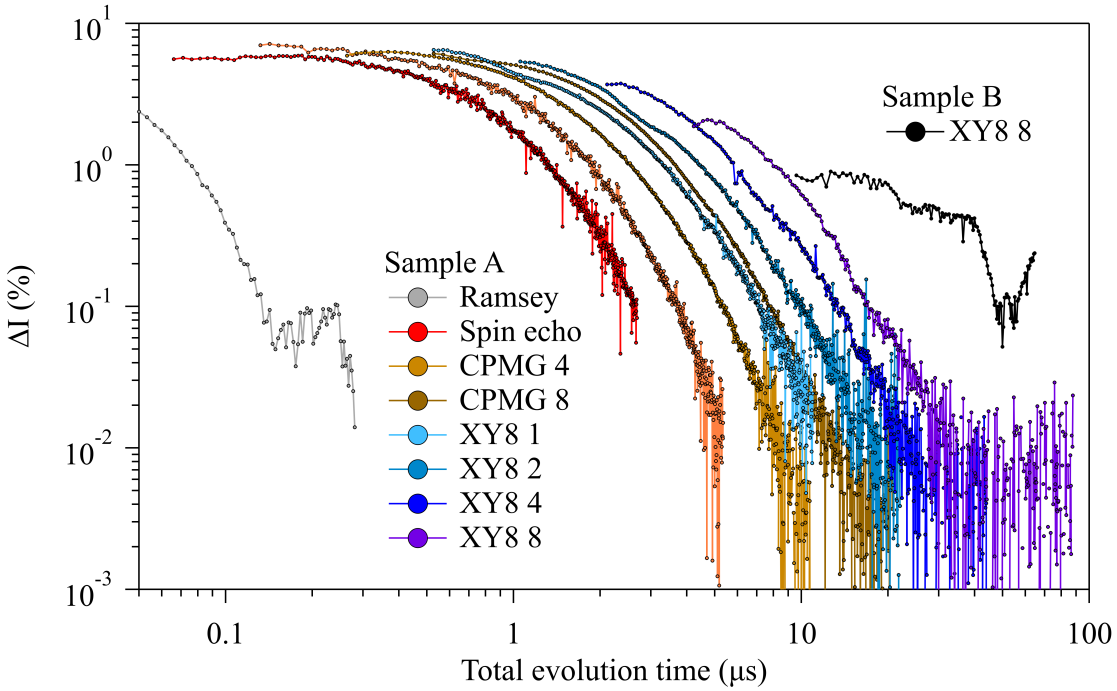

Figure 3.16: Signal contrast ΔI as a function of evolution time for several different MW pulse-train sequences. Sample A and B are defined in Fig. 2.2.

to be discussed in the next section.

3.7 AC magnetometry metrology

Our task in this section is to introduce a basic set of ac sensing protocols. Assuming the target AC signal is coupling to the NV spin via the Hamiltonian:

$$\mathrm{H}_{ac}(t) = \gamma h_{ac} \sin(\omega_{ac} t + \alpha) S_z, \tag{3.13}$$

where h_{ac} is the field amplitude present at the NV site. In the rotating frame, the qubit phase accumulated by the AC signal is $\phi(t) = \gamma \int_0^t h_{ac}(t')dt'$. For the MW sequences like Ramsey, the overall phase accumulation during the interrogation time τ, is small since the positive and negative phase contributions from the sine function almost cancel each other. However, for MW sequences like CPMG and XY8-n, the

π pulses effectively reverse the direction of $\mathbf{h}_{ac}(t)$, and therefore reverse the direction of precession. For a series of π pulses spaced at regular intervals, τ, the phase of the NV can be written as [22]:

$$\phi(t) = \gamma \int_0^t h_{eff}(t')dt', \tag{3.14}$$

where the effective field is $h_{eff}(t) = u(t)h_{ac}(t)$, and $u(t)$ alternates between successive π pulses (which we approximate as infinitely-narrow in time).

Expanding as a Fourier series, the effective field can be expressed as:

$$\begin{aligned} h_{eff}(t) &= h_{ac} \sum_{n=1,3,\cdots} \frac{2}{n\pi} \left[\cos((\omega_{ac} - n\pi/\tau)t - \alpha)\right. \\ &\quad \left. - \cos((\omega_{ac} + n\pi/\tau)t + \alpha)\right]. \end{aligned} \tag{3.15}$$

Most of these frequency components are integrated to nearly zero in Eq. 3.14, which reflects the fact that such pulse sequences filter out noise sources with frequency components far from $n\pi/\tau$. On the other hand, if $n\pi/\tau \approx \omega_{ac}$, $h_{eff}(t)$ has a component that is nearly constant over time and the phase ϕ has a relative large phase accumulation. For $n = 1$, where the pulse spacing $\tau \approx \pi/\omega_{ac}$,

$$\phi(t) = \frac{2\gamma h_{ac} t}{\pi} \mathrm{sinc}(\pi\delta f t)\cos(\pi\delta f t - \alpha) \tag{3.16}$$

where $\delta f = (2\tau)^{-1} - \omega_{ac}/(2\pi)$ is the frequency offset.

If the AC signal arises from sources such as a test signal coil or a spin's in-plane magnetization, then the signal initial phase α should be single valued. In this case if the pulse spacing is tuned exactly such that $\delta f = 0$, then the phase accumulates linearly with time. After accumulating this phase for a series of N pulses, the qubit can then be measured at S_z basis. The final fluorescence signal contrast ΔI depends

on the relative phase of the first and last $\pi/2$ pulses, and ΔI varies as:

$$\Delta I_1 = \begin{cases} \cos\left(2N\frac{\gamma h_{ac}}{\omega_{ac}}\cos\alpha\right) & \text{for } 90_x - 90_x \\ \sin\left(2N\frac{\gamma h_{ac}}{\omega_{ac}}\cos\alpha\right) & \text{for } 90_x - 90_y \end{cases} \tag{3.17}$$

Let's define $\Phi = 2N\frac{\gamma h_{ac}}{\omega_{ac}}$ which is the maximum phase that can be accumulated. Assuming the AC signal is so small such that $\gamma h_{ac} \ll \omega_{ac}$ ($\Phi \ll 1$), then the contrast can be simplified as:

$$\Delta I_1 \sim \begin{cases} 1 - (\Phi\cos\alpha)^2/2 & \text{for } 90_x - 90_x \\ \Phi\cos\alpha & \text{for } 90_x - 90_y \end{cases} \tag{3.18}$$

If the AC signal arises from sources such as statistically polarized spins, the initial phase α is randomized. In general, the probability distribution of α should be unbiased, therefore when $\delta f = 0$, the signal contrast ΔI can be integrated to be:

$$\Delta I_2 = \begin{cases} J_0(\Phi) & \text{for } 90_x - 90_x \\ 0 & \text{for } 90_x - 90_y \end{cases} \tag{3.19}$$

where $J_0(x)$ is the zero order Bessel function of the first kind. When h_{ac} is small, it is given by:

$$\Delta I_2 \sim \begin{cases} 1 - (\Phi/2)^2 & \text{for } 90_x - 90_x \\ 0 & \text{for } 90_x - 90_y \end{cases} \tag{3.20}$$

In short, for both single and randomized phase AC signal, the dynamical decoupling sequences can give rise to a qubit phase when $\delta f \sim 0$. Based on this concept, some approaches have been developed to measure the AC frequency ω_{ac} and the amplitude h_{ac}.

3.7.1 Pulse-spacing sweep

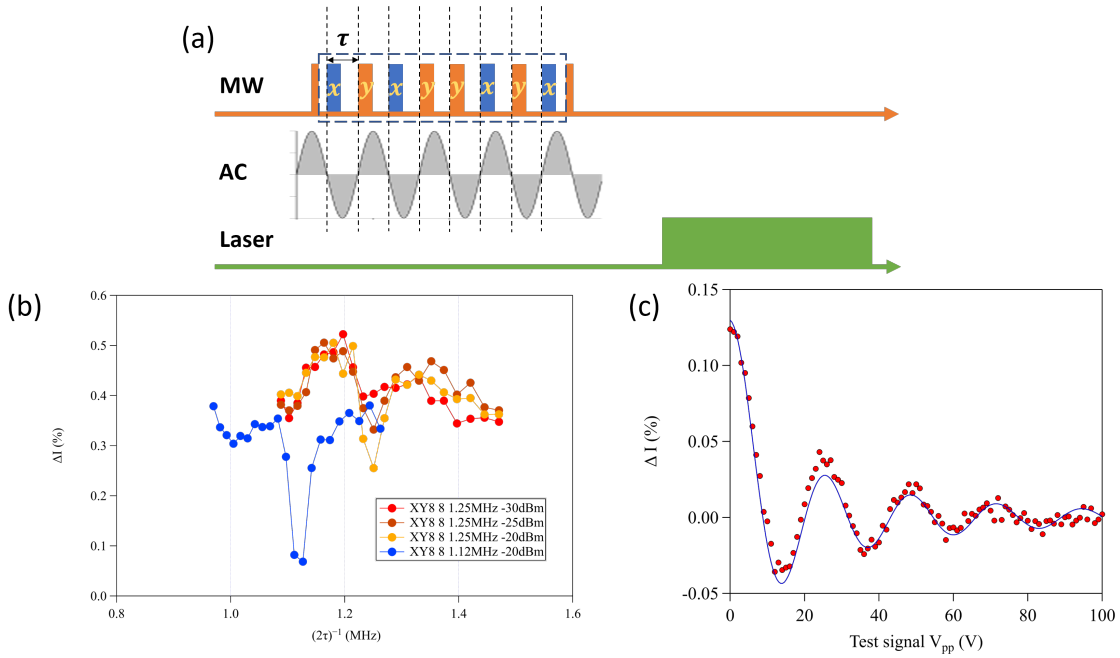

Figure 3.17: (a) XY8-n MW sequence compatible with the AC signal. The dashed box is repeated by n times. (b) Signal contrast ΔI versus the detection frequency, $(2\tau)^{-1}$, where τ is the pulse spacing of a dynamical decoupling sequence. Input signals of 1.12 and 1.25 MHz were test signals introduced externally. The dip in the contrast arises due to the phase accumulated by the NV centers. (c) ΔI of a test AC signal measured by signal averaging as a function of the voltage applied to the external AC coil. The solid line is a fit to zero order Bessel function of the first kind.

Since the NV signal contrast ΔI always has a decrease for $90_x - 90_x$ channel when $\delta f = 0$, one can sweep the interrogation time, τ, and measure the response on ΔI. Fig. 3.17 explains this approach. The data was measured with a external AC coil, which can generate AC fields ranging from nT to μT. Even though the test signal is single phased, the signal's initial phase at the beginning of each cycle is randomized. Hence for measurements averaged many times, the test signal phase α can be treated as an uniformly distributed random variable. For a XY8-8 sequences, the signal contrast shows significant dip when $(2\tau)^{-1} = \omega_{ac}/(2\pi)$ as expected in Eq. 3.20 (see Fig. 3.17(b)). When the signal amplitude h_{ac} is not so small, the signal contrast should obey the Bessel function in Eq. 3.19. This behavior is illustrated in

Fig. 3.17(c), in which the AC voltage, V_{pp} is varied to change the magnitude of h_{ac}. In this case, $h_{ac} \propto V_{pp}$.

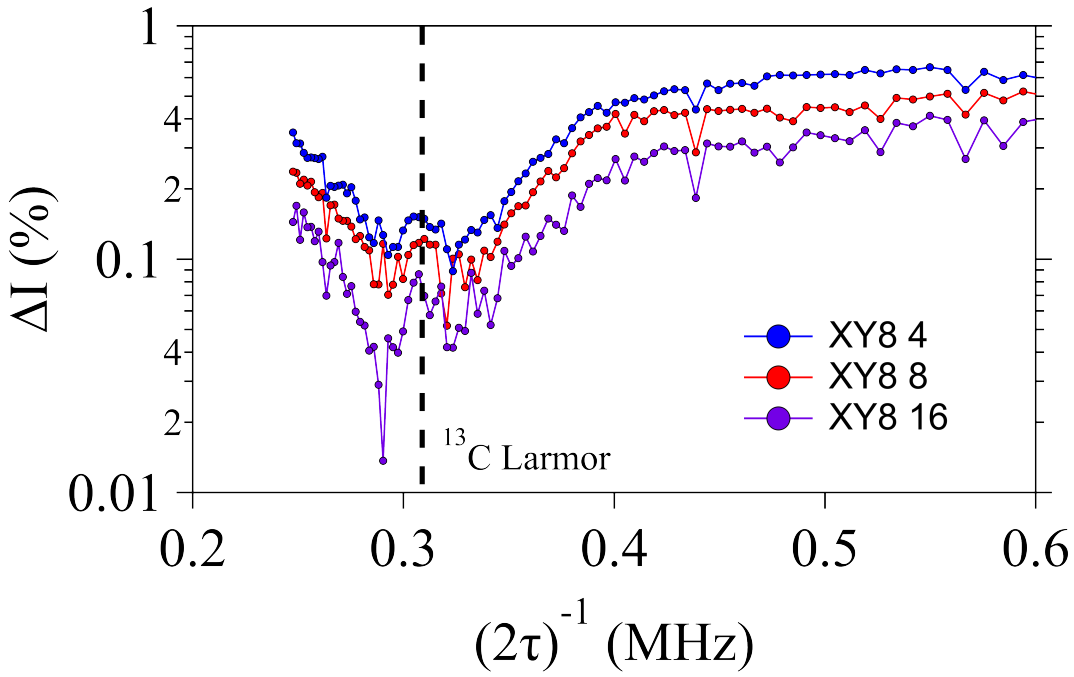

Figure 3.18: The signal contrast versus detection frequency, $(2\tau)^{-1}$, where τ is the pulse spacing of XY8 sequences, measured at various repeating number n. The dip around 0.3 MHz arises from precessing ^{13}C spins in the diamond lattice. The dashed line indicates ^{13}C Larmor frequency under a external field $H_0 = 288.58$ G.

Besides the test signal, this approach can also be used to detect nuclear spins processing near the NV centers. Fig. 3.18 shows pulse sweep measurements with various XY8-n sequences. As one can see, the dips around $f_{^{13}C} = 0.309$ MHz is enlarged as n grows, indicating that dips belong to some AC signal sources. The big dip is divided into two parts by ^{13}C's Larmor frequency (dashed line), which can be explained by ^{13}C spins with an magnetic shift from the hyperfine coupling to the nearby NV. The magnetic shift is about ± 20 KHz (± 6.5 %), which is too big to be dipolar coupling to other nuclear spins. Although the origins of this detailed structure are unclear, it is straightforward that we can detect the nuclear spins and the hyperfine structure using these dynamical decoupling methods.

3.7.2 Correlation spectroscopy

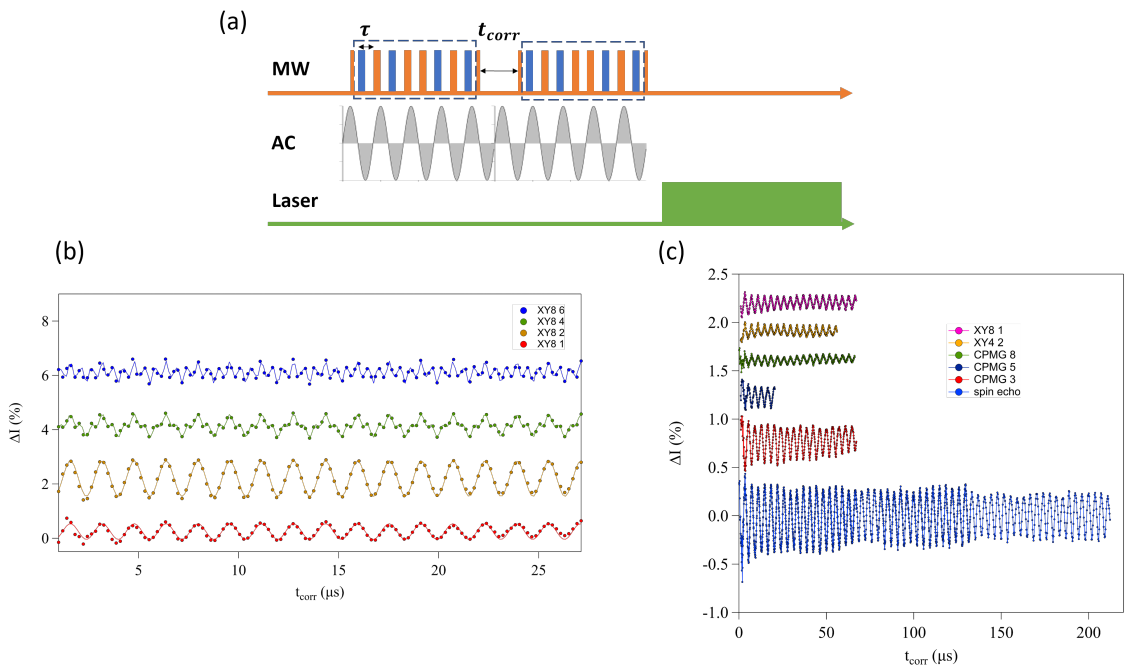

Figure 3.19: XY8-n correlation spectroscopy MW sequence compatible with the AC signal. The dashed box is repeated by n times. (b) Signal contrast ΔI versus free evolution period, t_{corr}. Test signal frequency was 625 kHz. Solid curves are fittings using Eq. 3.21. (c) ΔI versus t_{corr} for ^{13}C nuclear spins. The ^{13}C Larmor frequency is $f_{^{13}C}$ =0.270 MHz.

For the pulse sweep method, the frequency bandwidth is determined by the total evolution time $\Delta f \sim 1/T_2$. In order to further narrow down the bandwidth, a correlation spectroscopy method has been developed. The idea is illustrated in Fig. 3.19(a). The MW sequence is subdivided into two equal sensing periods of duration $N\tau$ that are separated by an incremented free evolution period t_{corr}. When $\delta f = 0$, the first sensing sequence picks up phase $\phi_1 = \Phi \cos\alpha$ and store in the qubit. If the AC signal is still correlated after t_{corr}, the initial phase at the beginning of second sensing sequence is $\alpha^{'} = \alpha + N\pi + \omega_{ac} t_{corr}$. Again the sensing sequence picks up phase $\phi_2 = \Phi \cos\alpha^{'}$ Eventually, the signal contrast after readout can be written as [22]:

$$\Delta I_3 = \sin\left(\Phi\cos\alpha\right)\sin\left(\Phi\cos(\alpha + \omega_{ac} t_{corr})\right) \text{ for } 90_x - 90_y \; 90_x - 90_y, \tag{3.21}$$

When Φ is small, ΔI_3 becomes:

$$\Delta I_3 \sim \Phi^2 \cos\alpha \cos(\alpha + \omega_{ac} t_{corr}) \text{ for } 90_x - 90_y \; 90_x - 90_y \tag{3.22}$$

By sweeping the free evolution period t_{corr}, an oscillation at target frequency ω_{ac} can be obtained. Since during t_{corr} the phase is stored in the S_z basis, the coherence is limited by T_1 instead of T_2. Hence the bandwidth can be improved to be $\Delta f \sim 1/T_1$.

Fig. 3.19(b)(c) display the correlation spectra detecting test signal and ^{13}C nuclear spins respectively. The test signal can be well explained by integrating α in Eq. 3.21 using a uniform distribution. The solid curves are fittings with different Φ values and the target frequency is consistent with the preset value 625 kHz. The ^{13}C correlations reveal oscillation at $f_{^{13}C} = 271.3 \pm 4.1$ kHz (spin echo), which is consistent with ^{13}C Larmor freqency under external field $H_0 = 251.88$ G. The signal contrast is still at the same level when $t_{corr} \sim 200\mu$s, showing that the coherence is not limited by T_2. On the other hand, it is obvious that the waveforms of ^{13}C do not show any significant repeating number N dependence – unlike the test signal data, different colored curves have almost the same shape, which suggests that AC signal from ^{13}C cannot be simply modeled as a constant amplitude and frequency sine wave with a uniform randomized phase (Eq. 3.13). Future studies are required to understand these correlation spectra in more detail.

3.7.3 Synchronized readout

Though the methods above have already pushed the bandwidth to the limit of NV qubit's lifetime (T_1 and T_2), it is still possible to push the limit further. Here we introduce a method that is independent of NV's coherence time, which is analogous to classical heterodyne detection in that an unknown signal is "mixed" with a local oscillator [70, 33]. The idea is illustrated in Fig. 3.20(a). Unlike the pulse sweep

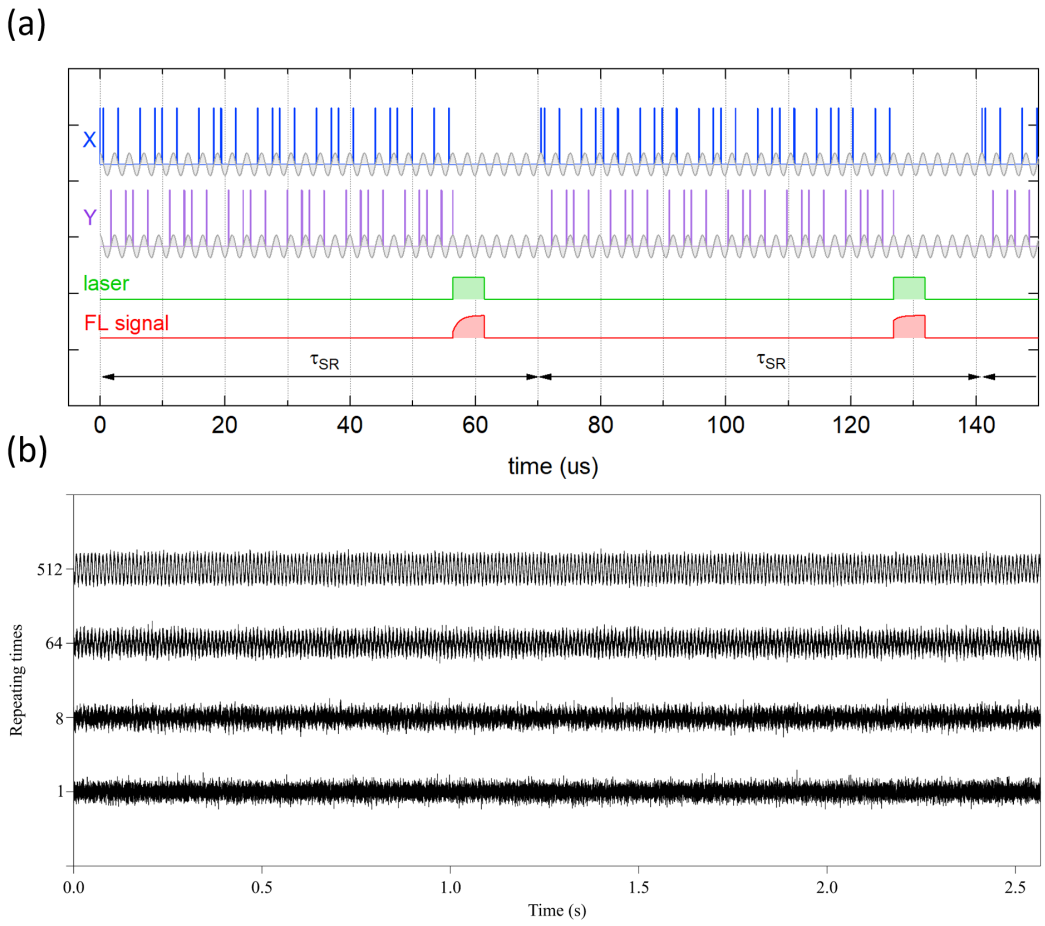

Figure 3.20: (a) XY8-n synchronized readout timing control. X and Y stand for π pulses applying on X and Y axis respectively. (b) synchronized readout of a test AC signal. The y axis stands for scan times N_{scan}. The total measuring time is $T_{tot} = N_{scan}T_{meas}$, where T_{meas} is measuring time for individual scan. In this experiment XY8-20 sequence is used. $\tau = 0.833\mu$s, $f_{ac} = 1.2001$ MHz, $\tau_{SR} = 78.333$ μs, $T_{meas} = 2.567$s.

approach, where initial phase of the AC signal at the start of each cycle, α, is uniformly random, here we set the total cycle time to an even integer multiple of interrogation time τ: $\tau_{SR} = 2n\tau$ (as displayed in Fig. 3.20). Therefore the initial phase at the m^{th} cycle could be written as:

$$\begin{aligned} \alpha_m &= m\omega_{ac}\tau_{SR} + \alpha_0 && (3.23) \\ &= 2\pi(f_{ac} - (2\tau)^{-1})m\tau_{SR} + 2n\pi + \alpha_0, && (3.24) \end{aligned}$$

where $\delta f \equiv f_{ac} - (2\tau)^{-1}$ is the frequency offset. As a result, the signal contrast at the m^{th} cycle should be:

$$\Delta I(m\tau_{SR}) = \begin{cases} \cos\left(\Phi\cos(2\pi\delta f m\tau_{SR} + \alpha_0)\right) & \text{for } 90_x - 90_x \\ \sin\left(\Phi\cos(2\pi\delta f m\tau_{SR} + \alpha_0)\right) & \text{for } 90_x - 90_y \end{cases} \tag{3.25}$$

For small Φ, this quantity becomes:

$$\Delta I(m\tau_{SR}) \sim \begin{cases} 1 - (\Phi\cos(2\pi\delta f m\tau_{SR} + \alpha_0))^2/2 & \text{for } 90_x - 90_x \\ \Phi\cos(2\pi\delta f m\tau_{SR} + \alpha_0) & \text{for } 90_x - 90_y \end{cases} \tag{3.26}$$

Fig. 3.20(b) shows several time-series signals produced by AC fields generated by a copper coil located near the NV diamonds. Each point represents a NV fluorescence acquisition result ΔI at the end of each cycle τ_{SR}. For a $90_x - 90_y$ quadrature channel, an oscillation at $\delta f = 100$ Hz emerges as the repeat time increases. The top curve (N = 512) exhibits an oscillation at 99.76 $\pm$ 0.14 Hz, whose bandwidth is dominated by the AC signal's lifetime instead of the NV's.

In order to determine the field sensitivity η_{ac}, defined as:

$$\eta_{ac} = \frac{h_{ac}}{SNR(1)}, \tag{3.27}$$

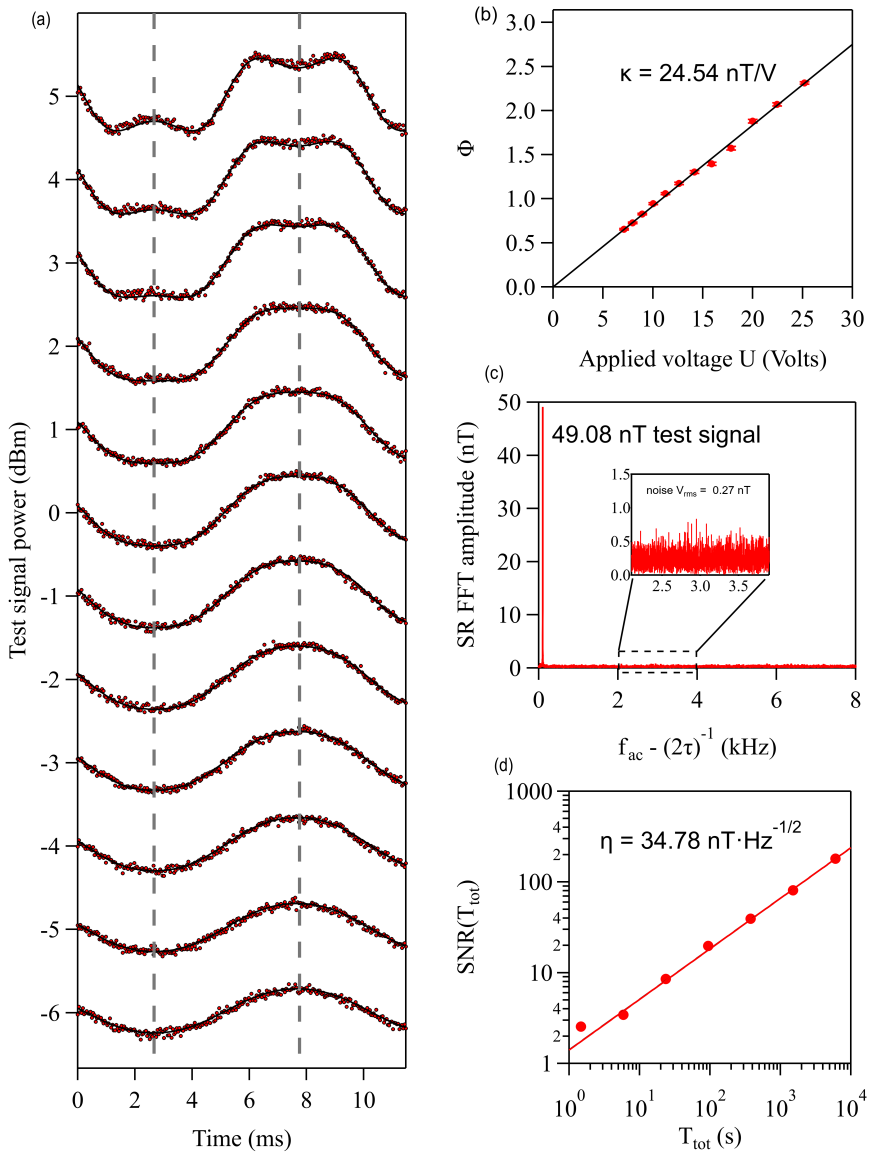

Figure 3.21: (a) Synchronized readout measurements of test signals. The applied voltage for the AC current source of the coil is varied from U = -6 to U = 5 dBm. Each black trace corresponds to a fitting using Eq. 3.25. (b) linear relation between maximum accumulating phase Φ and applied voltage on the coil V_{pp}. The black line stands for linear fit with none intercept. (c) Synchronized readout FFT spectrum of a 49.08 nT (2 V_{pp}) test signal. The calibrated signal amplitude defines the vertical axis of the plot. The inset window shows the frequency range used to estimate the noise in the spectrum. V_{rms} represents the white noise amplitude. (d) Synchronized readout SNR as a function of total measuring time. Black line stands for a power fit mentioned in the text. XY8-10 sequence is used. $\tau =$ 0.833μs, f_{ac} = 1.2001 MHz, τ_{SR} = 45 μs, T_{meas} = 1.475s.

one needs to know the size of the AC field h_{ac} and its corresponding signal-to-noise ratio (SNR) for a single acquisition $SNR(1)$. In practice, we assume that the AC field amplitude is proportional to the applied voltage across the coil: $h_{ac} = \kappa$ U, where U is the applied voltage, and κ is the coupling coefficient. For $90_x - 90_y$ phase in Eq. 3.25, if the m_0-th acquisition obeys $\cos(2\pi\delta f m\tau_{sr} + \alpha_0) = 1$, then signal contrast at that point becomes $\Delta I(m = m_0) = \sin\Phi = \sin\left(2N\frac{\gamma\kappa U}{\omega_{ac}}\right)$, which is a sine function of applied voltage U. Fig. 3.21(a) displays time-series signals with various applied voltages, U. When τ_{sr} equals to the time indicated by dashed lines in Fig. 3.21(a), ΔI is proportional to $\sin\Phi$. By fitting all curves simultaneously, the phase Φ can be obtained (Fig. 3.21(b)) and κ can be calculated to be:

$$\kappa = \frac{\omega_{ac}}{2N\gamma}\frac{\Delta\Phi}{\Delta U} = 24.54 \text{ nT/V} \tag{3.28}$$

On the other hand, the SNR can be obtained by comparing signal and noise intensity in Fig. 3.21(c). For a measurement of 49.08 nT AC signal which has been averaged for $4096T_{meas}$, the noise level can be obtained from baseline root-mean-square (rms) value. If the noise source is white noise, we have:

$$SNR(t) = \frac{N_{scans}T_{meas} * I_{signal}(1)}{\sqrt{N_{scans}T_{meas}} * I_{noise}(1)} = \sqrt{N_{scans}T_{meas}} * SNR(1) \tag{3.29}$$

Replacing $SNR(1)$ with η_{ac}, we obtain:

$$SNR(t) = \frac{h_{ac}}{\eta_{ac}}\sqrt{N_{scans}T_{meas}} \tag{3.30}$$

A power-law fit in Fig. 3.21(d) indicates a square-root scaling with time and a sensitivity of $\eta_{ac} = 34.78 \text{ nT} \cdot \text{Hz}^{-1/2}$.

Although the sensitivity can still be improved by increasing π pulses repeat number and varying τ, it might still be in the order of $\text{nT} \cdot \text{Hz}^{-1/2}$. So as to detect

AC sensing method	Resolution	AC signal type
Pulse-spacing sweep	10 kHz	random or single phase
correlation spectroscopy	1 kHz	random or single phase
Synchronized readout	100 mHz	single phase

Table 3.2: Various AC sensing methods. The resolutions are obtained from sample B.

nuclear polarization outside of the NV diamond, the sensitivity needs to be around 10 pT $\cdot$ Hz$^{-1/2}$ level as reported in [33]. On the other hand, there is a strong AC signal from the ^{13}C nuclear spins as seen in Section 3.7.1 and 3.7.2. This field is created by statistical polarization instead magnetic polarization, which lacks a traceable initial phase α. Thus we are not able to detect the AC signal directly from these local spins.

3.8 Conclusion

The work described in this chapter can be divided into three parts: CW NV ODMR study, pulsed NV ODMR and coherence extension, AC sensing metrology. In the first part we studied the basics of NV spectra and the relation to both the light polarization and the ^{13}C hyperfine interaction. The second part described pulsed ODMR NV control protocols using a qubit with a Bloch sphere. Utilizing dynamical decoupling sequences, the coherence time T_2 can be extended 50 times, which makes AC sensing possible. The third part introduced various methods to detect AC magnetic fields coupling to nearby NV centers. The differences between them are summarized in Table .3.2.

The ultimate goal is to use NV centers to detect nearby environments under extreme physical conditions such as high pressure. Ideally it is straightforward to adapt current methods to the diamond anvil cell (DAC) if the sensitivity is sufficient. In fact, one way to achieve this is to keep the AC sensitivity and enlarge the AC field by hyperpolarization [15]. Nevertheless, the pressure in the DAC makes quantum sensing challenging due to inhomogeneities of the microwave field and pressure. More

details will be discussed in the next chapter.

Chapter 4

AC sensing in a diamond anvil cell

In this chapter, we describe experiments to develop Optical detected magnetic resonance (ODMR) to study AC dynamic fields such as those arising from precessing nuclear spins as a function of pressure in the diamond anvil cell (DAC). In principle there is no upper pressure limit for such measurements, and we will discuss some of the challenges that emerge under pressure as the properties of the NV centers evolve.

4.1 Building ODMR in the DAC

The principle challenges to performing ODMR in a DAC are associated with the collecting sufficient fluorescence (FL) from the sample as well as introducing microwaves with sufficient homogeneity and magnitude. The optical system is the same as that of ambient condition before the final NV sample FL collection, which is shown in Fig. 2.3. The geometry of NV diamond and DAC is displayed in Fig. 4.1. The geometry of the DAC requires a larger working distance, from 0.8 to 0.4 for our case, so the FL intensity is reduced due to a smaller numerical aperture objective. Though the focusing beam size is few μm, the FL collected from focusing spot is too small to generate enough signal to noise ratio (SNR) to achieve AC quantum sensing. Therefore instead of having a confocal microscope setup, we collect all FL signal created by the

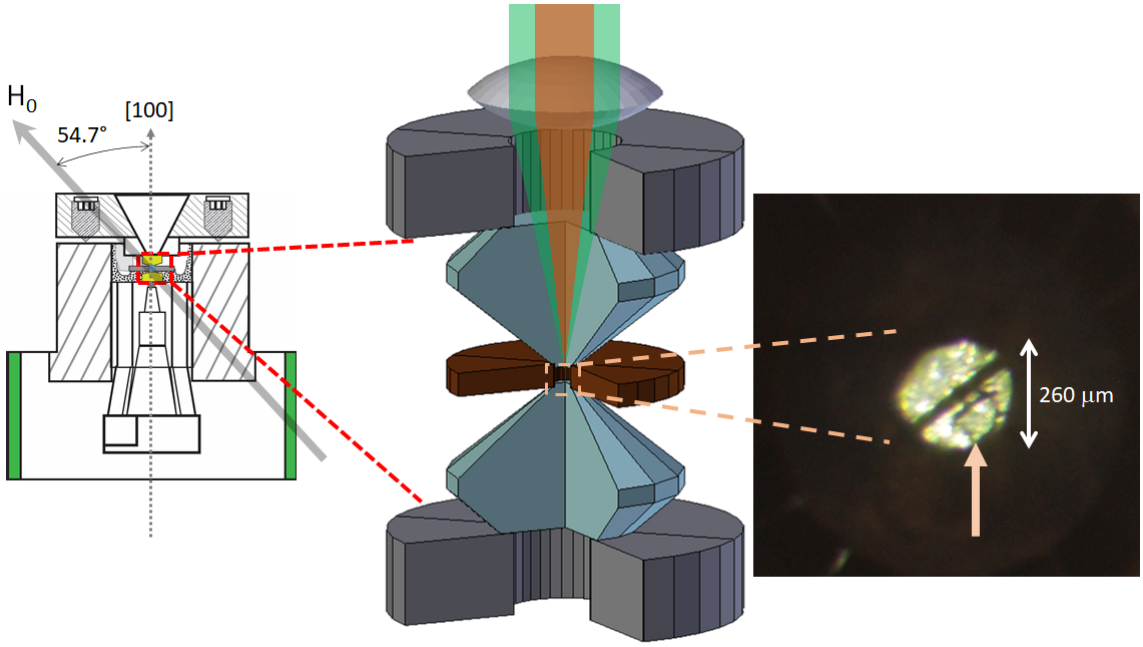

Figure 4.1: Diamond anvil cell for optically-detected magnetic resonance experiments. An objective focuses the excitation light and collects the fluorescence from within the sample space in the gasket. A gold antenna is located across the anvil culet (sample hole 260 μm diameter), and a small NV diamond crystal of dimensions $\sim 100 \times 75$ μm is visible at the center to the lower right of the antenna (see arrow), oriented normal the [100] direction. A magnetic field of magnitude $H_0 \sim 29$ mT is oriented 54.7° from the vertical along the [111] direction of the diamond using permanent neodymium magnets mounted externally.

NV chip.

4.1.1 MW antenna design

Introducing microwaves with sufficient magnitude in close proximity to the NV centers presents a major challenge for working in a DAC, because the conducting gasket can screen out the magnetic field, as illustrated in Fig. 4.2. High microwave amplitudes are necessary in order to achieve strong $\mathbf{H}_1$ fields and hence large Rabi frequencies. The magnitude of $\mathbf{H}_1$ should be ~ 0.18 mT in order to have a 90° pulse time on the order of 50 ns ($\Omega \sim 5$ MHz). Note that it is not necessary to have a high Q resonant circuit, so the antenna does not necessarily need to have a low resistance.

Previous studies have utilized antennas located external to the sample chamber [25, 45, 38, 90], within the sample chamber [71], as well as designer anvils with conducting paths deposited directly onto the diamond culet and protected with a capping layer of CVD grown diamond [77]. Locating the antenna outside the sample space, as shown in Fig. 4.2(a,b), is easier, but is inefficient because a large fraction of the power goes towards inducing screening currents in the conducting gasket and can lead to undesired heating effects. Designer anvils are costly and time consuming to prepare [86].

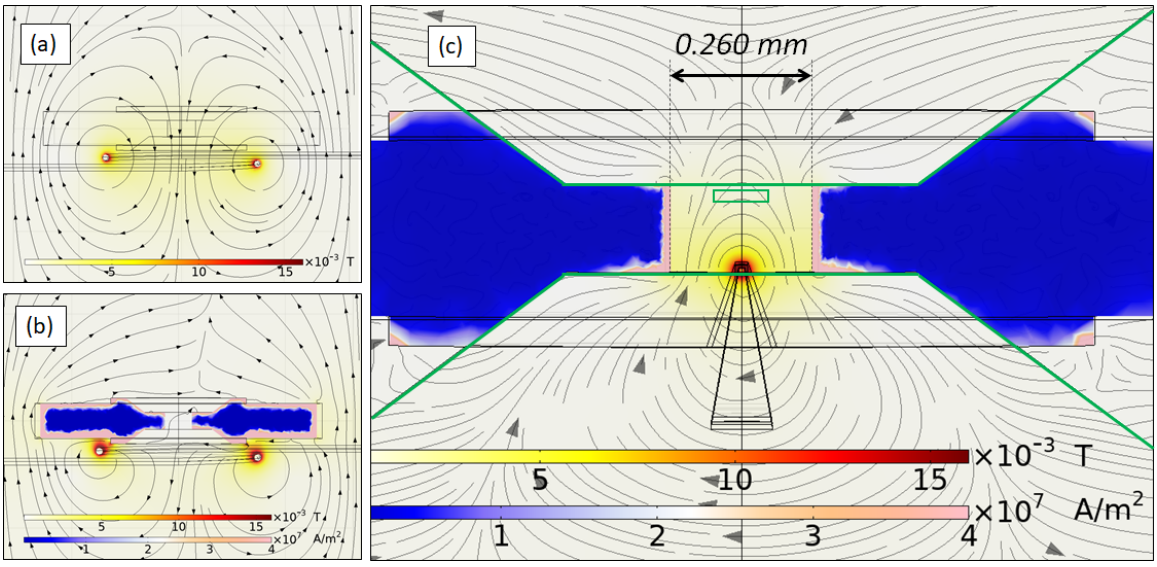

Figure 4.2: Calculated magnetic field profile from a wire loop surrounding a diamond anvil close to (a) an insulating gasket and (b) a conducting gasket for 63.2 V(40 dBm) across the antenna at 3 GHz. The conducting gasket screens the majority of the magnetic field within the sample space. (c) The calculated magnetic field profile and induced current density for a conducting gasket with a straight antenna, as illustrated in Fig. 4.3(a). The diamond anvil (outlined in green) has a relative permeability of 5 [40]. The green rectangle in the sample space represents the volume of the NV diamond chip used to compute the histograms in Fig. 4.4.

To overcome this challenge, we fabricated gold microwave strips, as shown in Fig. 4.3, by electroplating 8 μm thick strips onto a substrate, which were then liberated chemically for insertion into the DAC. A single antenna is then transferred onto the culet of the anvil under a microscope, and secured with thin layer of adhesive. Leads

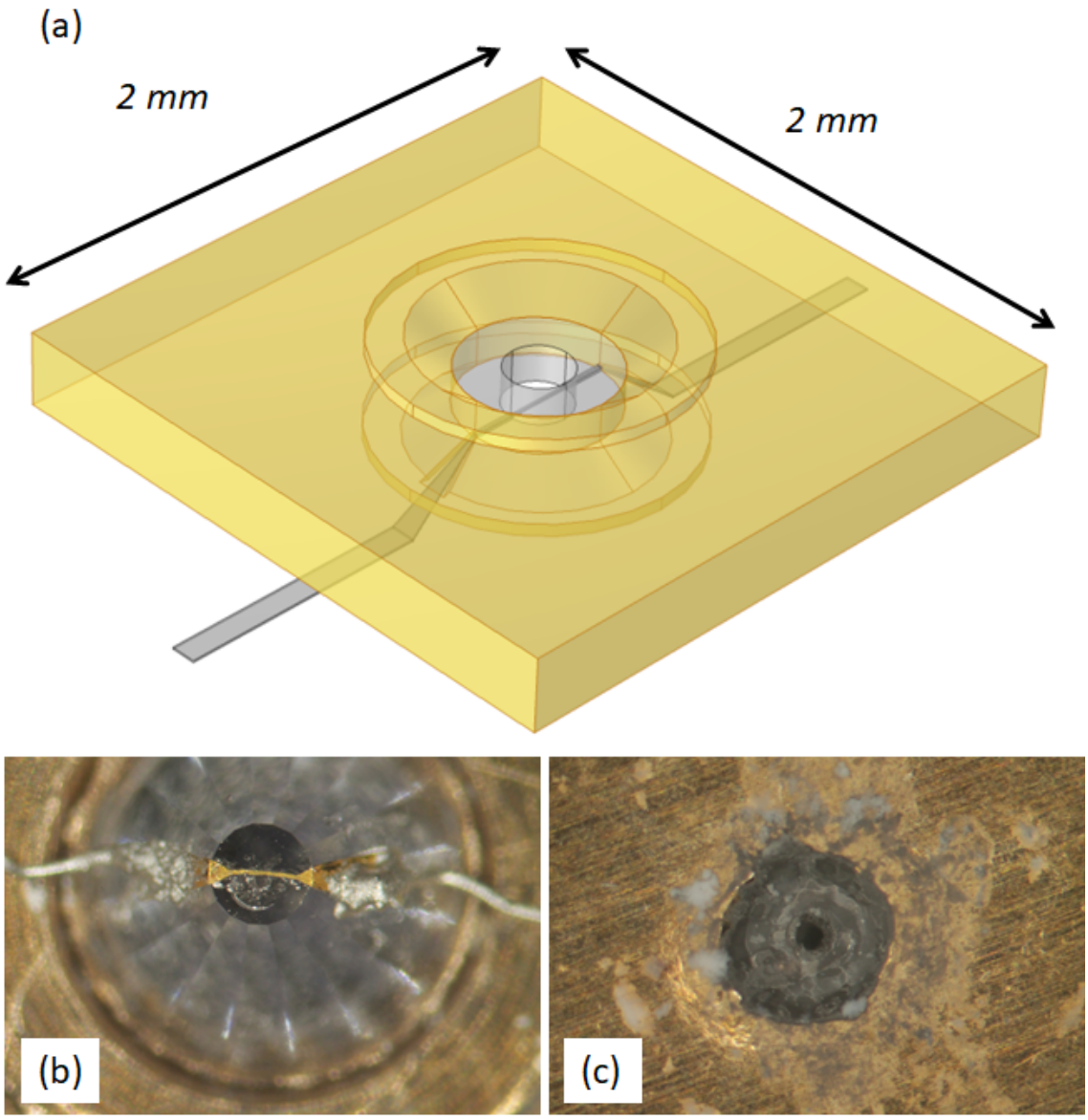

Figure 4.3: (a) Geometry of the gasket and sample region. The inner diameter is 260 μm, the culet diameter is 600 μm, and the thickness of the sample region is 150 μm. The gasket is copper-beryllium with conductivity 1.16×10^7 S/m. The gold antenna has width 11μm, thickness 8 μm and length 600 μm, and has conductivity 4.6×10^7 S/m. There is also a thin insulating layer between the antenna and gasket with conductivity 10^{-18} S/m. (b) Fabricated microwave antenna secured onto culet of the anvil (diameter 600 μm). The antenna has width 10 μm and thickness 8 μm. (c) Pre-indented gasket with insulating layer of boronitride, aluminum oxide and epoxy. The sample space in the center hole has diameter 260 μm.

were attached to the ends of the antenna pads with silver epoxy, and then attached to larger wires (not shown) that lead out of the cell. The antenna is insulated from the pre-indented region of the gasket (Fig. 4.3(c)). This approach enables us to reliably apply pressure to the gasket without comprising the antenna performance. The antenna leads are malleable and are compressed under pressure as the anvil presses into the gasket. In one test[84], the MW power starts to decrease dramatically as pressure reaches 6 GPa. It is very likely due to that the leads get severed as the gasket deforms. Moreover, at higher pressures (on the order of $\sim 10 - 30$ GPa) the anvil will eventually cups inward [57]. In such cases it may be better to utilize alternative designs, such as a wave guide to transfer MW power through the anvil rather than a wire located between the anvil and gasket.

4.1.2 MW field simulation

In order to better understand the $\mathbf{H}_1$ field distribution and radiofrequency screening effects of the gasket, we have modeled the antenna and gasket system and carried out finite element analysis calculations of the electromagnetic fields. Fig. 4.3(a) illustrates the gasket and antenna strip, including the ridge surrounding the indented region around the anvils (not shown). A thin insulating gap separates the antenna from the gasket. Using the COMSOL package, we find that the field radiates radially from the anvil, as illustrated in Fig. 4.2(c), but drops off quickly with distance. The ratio of power dissipated to resistance in the antenna to the radiated power is 3.2%, and that the power dissipated by induced currents in the gasket is 0.5%. These numbers indicate that the thin gold wire radiates power into the sample space efficiently. On the other hand, for a loop antenna located outside the sample space (Fig. 4.2(b)), but in close proximity to the gasket and anvil, the magnetic field in the sample space is well-screened by the conducting gasket.

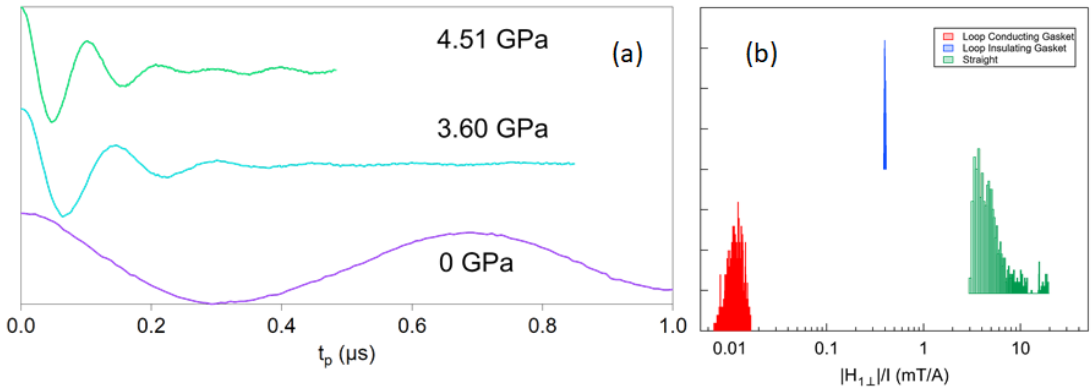

Figure 4.4: (a) Rabi oscillations ($|0\rangle \leftrightarrow |-1\rangle$) for various pressures in the DAC with a microwave power of 44 dBm. (b) Computed histograms of $H_{1\perp}/I$ based upon the finite element simulations shown in Fig. 4.2(c), for for a loop antenna with insulating gasket, with a conducting gasket, and for the straight antenna design illustrated in Fig. 4.3(a). Note that the field has been normalized by the current in the wire and have been computed at 2 GHz.

4.1.3 Rabi oscillations

As seen in Fig. 4.2, the $\mathbf{H}_1$ field profile is inhomogeneous. It is largest in the region closest to the antenna but drops off quickly along the vertical axis. Fig. 4.4(b) displays a histogram of the field to current ratio of magnitude of $\mathbf{H}_{1\perp}$, the component of $\mathbf{H}_1$ perpendicular to $\mathbf{H}_0$ along the [111] direction (see Fig. 4.1), within a volume of $100 \times 75 \times 20$ μm^3 representing the NV diamond (illustrated by the green box in Fig. 4.2(c)). The size and shape of this histogram depends critically on the location of the NV diamond within the sample space. This distribution of fields means that each of the $\sim 8 \times 10^9$ NV centers in the NV diamond experiences a slightly different Rabi frequency. As a result, the oscillations die out faster under pressure, as observed in Fig. 4.4(a). We also considered a loop, rather than a straight antenna, as shown in Fig. 4.4(b). If the gasket remains insulating, the distribution remains narrow. For the conducting gasket, the distribution broadens and is shifted to lower fields because the gasket efficiently screens the field. The highest field to current ratios are achieved with the straight antenna because the distance to the sample is smallest in this case,

however the field is inhomogeneous.

Experimentally, we find that the Rabi power is pressure dependent as shown in Fig. 4.4(a). The decrease of the MW power is possibly due to the MW strip deformation under the pressure, and the change of the total circuit impedance. After all, the power delivered to the antenna is dominated by the reflectance coefficient of the combination of leads and antenna. Although most of the power is reflected, in practice the transferred MW power is sufficient to manipulate NV spin to perform AC sensing protocols at different pressures.

4.2 NV properties under pressure

In order to facilitate quantum sensing with an NV ensemble in a diamond anvil cell, one needs to understand how NV spins respond to pressure. In this section, we will explain some basic properties of NV such as energy levels and coherence time as pressure increases.

4.2.1 CW ESR under pressure

Fig. 4.5 presents a series of NV spectra as a function of pressure. Under zero pressure, we noticed the higher frequency lines of the spectra (blue) are not completely overlapping. This is due to a slight misalignment between external field $\mathbf{H_0}$ and diamond chip [111] direction. During pressurization, the zero field splitting D increases and the lines gets broader as pressure increases.

Using a linear relation between the zero field splitting D and the pressure P, one can estimate the pressure at each taken measurements to be:

$$P_{est} = \frac{D - D_0}{A}, \tag{4.1}$$

where we choose $D(0) = 2866$ MHz and $A = 11.72$ MHz/GPa [77], and D can be

extracted by fitting the NV ESR spectra. The line broadening can be caused by various reasons. One of the most important reasons is the pressure inhomogeneity, which will be discussed later.

We also noticed that the peak intensity ratio between low frequency and high frequency peaks varies under pressure. Even though all the measurements are taken with the same light polarization direction (see Section 3.2), the resonance intensity is dominated by the MW power reflectance. It is very likely that the reflectance coefficient changes dramatically as the antenna deforms during the pressurization, which is the same reason for Rabi power pressure dependence.

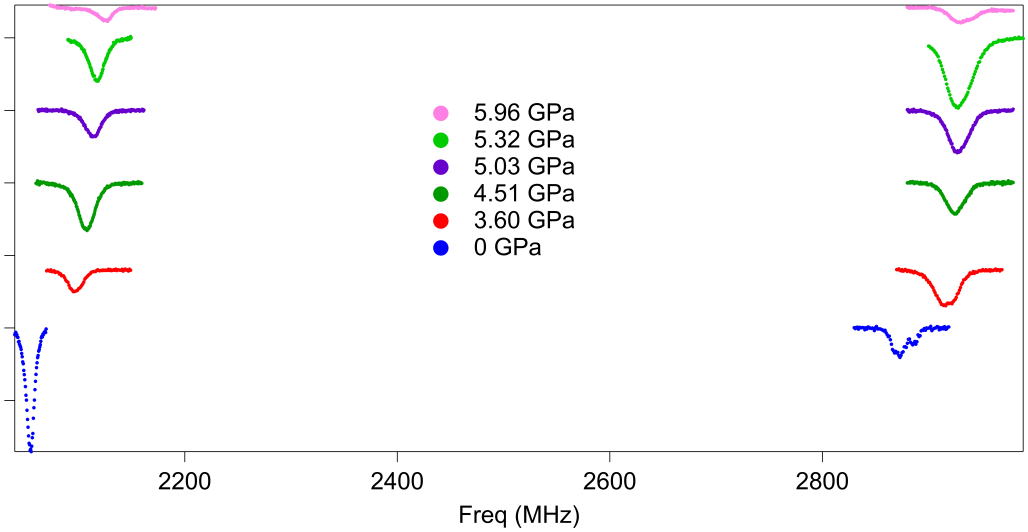

Figure 4.5: Pulsed ESR spectra of a diamond with NV^- centers under different pressure when $H_0 = 29$mT. The resonance condition depends on the zero field splitting D and four possible orientations of the NV^- axis in the diamond lattice. The measurement only captures lower half of the whole spectra (4 peaks out of 8 in total). The pressure is calibrated from the spectra by subtracting D(P) using curve fitting.

4.2.2 Ramsey interferometry

Under pressure, the NV^- spin dephases much faster than under ambient condition, as shown in Fig. 4.6. The Ramsey signal contains information about hyperfine coupling

to nearby ^{14}N nuclear spin (if the MW excitation is wide enough) and its amplitude decays exponentially with characteristic time $1/T_2^*$. However as pressure increases, T_2^* decreases by a factor 30 – from 3 μs to 100 ns.

So far as we know from Fig. 4.5, the $|0\rangle$ to $|-1\rangle$ is still a single transition under pressure. However, if both hydrostatic and shear pressure are generating local inhomogeneity, that might introduce extra term into dephasing process, which makes T_2^* faster. In next section we shall see that by utilizing dynamical decoupling sequences such as spin echo, the local strain inhomogeneity can be refocused, which preserves the relaxation time T_2 to be about same as that under ambient condition.

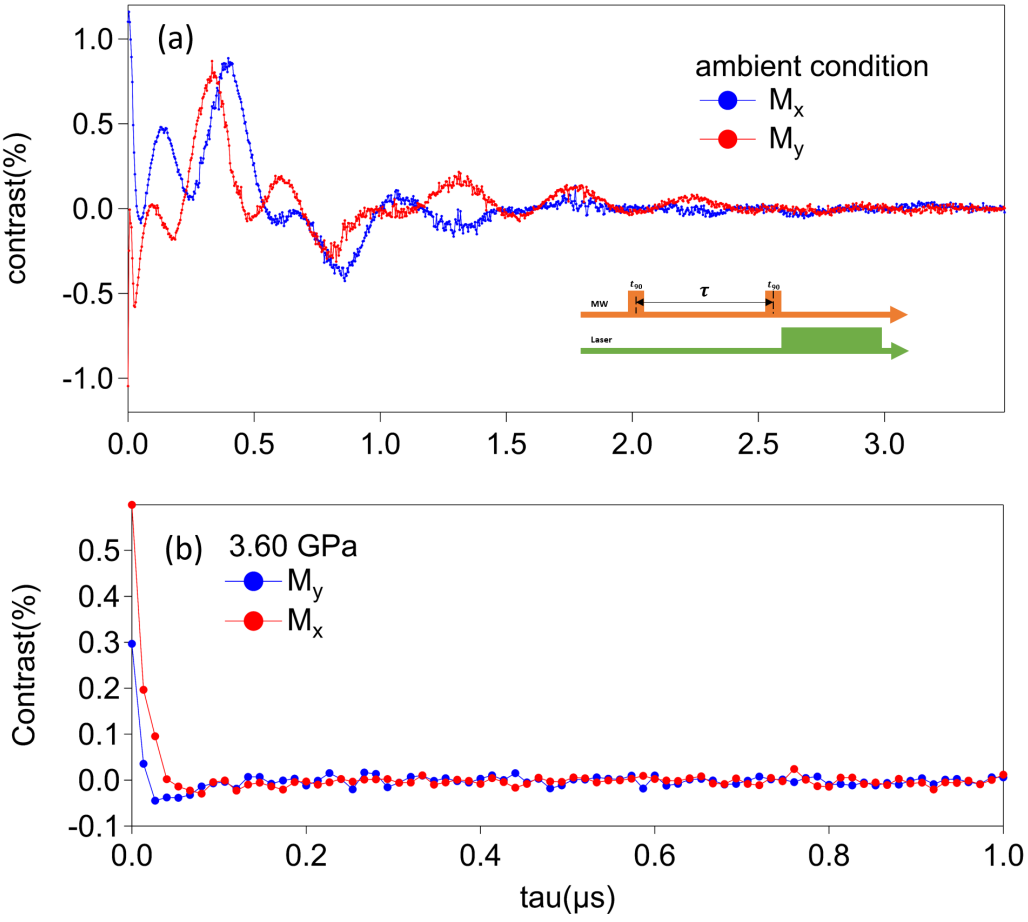

Figure 4.6: Ramsey interference measured by $90_x - \tau - 90_{\pm x}$ and the $90_x - \tau - 90_{\pm y}$ sequences under (a) ambient condition and (b) 3.60 GPa pressure.

4.2.3 Spin echo

4.2.3.1 Coherence time T_2

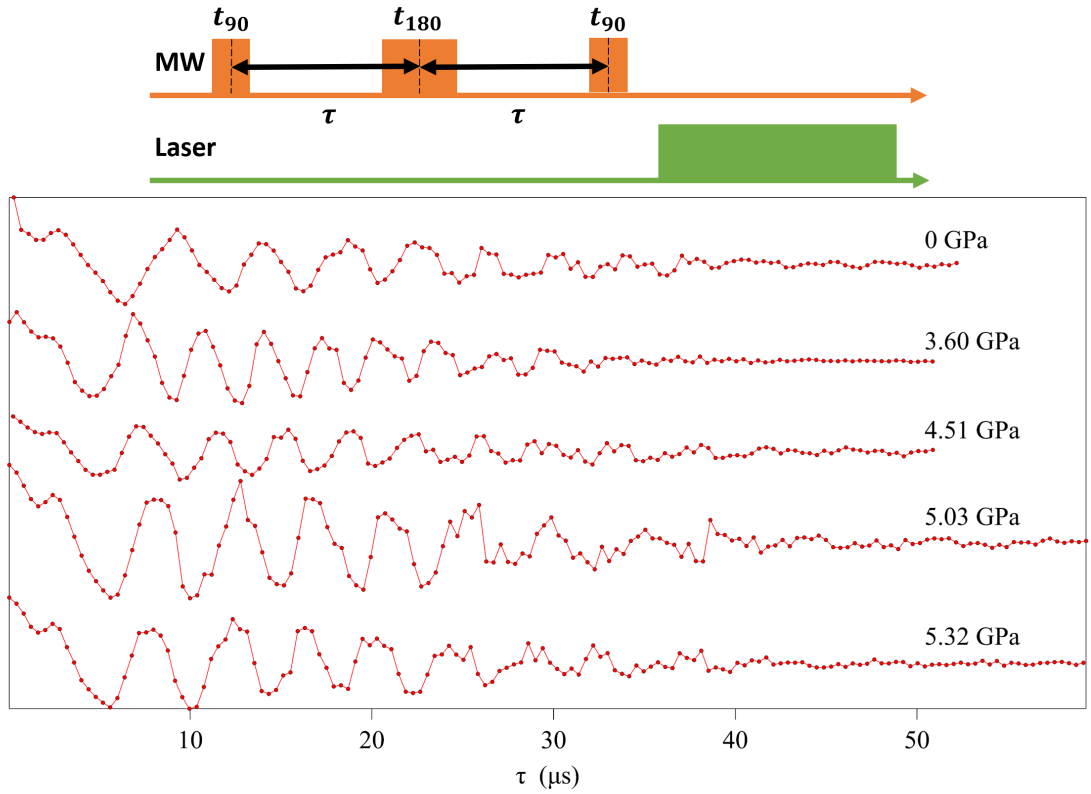

Figure 4.7: Spin echo coherence versus τ under various pressure. The contrast is measured by $90_x - \tau - 180_x - \tau - 90_{\pm x}$. The oscillations are due to the AC field created by nearby ^{13}C nuclear spins.

In contrast to Ramsey interference, the coherence time T_2 measured by a spin echo sequence stays the same under pressure. Fig. 4.7 shows the spin echo contrast versus the pulse spacing τ as pressure increases. T_2 is approximately 40 μs at all pressure levels. The oscillations in the echo signal occur at $f \sim 0.3$ MHz, which is close to the Larmor frequency of the ^{13}C: $f_{^{13}C} = \gamma_{^{13}C} H_0 = 0.31$ MHz.

The reason that the coherence time T_2 is unaffected by strain inhomogeneity can be understood by considering the static line broadening. As mentioned in Eq. 1.49,

the spin Hamiltonian under hydrostatic pressure can be written as:

$$H_{NV} = (D + \delta(x))S_z^2 + \gamma H_0 S_z + \sigma(x)(S_x^2 - S_y^2), \tag{4.2}$$

where $\delta(x)$ and $\sigma(x)$ are parameters that are directly proportional to hydrostatic and shear strain, respectively. These quantities are usually spatial dependent [51]. If we assume $D \gg \delta, \sigma$, one can apply second order perturbation theory to get the energy eigenvalues:

$$\mathrm{E}_{+1}^{'} = D + \gamma H_0 + \delta + \frac{\sigma^2}{2\gamma H_0} \tag{4.3}$$

$$\mathrm{E}_{0}^{'} = 0 \tag{4.4}$$

$$\mathrm{E}_{-1}^{'} = D - \gamma H_0 + \delta - \frac{\sigma^2}{2\gamma H_0} \tag{4.5}$$

Now if we just consider the $|0\rangle$, $|-1\rangle$ two level subsystem, we find that phase term $e^{-iE_{-1}^{'}t}$ can be cancelled by the spin echo approaches despite there is a spatial distribution (similar to spin echo to cancel magnetic field inhomogeneity in conventional NMR). Meanwhile for Ramsey interference, the spatial inhomogeneity in $\delta(x)$ and $\sigma(x)$ will exaggerate the dephasing process, which reduces T_2^* as strain increases (similar to free induction decay in conventional NMR).

4.2.3.2 FFTSUM

Different from spin echo T_2 measurement, one can fix first $\tau = \tau_0$, then sweep τ_1 as illstrated in Fig. 4.8 – eventually the signal will form an echo when $\tau_1 = \tau_0$. The spectra can be measured at various frequencies and their Fourier transform can be summed together. This so called FFTSUM approach is often utilized to obtain spectra in conventional NMR (see Fig. 6.5). Fig. 4.8 displays FFTSUM spectra versus pressure. The spectra clearly broaden with pressure, and the hyperfine coupling peaks have been washed out under pressure. We find that the linewidths increase by a factor

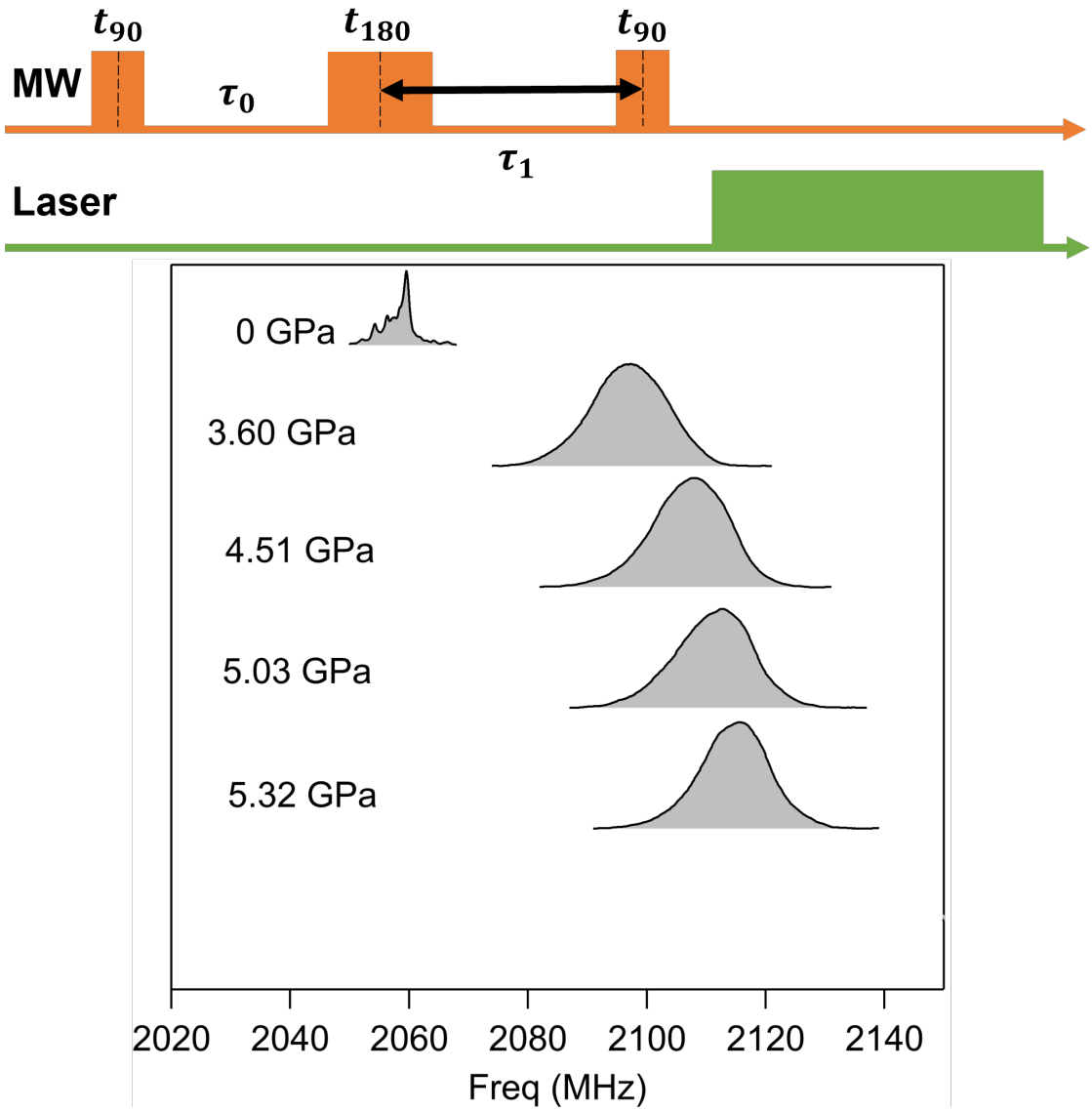

Figure 4.8: Spectra of the $|0\rangle \leftrightarrow |-1\rangle$ transition of the NV ensemble as a function of pressure, measured by spin echo sequences. Each spectra is obtained by gluing several τ_1 sweeping spectra together. τ_0 here is choose to be around 8 μs.

of eight over this range, which is as expected since the width is still dominated by T_2^*. The frequency shift is comparable with continuous-wave ESR results.

4.3 AC quantum sensing under pressure

In the previous section we have shown that despite the non-hydrostatic pressure environment, the signal can still be refocused by dynamical decoupling sequences, making AC quantum sensing possible. Here we display two quantum sensing protocols to detect AC magnetic signals. These methods can detect AC fields generated by nearby nuclear spins and small test AC signals.

4.3.1 XY8-N pulse spacing sweep

The most straightforward approach to detect an AC field is to sweep the pulse spacing, τ, and search for changes in signal contrast ΔI. As shown in Eq. 3.20, $\Delta I \sim 1 - (\frac{M\gamma h_{ac}}{4\pi f_{ac}})^2$ if $\tau = (2f_{ac})^{-1}$ ($2\pi f_{ac} \gg \gamma h_{ac}$), where M is the number of π pulses and the AC signal is $h_{ac}\sin(2\pi f_{ac}t + \phi)$. If τ is matched with f_{ac}, the contrast will have a observable dip whose depth is proportional to B_{ac} (see Fig. 3.17(b)).

Figure 4.9 shows XY8-N pulse sweeping spectra without any external driving AC field at ambient pressure, 3.6 GPa and 5.0 GPa respectively. The contrast decays exponentially as τ increases due to the dephasing effect. There is a dip in the contrast at $\sim$ 0.3 MHz, which corresponds to the Larmor frequency of ^{13}C in the applied H_0 field. The 1% abundant ^{13}C nuclear spins in the diamond lattice precess at this frequency and create AC fields at the NV site that are not refocused by the dynamical decoupling. The dips around 0.6 and 1.2 MHz are corresponds to $2f_{ac}$ and $4f_{ac}$, which can also be picked up by XY8-N sequences if the MW pulses are imperfect [47]. The peaks at 1.2 MHz may alaso arise from ^{1}H nuclei since $\gamma_{^1H} \sim 4\gamma_{^{13}C}$. Based on the sensitivity of our system and other AC sensing methods we tried, it is almost certain that the three dips are all contributed by ^{13}C nuclear spin.

It is also obvious that the dip depth drops as pressure increase, which is possibly due to inhomogeneous pressure distribution, leading to a reduction on the NV

sensitivity.

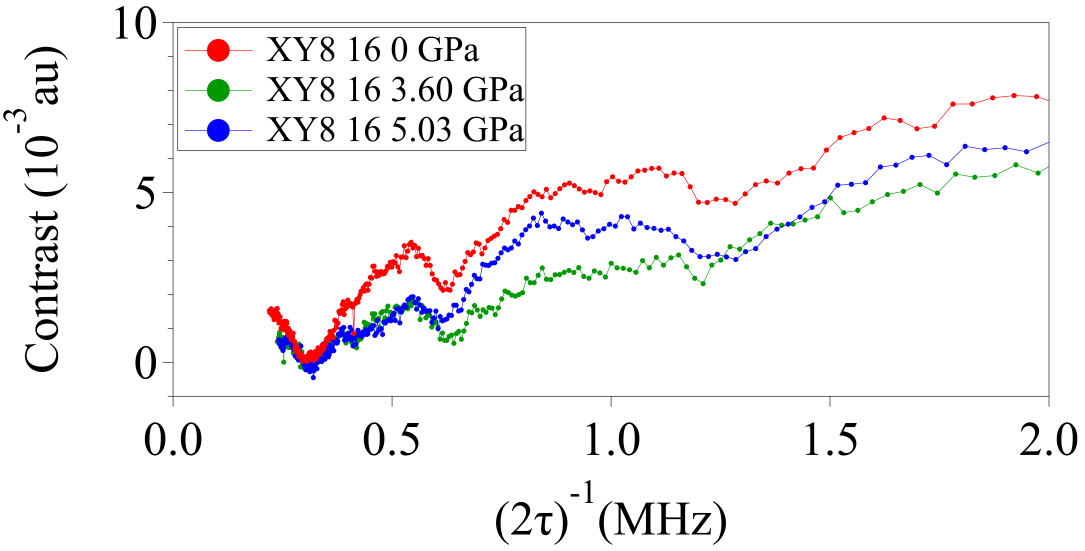

Figure 4.9: Optical contrast versus frequency, $(2\tau)^{-1}$, where τ is the pulse spacing of an XY8-16 sequence, measured at various pressures. The dips around 0.3, 0.6 and 1.2 MHz arise from precessing ^{13}C spins in the diamond lattice.

4.3.2 Synchronized readout

Instead of averaging the signal over randomly-distributed initial phases at the beginning of each repeat of the dynamical decoupling sequence, it is possible to collect each fluorescence measurement and perform a Fourier transform. After each NV fluorescence measurement, the NV is re-initialized into the ground state without affecting the AC source. As a result, the phase of $\mathbf{B}_{ac}(t)$ will evolve in a coherent fashion for each measurement. The phase of detecting AC field at m^{th} acquisition should be:

$$\phi_m = 2m\pi(f_{ac} - (2\tau)^{-1})T_{meas} + 2n\pi + \phi_0 \tag{4.6}$$

according to Eq. 3.24, where $T_{meas} = 2n\tau$ is the total measurement duration for each cycle, and $\delta f \equiv f_{ac} - (2\tau)^{-1}$ is the frequency offset between target signal and

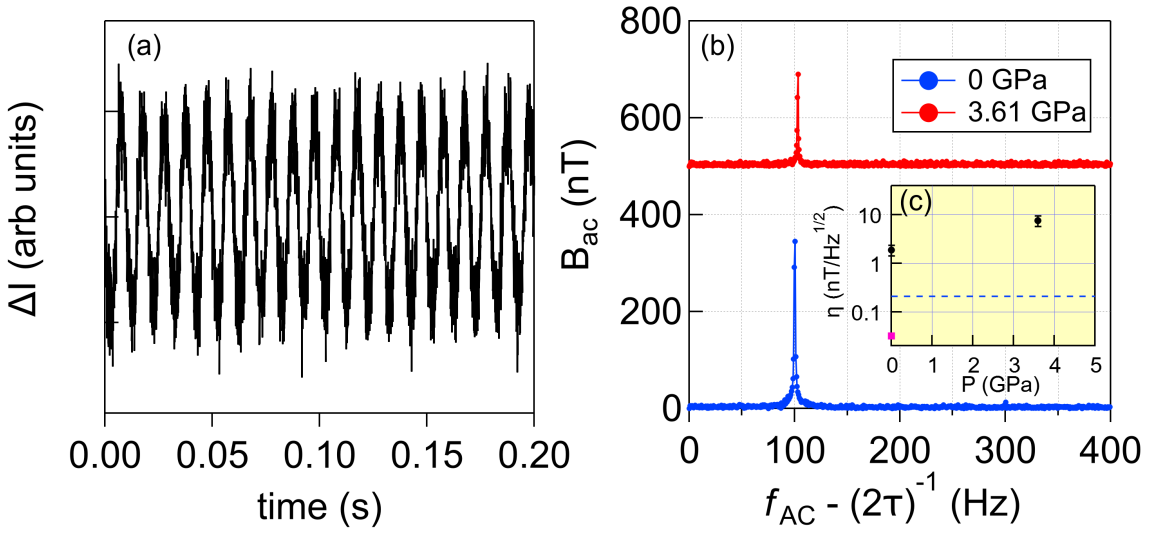

Figure 4.10: (a) Optical contrast, ΔI measured for NVs in the DAC with a test signal at frequency $f_{ac} = 1.2001$ MHz, where $\tau = 416.667$ ns (corresponding to a detection frequency at 1.2 MHz), for a XY8-16 sequence of equally-spaced measurements at with $T_{meas} = 45$ μs, as described in the text. (b) Fourier transform of ΔI at ambient pressure. The spectra exhibits a single large peak at 100 Hz, and the vertical axis has been scaled to match the known applied field magnitude. The 3.61 GPa data has been offset vertically by 500 nT for clarity. (c) Sensitivity, η (•), versus pressure. The dashed blue line corresponds to the necessary sensitivity to achieve unity signal to noise ratio after 1 minute, and the pink square (■) at 0 GPa corresponds to the sensitivity reported in [33].

detection signal. For a $90_x - 90_y$ sequence in the limit of small B_{ac}, the fluorescence contrast will vary as (Eq. 3.26):

$$\Delta I(T) \sim \left(\frac{2N\gamma B_{ac}}{2\pi f_{ac}}\right) \cos(2\pi\delta f T + \phi_0), \tag{4.7}$$

where $T = mT_{meas}$. In effect, the AC field is demodulated by the dynamical decoupling sequence, and imprinted on ΔI. A Fourier transform of $\Delta I(T)$ thus provides a spectrum of $B_{ac}(t)$ relative to the detection frequency $(2\tau)^{-1}$.The frequency resolution is determined by the number of points m, T_{meas}, the stability of the field $\mathbf{H}_0$, and the stability of the microwave pulse timing. The resolution can be as low as a mHz, which is sufficient to resolve many chemical shifts even at low applied fields [70,

33]. This technique requires coherently averaging many repeated measurements, but sufficient signal-to-noise ratio can be obtained within a few hours.

In practice, the nuclear spins we want to measure – protons in Daphne oil as an example – are dominated by statistical polarization under our experimental conditions [89], which leads to rather weak (in the range of pT) AC field magnitude B_{ac} and random phases ϕ_0. The same is true for the ^{13}C spins – the phases are random even though with stronger magnitude. Therefore, we tried to generate a uniform, single-phased test AC signal by a copper coil outside of DAC, in order to demonstrate accessibility of this sensing method under pressure. The results are illustrated in Fig. 4.10.

4.4 Discussion

4.4.1 Sensing sensitivity

The data shown in Fig. 4.10 was acquired for a large applied test AC field for a single acquisition sequence without signal averaging with a total measurement time of approximately 1.5 s, corresponding to a sensitivity, $\eta = 1.9$ nT/Hz$^{1/2}$ at ambient pressure. The test field magnitude is calibrated using the same method described in Section .3.7.3. At 3.6 GPa, we find the sensitivity decreases to $\eta = 7.6$ nT/Hz$^{1/2}$. Here we define sensitivity as the minimum detectable signal per unit time. Ideally η should be as low as possible to achieve a high signal to noise ratio. Our values are not as low as previous reports, which reach down to 32 pT/Hz$^{1/2}$ [33]. One of the primary reasons for the difference in the DAC is the wide distribution of Rabi frequencies, which means that not all of the NVs in the ensemble experience the same H_1 field. The pulse width for the dynamical decoupling 180° pulses, given by $\pi/(\gamma H_1)$, will differ for each of these NVs. As a result, the accumulated phase is not as high as it would be for a uniform H_1. To illustrate this point, Fig. 4.11 shows how the

signal intensity varies as a function of the pulse width time. Numerical simulations of the Bloch equations under these conditions indicate that the sensitivity is reduced by $\approx 10\%$ if the dynamical decoupling pulses are either 10% shorter or longer than ideal. As shown in Fig. 4.4, the H_1 field for the straight antenna is inhomogeneous over the sample volume, such that the width of the distribution is approximately 40% of the average. Although this antenna is able to provide large H_1 fields within the sample space, the field inhomogeneity reduces the synchronized readout sensitivity.

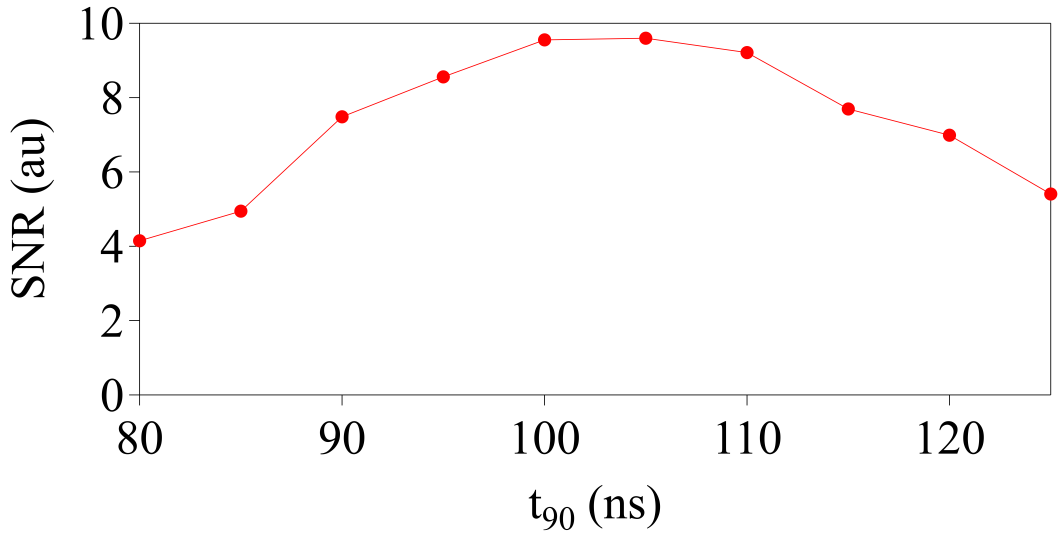

Figure 4.11: Signal intensity (arbitrary units) for a synchronized readout measurement of an AC signal (as in Fig. 4.10) versus the width of a 90° pulse. The dynamical decoupling pulses (180°) are twice as long as the time t_{90} given on the horizontal axis.

Another limiting factor for the sensitivity is the large ratio of the 180° pulse width, t_{180}, to the pulse spacing, τ. The data in Fig. 4.10 utilized $t_{180}/\tau \approx 0.43$, which is far from the idealized case of the infinitely-narrow pulses. Numerical simulations indicate that the sensitivity will be suppressed when the ratio $t_{180}/\tau \gtrsim 0.2$. This provides an effective upper limit on $\omega_{ac}^{max} \approx 0.2\Omega$ for a given value of the Rabi frequency, Ω.

Under pressure we find that η increases by a factor of four, as shown in Fig. 4.10(c). There are two possible reasons for this change. Under pressure the NV spectrum is broadened due to the pressure gradients. If the spectrum is sufficiently

broad, the dynamical decoupling pulses will not fully refocus the NV magnetization, similar to the effect of a non-uniform H_1 field as discussed above. Moreover, the antenna deforms under pressure, and as a result the impedance changes and affects the magnitude of the H_1 field. Consequently both Ω and ΔI can be reduced, affecting the sensitivity.

4.4.2 Pressure inhomogeneity

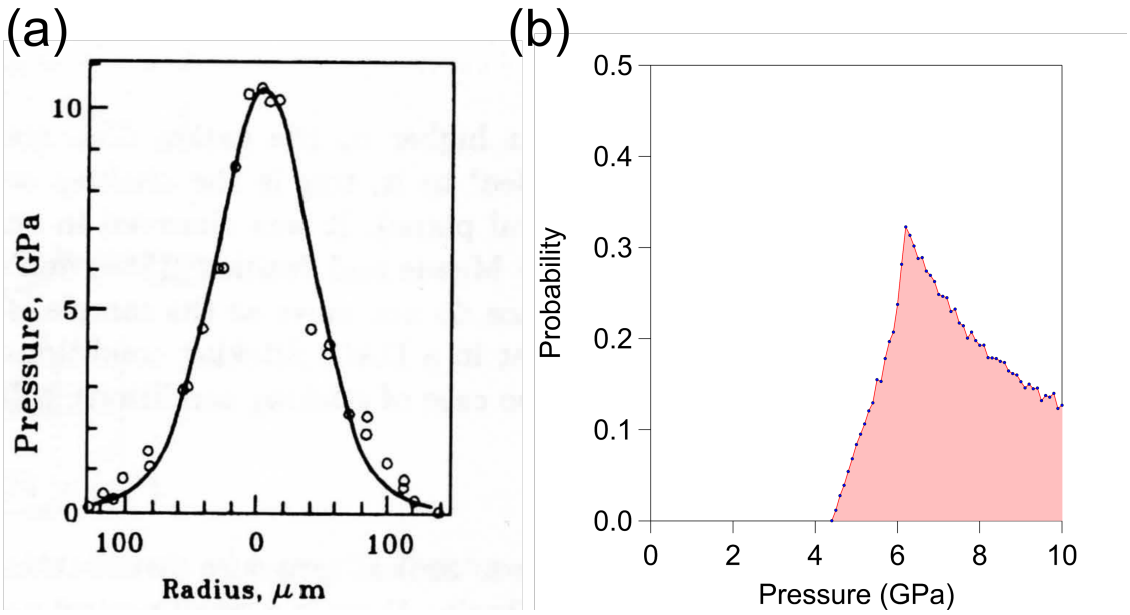

Figure 4.12: (a) Experimental data of pressure spatial distribution in the DAC. Flat plate, natural diamond ($R = 100\mu$m); gasket, capacitor paper of thickness 12 μm; applied load, 150 N[28]; (b) Pressure probability distribution of a 80 μm $\times$ 80 μm sample in the DAC center under the pressure spatial distribution in (a). The histogram is obtained using the Monte Carlo method.

As shown in Fig. 4.12(a), the pressure inside the sample chamber of a DAC reaches its maximum at the center ($r = 0$), and drops to zero when it is away from culet region ($r \geq r_{culet}$). Using a Monte Carlo simulation, one can obtain the pressure distribution within a square sample of 80×80 μm^2, as shown Fig. 4.12(b) (assuming pressure distribution only occurs in the xy plane). We can then approximate the

pressure distribution with a Lorentzian form:

$$\rho(P) \sim \frac{\sigma_P/2\pi}{(P-P_0)^2+\sigma_P^2}. \tag{4.8}$$

where P_0 is the mean value and σ_P is the standard deviation of the original distribution.

Under ambient condition, we assume the energy spectrum to be:

$$S_0(E) = \frac{\sigma_0}{(E-E_\pm)^2+\sigma_0^2}, \tag{4.9}$$

where $E_\pm = D_0 \pm \gamma B$ and $\sigma_0 \sim \frac{1}{T_2^*}$ depicts the NV^- spin decoherence.

Under few GPa pressure, if one only considers the effect of hydrostatic pressure (Section 1.4.4), it is reasonable to assume $M_z = AP$[77, 25, 21]. Hence the energy spectrum should be:

$$S_P(E) = \int S_0(E-AP)\rho(P)dP \tag{4.10}$$

$$= \int S_0(E-E^{'})\rho(E^{'})dE^{'} \tag{4.11}$$

where $E^{'} = M_z = AP$. The new spectrum becomes a convolution between the original one and the pressure distribution. Since they are both Lorentzian, it can be shown that the result is still a Lorentzian and it has form:

$$S_P(E) = \frac{\sigma_P^{'}}{(E-(E_\pm+AP_0))^2+{\sigma_P^{'}}^2}, \tag{4.12}$$

where $\sigma_P^{'} = A\sigma_P + \sigma_0$.

One major effect of pressure is the common shift – the NV^- energy levels should all shift by $\omega_{CM} = AP_0$; another one is the line broadening – the new line width under

pressure should increase by $A\sigma_P$. These phenomena are evident in high pressure ODMR. Fig. 4.13 shows extracted P_0 and σ_P from Fig. 4.8. It is as expected that σ_P is about 0.6 GPa, where is about the same as Monte Carlo simulation on a 80 μm $\times$ 80 μm sample in Fig. 4.12(b).

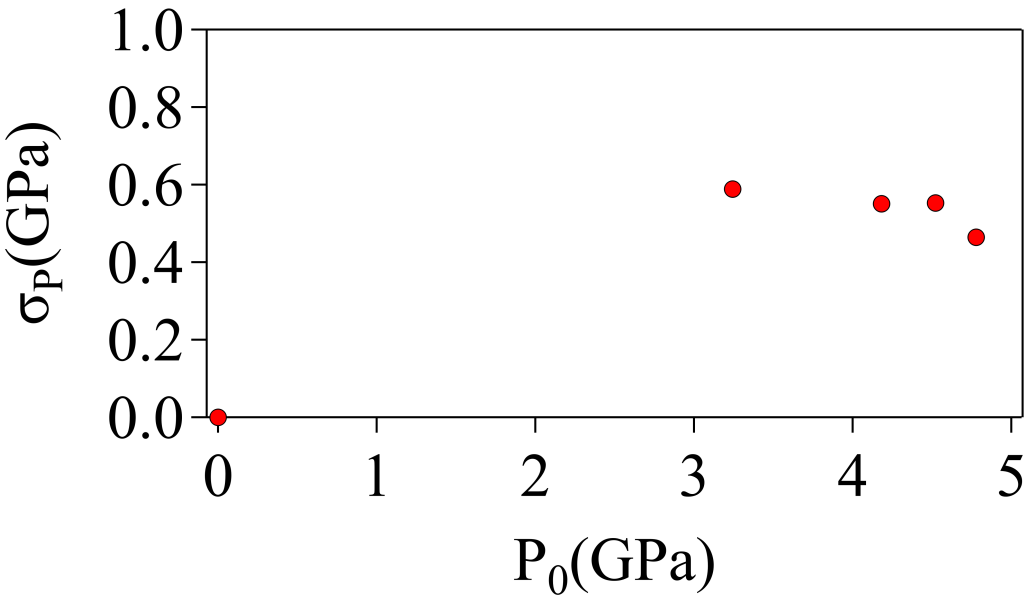

Figure 4.13: Pressure distribution characterization. Each point indicates its pressure condition inside the DAC. P_0 and σ_P are extracted by fitting FFTSUM spectra 4.8 with Lorentzian. $A = 11.72$ MHz/GPa [77].

4.4.3 Future improvements

There are several possible routes to improve the sensitivity of AC-ODMR in the DAC. The inhomogeneity of the microwave fields from the antenna leads to an increase in η. An antenna design that provides a more homogeneous and stable H_1 field and is less prone to distortions under pressure is vital. In the future other antenna designs may be considered, for example a circular loop within the sample space, to improve the homogeneity and reduce screening effects by the gasket.

Utilizing diamonds with lower NV concentrations and isotopically pure ^{12}C would significantly enhance T_2 and also improve the sensitivity. It is also possible to im-

prove the sensitivity by utilizing dynamic nuclear polarization. This number can be enhanced significantly by utilizing the presence of free radicals and taking advantage of the Overhauser effect to transfer polarization to the nuclear spins in a liquid. Bucher et al. used the TEMPOL molecule dissolved into liquid solutions to enhance the sensitivity by more than a factor of 200 [15]. The unpaired electrons on the TEMPOL molecule have an enhanced spin polarization that can be transferred to hyperpolarize the nuclear spins beyond their thermal polarization described in Section .1.1. This process can enhance the signal-to-noise ratio by several orders of magnitude, but requires pulsing the system at the Larmor frequency of the TEMPOL electron spins for several ms prior to detection of the nuclear spins with NV magnetometry.

The sensitivity may also be improved by utilizing double quantum coherence under pressure [50, 51]. The AC-ODMR experiments described here are based on single quantum coherence in which the NV is prepared in the state $|0\rangle + |\pm 1\rangle$. The resonance frequency of the double quantum coherent state $|-1\rangle + |+1\rangle$ is independent of D. This property could be important because pressure inhomogeneities strongly affect D, giving rise to spectral broadening that impacts the sensitivity of the AC detection. More details about double quantum will be discussed in the next chapter.

Chapter 5

Double quantum resonance metrology

This chapter describes a novel method to manipulate the NV^-spins – instead of using $|S_z = 0\rangle$ and $|S_z = -1\rangle(|S_z = +1\rangle)$, the qubit two level system is generated by $|S_z = -1\rangle$ and $|S_z = +1\rangle$. This so called double quantum (DQ) method offers advantages over traditional single quantum (SQ) method in various aspects. The experimental setup will be introduced and preliminary results such as Rabi oscillations and Ramsey spectroscopy will be discussed.

5.1 Motivations

In section 4.4.2, we discussed the potential hazard of the pressure inhomogeneity. The line gets so broad that the hyperfine coupling structure to ^{14}N nuclear spin is washed out. It may as well undermine the AC sensing sensitivity as pressure increases. One possible solution to get rid of hydrostatic inhomogeneity is the DQ spectroscopy. For transition between $|S_z = -1\rangle$ and $|S_z = +1\rangle$, the energy spectra becomes:

$$S_{DQ}(E) = \frac{\sigma_0}{(E - 2\gamma B)^2 + \sigma_0^2}, \tag{5.1}$$

which is pressure independent. Under pressure though there is a distribution around the sample, it has no effect on $S_{\pm}(E)$ and there should be no common shift and line broadening. Therefore by utilizing DQ methods the hyperfine interaction to ^{14}N and AC sensitivity under pressure should be improved comparing to SQ methods.

Unlike SQ transitions of NV, which can be achieved using MW fields which couples to spin ladder operators $\hat{S}_+$, the DQ transition of NV is rather challenging to be achieved directly. One accessible approach is creating a superposition of $|\pm 1\rangle$ using SQ transition, letting the system evolve, eventually measuring reflecting the states back to $|0\rangle$ [50]. Although transition DQ might directly couples to strain and electric field, the coupling to strain is in a complex form whereas coupling to electric field is much weaker than magnetic field [48, 26].

Another advantage of DQ is the AC sensing amplitude enhancement. Instead of γB response in SQ, the magnetic field gives rise to a differential shift ω_{DF}, which is $2\gamma B$, resulting in $4\times$ sensitivity increase when measuring small AC field (due to the statistical polarization, the AC field amplitude from surrounding nuclear spins is proportional to B_{rms}^2). A proton NMR measurement using single NV$^-$ center was shown in [50].

5.2 Excitation and control of the DQ resonance

Consider an NV spin in the presence of a time independent field with two frequency components:

$$H_{DQ} = DS_z^2 + \gamma B \cdot S + \gamma(B_1 \cos(\omega_1 t + \phi_1) + B_2 \cos(\omega_2 t + \phi_2))S_x, \tag{5.2}$$

where ω_i and ϕ_is are the frequency and phase for ± 1 transitions. In the matrix form it is:

$$H_{DQ} = \begin{pmatrix} D+\gamma B & \gamma h_{MW}/\sqrt{2} & 0 \\ \gamma h_{MW}/\sqrt{2} & 0 & \gamma h_{MW}/\sqrt{2} \\ 0 & \gamma h_{MW}/\sqrt{2} & D-\gamma B \end{pmatrix}, \tag{5.3}$$

where $h_{MW} = B_1 \cos(\omega_1 t + \phi_1) + B_2 \cos(\omega_2 t + \phi_2)$. Analogous to $S = \frac{1}{2}$ system, we apply unitary transformation

$$U = \begin{pmatrix} e^{-i\omega_1 t} & 0 & 0 \\ 0 & 0 & 0 \\ 0 & 0 & e^{i\omega_2 t} \end{pmatrix}, \tag{5.4}$$

to the Hamiltonian [50]. The transformed Hamiltonian $\tilde{H}_{DQ} = U^\dagger H_{DQ} U + i\frac{\partial U^\dagger}{\partial t} U$ becomes:

$$\tilde{H}_{DQ} = \begin{pmatrix} D+\gamma B-\omega_1 & e^{i\omega_1 t}\gamma h_{MW}/\sqrt{2} & 0 \\ e^{-i\omega_1 t}\gamma h_{MW}/\sqrt{2} & 0 & e^{i\omega_2 t}\gamma h_{MW}/\sqrt{2} \\ 0 & e^{-i\omega_2 t}\gamma h_{MW}/\sqrt{2} & D-\gamma B+\omega_2 \end{pmatrix}. \tag{5.5}$$

Using rotating wave approximation, the off-diagonal term, taking $e^{i\omega_1 t}\gamma h_{MW}/\sqrt{2}$ as an example, can be simplified to be:

$$\begin{aligned} e^{i\omega_1 t}\gamma h_{MW}/\sqrt{2} &= \frac{\gamma B_1}{2\sqrt{2}} e^{i\omega_1 t}(e^{-i\omega_1 t}e^{-i\phi_1} + e^{i\omega_1 t}e^{i\phi_1}) \\ &\quad + \frac{\gamma B_2}{2\sqrt{2}} e^{i\omega_1 t}(e^{-i\omega_2 t}e^{-i\phi_2} + e^{i\omega_2 t}e^{i\phi_2}) \\ &\sim \gamma B_1 e^{-i\phi_1}/2\sqrt{2} \end{aligned} \tag{5.6}$$

$(\omega_1, \omega_2, |\omega_1 - \omega_2| \gg 1)$.

Eventually, the final time-independent Hamiltonian in rotating frame $\tilde{H}_{DQ}$ is:

$$\tilde{H}_{DQ} = \begin{pmatrix} D+\gamma B-\omega_1 & \gamma B_1 e^{-i\phi_1}/2\sqrt{2} & 0 \\ \gamma B_1 e^{i\phi_1}/2\sqrt{2} & 0 & \gamma B_2 e^{-i\phi_2}/2\sqrt{2} \\ 0 & \gamma B_2 e^{i\phi_2}/2\sqrt{2} & D-\gamma B+\omega_2 \end{pmatrix}. \tag{5.7}$$

By controlling B_i, ω_i and ϕ_is' value, the dynamical decoupling sequences can be constructed and NV^-'s final state can be calculated analytically:

$$|\Psi\rangle = e^{-i\tilde{H}_{DQ}(\mathbf{B}_n,\omega_n,\phi_n)tn}...e^{-i\tilde{H}_{DQ}(\mathbf{B}_2,\omega_2,\phi_2)t2}e^{-i\tilde{H}_{DQ}(\mathbf{B}_1,\omega_1,\phi_1)t1}|\Psi_0\rangle, \tag{5.8}$$

If we assume $B_1 = B_2 = B$ and two MW pulses is turned on and off simultaneously (two tone pulse), then we can define t_{180} as the time needed to pump the $|0\rangle$ initial state to the superposition state $\frac{1}{\sqrt{2}}(|-1\rangle + e^{i\theta}|+1\rangle)$ on resonance:

$$t_{180} = \frac{\pi}{\gamma B}, \tag{5.9}$$

which is $\sqrt{2}$ times quicker than SQ t_{180} with the same MW amplitude.

5.3 Experimental method

In principle, the only difference between SQ and DQ measurements is the MW control. Instead of exciting from $|0\rangle$ to $|+1\rangle$ or $|-1\rangle$, electrons are pumping to both energy levels. However, in real experiments, it usually contains both SQ and DQ signals at the same time. In order to maintain DQ signal in the meantime to get rid of SQ signals, it is necessary to implement phase cycling to cancel unwanted components meanwhile to keep the DQ signals.

5.3.1 MW generation

There are two possible ways to generate DQ states: generating two different frequency pulses simultaneously or generate them one after the other. Here we only discuss the first method.

For AWG MW generation, in order to have more points in one period to distinguish different phases, the higher harmonics generation is used. For generating the two tone pulse, we use the same method – a lower frequency two tone pulse is generated, and its higher harmonics component is isolated and amplified. The other harmonics we are not interested in can be filtered out.

In order to keep the same pulse duration (t_{90}) for two transitions, one can run Rabi oscillation experiments separately on each transitions. Usually the same MW input power for each transition does not result in the same t_{90} (due to circuit different impedance @ ± 1 transitions). Hence the two frequency components generated by AWG usually have different amplitudes.

5.3.2 Phase cycling

In conventional solid state NMR, CYCLOPS cycling is often used to cancel out noise due to imperfection of the experiments [19]. We also used partial phase cycling in SQ NV^- spectroscopy for quadrature detection (see Section 3.5.1). For DQ measurements, however, the phase cycling is always required to extract the DQ component from SQ.

Table 5.1 displays possible single phase measurements and their expected FL signal. A preliminary version of phase cycling for DQ Ramsey is picking four phase combinations from the first eight rows in table 5.1 to form $\cos 2\omega\tau$ and picking four from the last eight rows to form $\sin 2\omega\tau$. It requires four phases for each quadrature channel since it needs to cancel the SQ and baseline offset in the same time. A detailed study will be discussed in Section 5.5.

Pulse 1 $\|-1\rangle$	Pulse 1 $\|+1\rangle$	Pulse 2 $\|-1\rangle$	Pulse 2 $\|+1\rangle$	FL $\|\langle 0\|\Psi\rangle\|^2$
x	x	x	x	$\cos^2\omega\tau$
x	x	-y	y	$\sin^2\omega\tau$
x	x	-x	-x	$\cos^2\omega\tau$
x	x	y	-y	$\sin^2\omega\tau$
x	x	y	y	$\cos^2\omega\tau$
x	x	x	-x	$\sin^2\omega\tau$
x	x	-y	-y	$\cos^2\omega\tau$
x	x	-x	x	$\sin^2\omega\tau$
y	x	x	x	$(\cos\omega\tau+\sin\omega\tau)^2/2$
y	x	-y	y	$(\cos\omega\tau-\sin\omega\tau)^2/2$
y	x	-x	-x	$(\cos\omega\tau+\sin\omega\tau)^2/2$
y	x	y	-y	$(\cos\omega\tau-\sin\omega\tau)^2/2$
y	x	y	y	$(\cos\omega\tau+\sin\omega\tau)^2/2$
y	x	x	-x	$(\cos\omega\tau-\sin\omega\tau)^2/2$
y	x	-y	-y	$(\cos\omega\tau+\sin\omega\tau)^2/2$
y	x	-x	x	$(\cos\omega\tau-\sin\omega\tau)^2/2$

Table 5.1: Expected DQ Ramsey FL output for some possible MW pulse phase configurations. Here $\omega=\omega_{rf1}-\omega_-=-(\omega_{rf2}-\omega_+)$ is the differential shift frequency ($\omega_\pm$: the resonance frequency of $|\pm\rangle$; $\omega_{rf1,2}$: the applied MW fields frequencies)

5.4 Double quantum Rabi

In order to implement DQ for quantum sensing, it is important to understand the behavior of simple MW sequences such as the Rabi sequence. Fig. 5.1(a) describes a special DQ Rabi sequence we used in pulsed ODMR experiments. Instead of applying two tone MW pulses, a pulse at frequency ω_1 is followed by one at frequency ω_2.

If ±1 MW pulses are independent events for FL, the final contrast can be written as: $\mathbf{FL}(t_{-1},t_{+1})=\mathbf{FL}(t_{-1})+\mathbf{FL}(t_{+1})$. As a result, one should expect FL having similar behavior versus t_{+1} with various t_{-1} – different t_{-1} will only lead to a different offset. However, based on the data in Fig. 5.1(b), we find that the FL oscillation amplitude $\mathrm{A}(t_{-1}=130\ ns)$ is less than half of $\mathrm{A}(t_{-1}=0\ ns)$, which contradicts to the ±1 MW independence. This can be explained by a common ground state $|S_z=0\rangle$ – when $t_{-1}=t_{180}$, the population at $|0\rangle$ is almost zero, which cannot afford a full amplitude Rabi as that when $t_{-1}=0$. Still, the FL does not become zero when

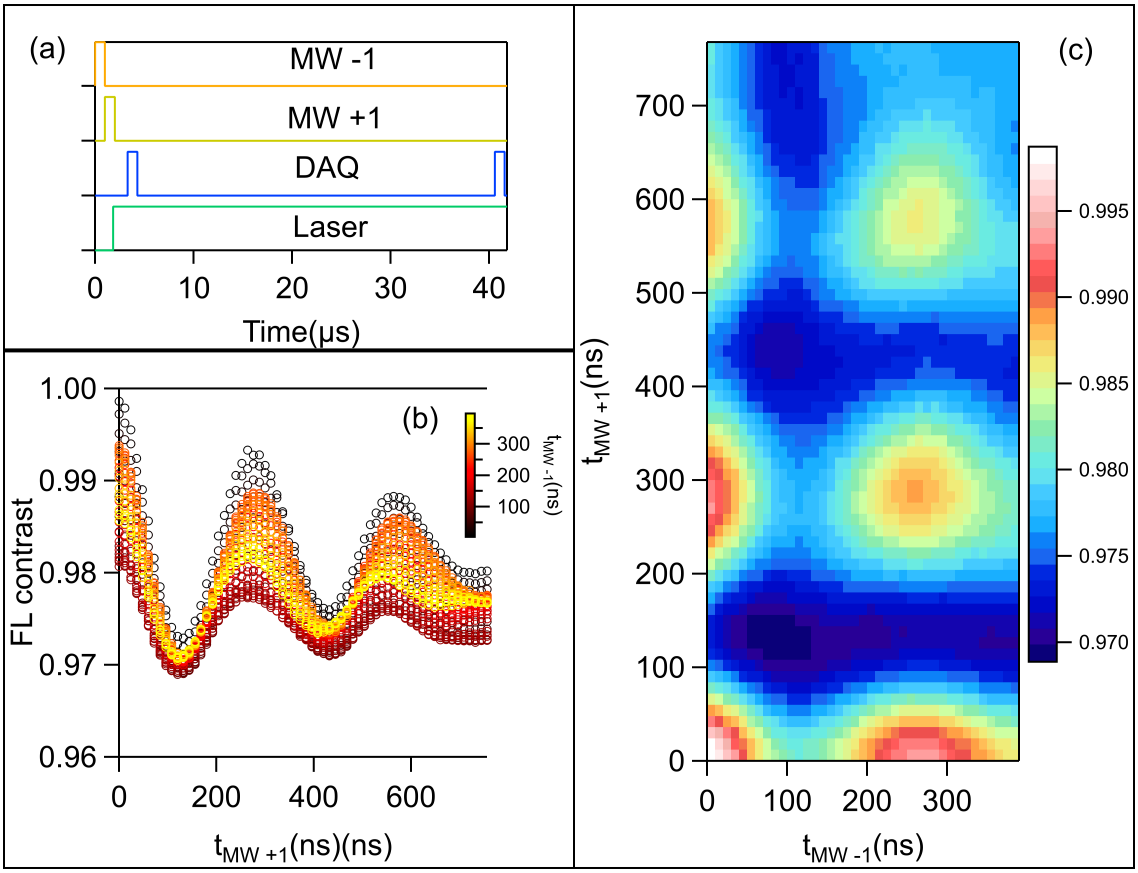

Figure 5.1: DQ Rabi experiment demonstration. The experiment is done under 60 G bias field ambient condition. (a) DQ Rabi pulse sequence. The two MW pulses for each transition are triggered sequentially with no overlapping in time. (b) FL contrast versus MW pulse duration of +1 transition. The color is indicating various -1 MW pulse duration prior to the +1 sweep. (c) FL color map versus MW duration for both ±1 transitions.

($t_{-1} = 130\ ns$), indicating the FL is not fully controlled by DQ: the ground states supports both SQ and DQ states.

To summarize, the DQ Rabi experiment results in a mixture between ±1 SQ and DQ components and SQ components is outweighing the DQ. The result might be due to the MW inhomogeneity and the mix state nature of NV^- ensemble. In that case, the phase cycling is necessary to cancel out SQ in order to study DQ. Unfortunately phase cycling is unsuitable for Rabi experiment – it does not offer phase information.

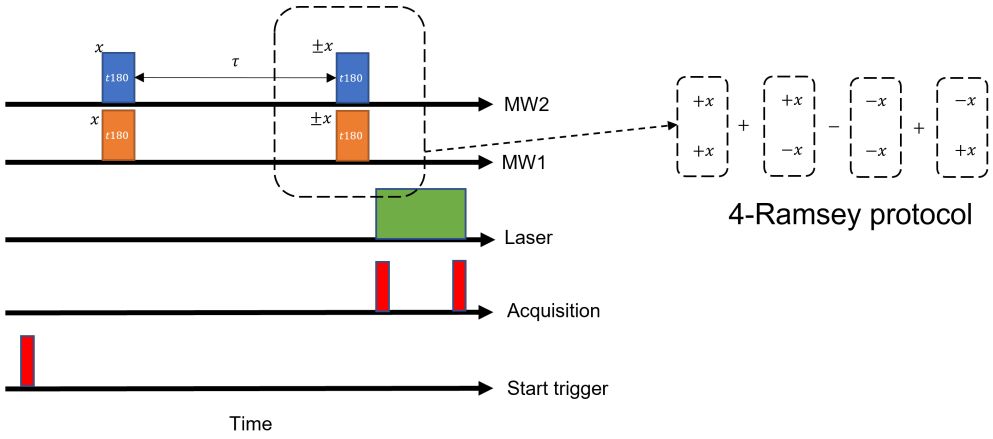

Figure 5.2: DQ Ramsey pulse sequence. Unlike SQ pulse sequence, the MW pulse contains two frequency component for two NV^- transitions. The inset is the phase cycling protocol to cancel out the SQ signals [36].

5.5 Double quantum Ramsey interferometry

5.5.1 Numerical analysis

The DQ Ramsey pulse sequence is displayed in Fig. 5.2. Since in ODMR experiments we measure FL $\propto |\langle 0|\Psi\rangle|^2$, we can studying FL numerically using the rotating frame as the waiting time τ and the frequency shift $\delta\omega$ change.

Unlike off-resonance SQ Ramsey (see Section .3.5.3), the frequency shift for DQ in general can be defined into two kinds: common shift $\omega_{CS} = \omega_{rf1} - \omega_- = \omega_{rf2} - \omega_+$, denoting to a shift that has same sign for both ± 1 transitions; differential shift $\omega_{DS} = \omega_{rf1} - \omega_- = -(\omega_{rf2} - \omega_+)$, denoting to a shift that has opposite sign for ± 1 transitions [36].

Fig. 5.3 shows necessity of phase cycling when applying off-resonance (differential shift) MW pulses. In ODMR experiments, off-resonance MW excitation can always happen due to wide MW excitation window ($\sim \frac{1}{t_{180}}$) and MW inhomogeneity around NV^- ensemble. It is obvious from Fig. 5.3 (a) that for a single phase measurement, both SQ and DQ coexist – the signal can be decomposed to 3 MHz and 6 MHz components. However in Fig. 5.3 (b), the linear combination of individual measurements

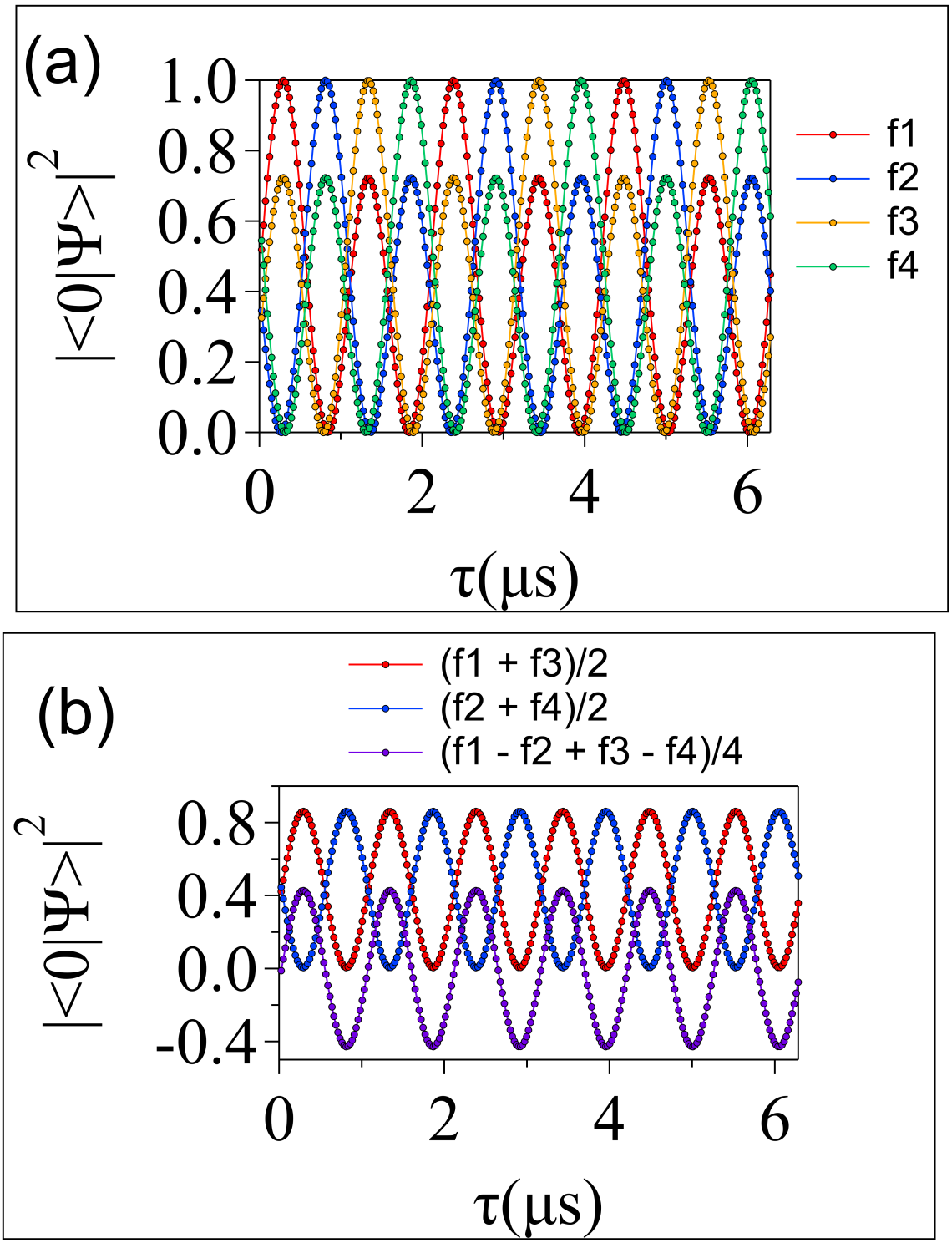

Figure 5.3: Numerical demonstration of phase cycling. The differential shift $\omega_{DF} = 3$ MHz and two tone pulse is set on resonance for both ± 1 transitions. The Rabi power $\gamma B_{MW} = 5$ MHz. (a) τ dependence for individual measurement. f1 f2 f3 f4 correspond to first 4 phase configurations in Table 5.1. All four signals have components at both 3 MHz and 6 MHz, indicating SQ and DQ contribution. (b) τ dependence for phase cycling. These linear combinations remove the 3 MHz SQ component, leaving only DQ contribution.

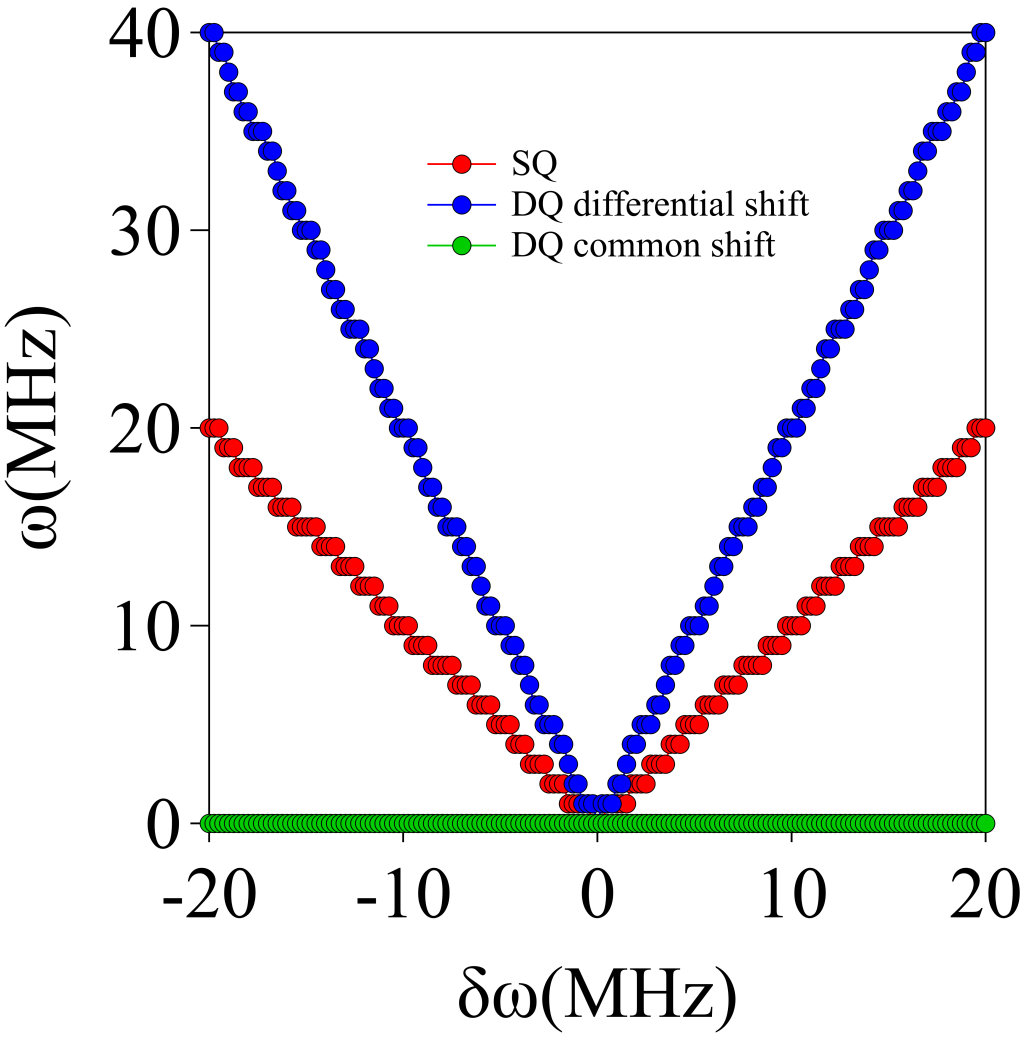

Figure 5.4: For Ramsey sequence, the final state probability $|\langle 0|\Psi\rangle|^2$ takes the form $A\cos(\omega\tau)$ in ideal case. The plot shows ω dependence on frequency shift $\delta\omega$.

can cancel out SQ components (blue and red) and the background (purple), indicating the pure DQ response in terms of period and intensity.

The pure DQ FL versus τ can be extracted by using the proper phase cycling. If we concentrate mainly on the frequency $\delta\omega$ of FL oscillation, we found that: when MW frequencies are on resonances ($\delta\omega = 0$), the final states show no difference from SQ on resonance results; when MWs have a non-zero common shift, $\omega_{CS} = \delta\omega$, as we expected that DQ detection is invariant under the common shift; As for a differential shift, $\omega_{DS} = \delta\omega$, the DQ Ramsey fringes have frequencies which is twice of $\delta\omega$. As for SQ, the Ramsey fringes show frequencies equal to $\delta\omega$. The FL oscillating frequency ω vs $\delta\omega$ is shown in Fig. 5.4.

5.5.2 Experimental study

Fig. 5.5(a) displays the DQ Ramsey response to the waiting time τ between two t_{180} pulses when both ± 1 transitions are on resonance. f1 f2 f3 f4 are four single phase measurements. It is obvious that each one of them contains three components from both SQ and DQ. In principle the resonance frequencies for both SQ and DQ are:

$$\mathrm{E_{SQ-}} = D_0 - \gamma B = 2.713 \text{ GHz} \tag{5.10}$$

$$\mathrm{E_{SQ+}} = D_0 + \gamma B = 3.028 \text{ GHz} \tag{5.11}$$

$$\mathrm{E_{DQ}} = 2\gamma B = 0.315 \text{ GHz} \tag{5.12}$$

However the τ dwell time is 4 μs, corresponding to $f_s = 0.25$ GHz sampling rate, which is insufficient to capture desirable frequencies in the first Nyquist zone. In other words, the peaks in FFT spectra in Fig. 5.5(b) are actually aliases of the target

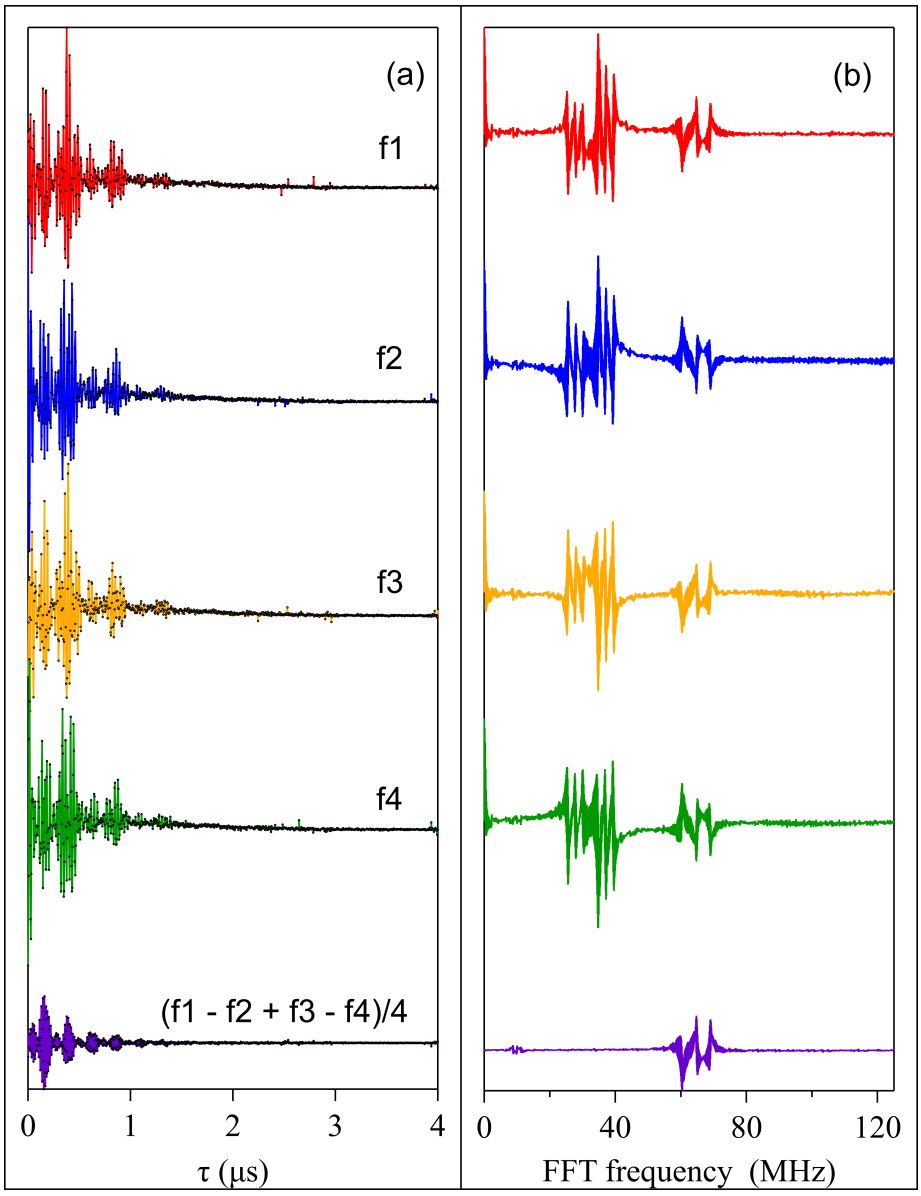

Figure 5.5: DQ Ramsey with phase cycling. The experiment is done under a 60 G bias field ambient condition. The Rabi power is about 5.5 MHz. The pulse sequence is the same as Fig. 5.2. (a) Measured DQ Ramsey FL contrast with different phase configurations. The definition of f1 f2 f3 f4 is the same as in Fig. 5.3. (b) complex FFT of Ramsey versus τ oscillation. The three groups of peaks correspond to SQ ± 1 and DQ components. The splitting of each group is due to the hyperfine coupling from NV^- spins to ^{14}N spins.

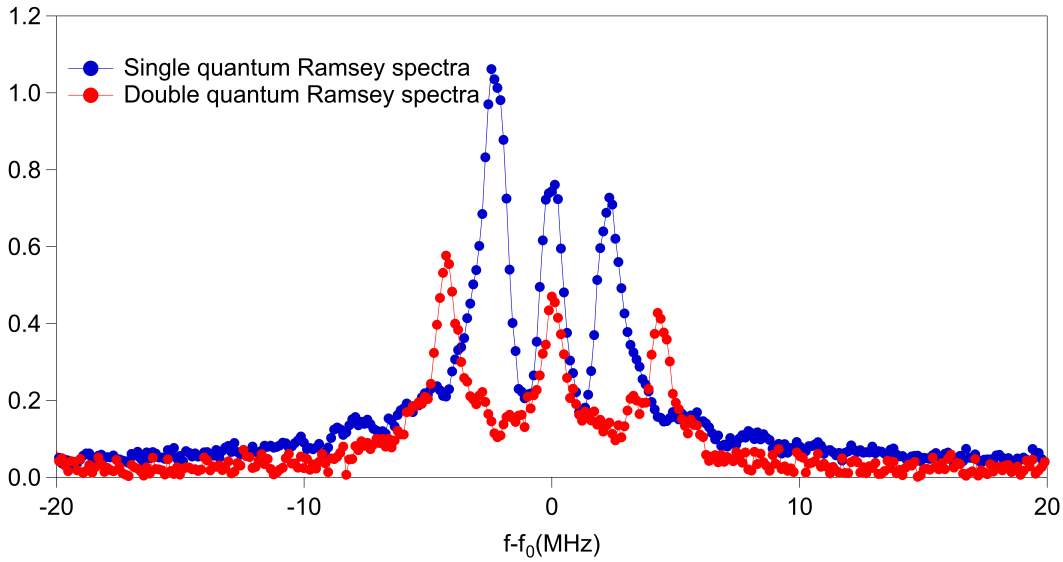

Figure 5.6: SQ and DQ Ramsey FFT spectra with both center shifting to 0. The plot is showing complex FFT magnitude. The splitting is due to ^{14}N hyperfine coupling.

signals. By shifting the signal with integer multiplies of f_s. We get:

$$E_{SQ-}{}' = |E_{SQ-} - 11f_s| = 37 \text{ MHz} \quad (5.13)$$

$$E_{SQ+}{}' = |E_{SQ+} - 12f_s| = 28 \text{ MHz} \quad (5.14)$$

$$E_{DQ}{}' = |E_{DQ} - f_s| = 65 \text{ MHz} \quad (5.15)$$

Comparing with FFT spectra, we can tell that the three groups of peaks from low to high frequencies are belonging to SQ +1, SQ -1 and DQ respectively. The ratio based on the peak area in the spectra is roughly 1:2:1. Hence we can quantitatively verify that only one fourth of the total signal is contributed by DQ.

By applying the proper phase cycling, both SQ components can be cancelled. A detailed comparison between SQ and DQ Ramsey spectra is shown in Fig. 5.6. Although the DQ signal has smaller intensity, the hyperfine splitting is twice as big than SQ. The three peaks arise from the term AS_zI_z, which can be understood as three sperate differential shifts, -A, 0, +A. Hence the DQ spectrum exhibits a $2A$ response.

The average peak width of SQ and DQ spectra are 1.265 MHz and 1.443 MHz respectively, which indicates similar T_2^* for both SQ and DQ under ambient condition. In Section 4.2.2, we notice that SQ T_2^* decreases dramatically due to strain distribution in DAC. We expect that DQ T_2^* will decay less since most of hydrostatic pressure inhomogeneity will be cancelled.

5.6 Future work

After demonstrating DQ Ramsey for NV^- ensembles, it is straightforward to apply it onto Ramsey sensing in the DAC. The line broadening from pressure inhomogeneity can be reduced, which makes the study of NV^- coupling to other nuclear spins versus pressure feasible. Also, instead of DQ Ramsey, more complex dynamical decoupling sequence should be able to apply using DQ, and AC sensing using DQ is a straightforward generalization.

Chapter 6

NMR study on $TmVO_4$

Nematicity and nematic correlations may play a role in the low temperature behavior of a number of strongly correlated electron systems, including the iron-based superconductors and the high temperature superconducting cuprates. Disentangling the effects of nematicity from other intertwined order parameters can help us understand its role better. The preferred candidate, $TmVO_4$, is an insulator and undergoes structure transition due to quadrupolar order at low temperature. It is a model system to study the roles played by nematic fluctuations and quantum phase transition by suppressing the nematic order. In this chapter, our preliminary NMR measurements and analysis will be discussed. Some challenges and potential solutions will also be introduced.

6.1 Crystal structure and ground state

$TmVO_4$ is an insulator that crystallizes in space group $I41/amd$ (see Fig. 6.1(a)). The Tm ions is in the $4f^{12}$ configuration. From Hund's rules, its 4f orbitals are filled such that L = 5, S = 1 and J = 6. Thus, for a local Tm site, the spherical harmonics Y_m^6 form the natural basis to construct wavefunctions. The surrounding ions create

Table 6.1: Character table for D_{2d}, with the reducible representations $\Gamma^{J=6}$

D_{2d}	E	$2S_4$	C_2	$2C_2'$	$2\sigma_d$
A_{1g}	1	1	1	1	1
A_{2g}	1	1	1	-1	-1
B_{1g}	1	-1	1	1	-1
B_{2g}	1	-1	1	-1	1
E_g	2	0	-2	0	0
$\Gamma^{J=6}$	13	-1	1	1	1

a crystalline electric field (CEF) that obeys the tetragonal point group symmetry D_{2d}[9], and so the degeneracy of the 13 Y_m^6 states is removed.

Now let's examine how the $\Gamma^{J=6}$ representation is reduced under CEF[49], which is:

$$\Gamma^{J=6} = \sum_i a_i \Gamma_i^{(irreducible)}, \tag{6.1}$$

where a_i is the number of each irreducible representation, which can be calculated using characters of representations:

$$a_i = \frac{1}{h} \sum_j N_j \chi^{\Gamma^{J=6}}(R_j) \chi^{\Gamma^{(irreducible)}}(R_j), \tag{6.2}$$

where h is the order of point symmetry group (for D_{2d} $h = 8$), N_j is the number of elements in class j, χ^Γ is the character of certain representation, and R_j is the group element.

Based on the character table 6.1, the energy level can be reduced to be:

$$\Gamma^{J=6} = 2A_{1g} \bigoplus 1A_{2g} \bigoplus 2B_{1g} \bigoplus 2B_{2g} \bigoplus 3E_g, \tag{6.3}$$

Nevertheless group theory does not determine the relative energies of these representations. The ground state of Tm ion can be obtained explicitly by solving CEF Hamiltonian:

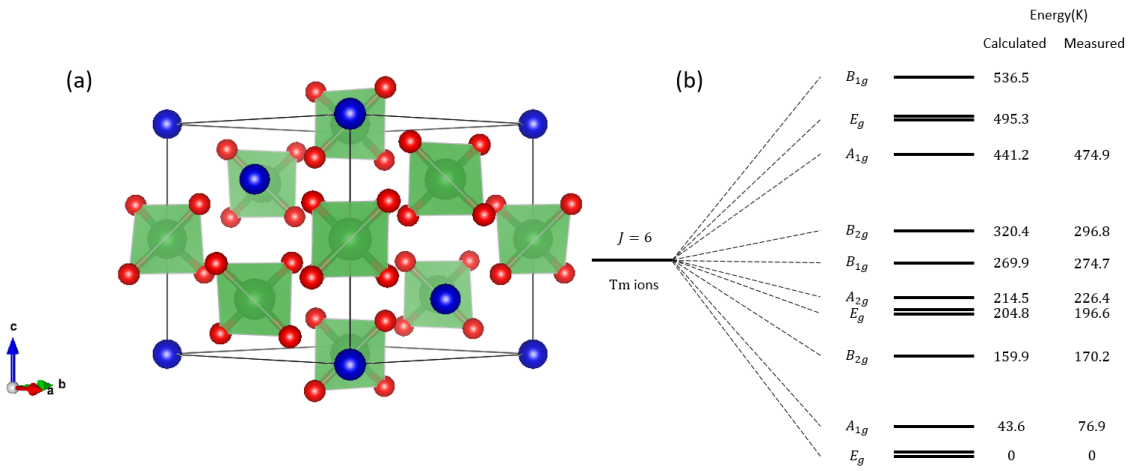

Figure 6.1: (a)$TmVO_4$ unit cell structure. Tm is blue, V is green (within the pyramids) and O is red.(b) The energy levels of Tm when the local J = 6 state is reduced in the D_{2d} CEF. The experiment data [88] is in agreement with calculation results using the CEF Hamiltonian.

$$H_{CEF} = B_2^0 O_2^0 + B_4^0 O_4^0 + B_6^0 O_6^0 + B_4^4 O_4^4 + B_6^4 O_6^4, \tag{6.4}$$

where O_i^j is spherical tensor operator (Stevens operator) and B_i^j is the coefficient.

Taking the coefficient from [88], the energy spectrum can be solved numerically using GT pack [32, 37] and is displayed in Fig 6.1(b).

It turns out that the ground state in the J_z basis,

$$|\psi_{1,2}\rangle = 0.89|\pm 5\rangle + 0.42|\pm 1\rangle + 0.19|\mp 3\rangle, \tag{6.5}$$

is a E_g doublet, which is also a non-Kramers doublet. The degeneracy of these ground states cannot be lifted by a magnetic field perpendicular to the z-direction because $\langle\psi_{1,2}|J_{\pm}|\psi_{1,2}\rangle = 0$. Thus $TmVO_4$ has non-zero g-factor $g_c \sim 10$ and $g_{ab} \sim 0$[9]. Due to the special nature of the ground state, phenomena such as strong magnetic anisotropy

and Jahn-Teller transition arise.

6.2 Ferroquadrupolar order

The first excited CEF state is 54 cm^{-1} above the ground state doublet [88], so at low temperatures the system is mainly controlled by the non-Kramers doublet. Since $g \sim 0$, the system cannot reduce the entropy by forming a magnetic order in the plane. Also the Tm's ground state has a rather large quadrupolar moment. It turns out that these local 4f quadrupolar moments spontaneously develop long-range order at $T_D = 2.18$ K. The heat capacity result is shown in Fig. 6.2. The transition reduces the overall system entropy and the data can be well described by mean-field solution of Ising model:

$$H_{QQ} = -\sum_{ij} J_{ij} O_2^2(i) O_2^2(j), \tag{6.6}$$

where O_2^2 is the Stevens operator representing the quadrupolar moments. The ground state doublet, however, can be linearly split by either a magnetic field oriented along the c-axis, or lattice strains with either a B_{1g} $(x^2 - y^2)$ or B_{2g} (xy) symmetry. These perturbations can be understood as a transverse field acting on ferroquadrupolar Ising model($\tilde{S} = 1/2$)[49].

Consequently, the transverse field H_c can tune $TmVO_4$ from ferroquadrupolar order to a quantum critical point (QCP). QCPs are critical points of continuous phase transitions that occur at zero temperature. Due to the absence of the thermal fluctuations, $TmVO_4$ offers an important platform to investigate quantum nematic fluctuations at a QCP.

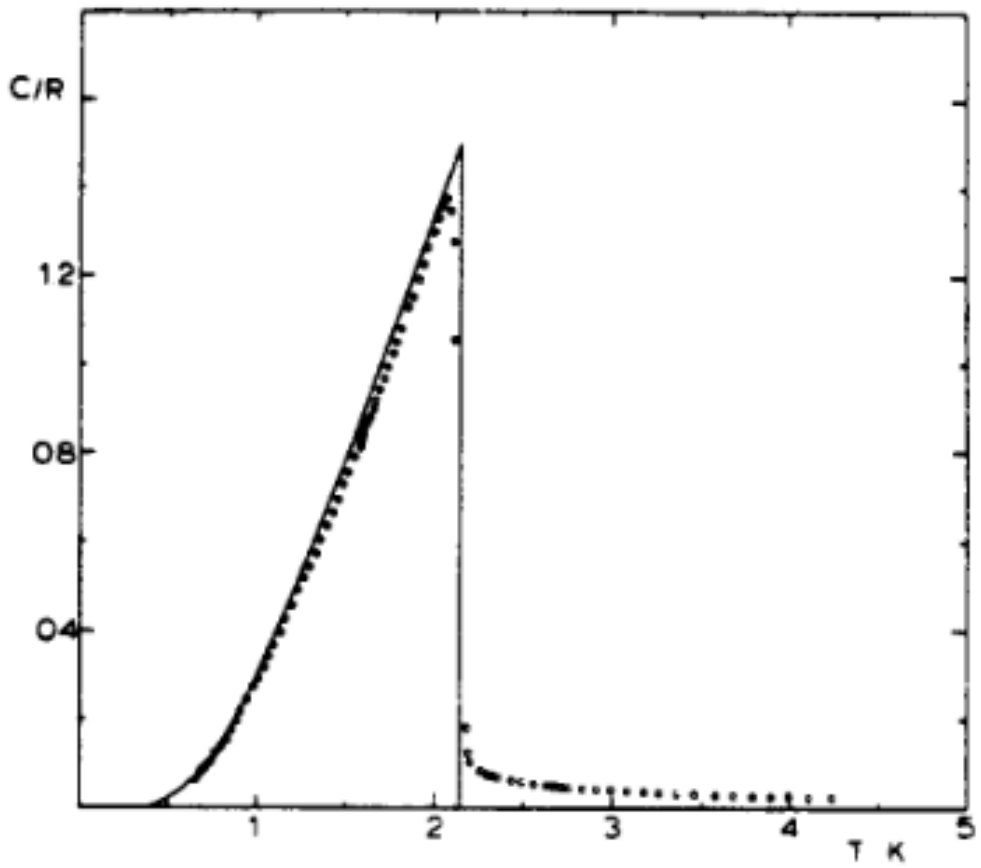

Figure 6.2: The specific heat of $TmVO_4$; the solid curve represents the result obtained from mean-field model [20].

In our experiment, we intend to use magnetic field H_c as the transverse field, which can be realized by rotating a fixed field between ab plane and c axis.

6.3 NMR method

$TmVO_4$ crystals were grown from a $Pb_2V_2O_7$ flux using 4 mole percent of Tm_2O_3, following the methods described in [29, 75]. The crystals have a rod-like morphology with the the c-axis along the long axis. A single crystal of approximate dimension

1mm × 1mm × 4mm was selected and rotated in the cryostat. While sample is rotating, the transverse field, $\mathbf{H}_0$ projection on sample c-axis, should follow $H_c = H_0 \cos\theta$, where θ is the angle between crystal c-axis and $\mathbf{H}_0$. Therefore when $H_c \sim 0.5$ T[52], the system should reach the QCP.

The ^{51} V(I = 7/2, Q = 52 mb, 99.75% abundant) NMR is investigated as the crystal is rotated [85]. Because the V has axial symmetry, the peaks frequencies are given by (Section 1.2):

$$\nu = \gamma H_0 \left(1 + K(\theta)\right) + n\nu_q(\theta), \tag{6.7}$$

where the magnetic, $K(\theta)$, and quadrupolar, $\nu_q(\theta)$, shifts vary with θ:

$$K(\theta) = K_{cc}\cos^2\theta + K_{aa}\sin^2\theta \tag{6.8}$$

$$\nu_q(\theta) = \nu_{zz}\left(3\cos^2\theta - 1\right)/2. \tag{6.9}$$

Here $\gamma = 11.193$ MHz/T, $n = -3, \cdots, 3$, $\nu_{zz} = eQV_{zz}/12h$ and V_{zz} is the electric field gradient(EFG) at the V site (details in chapter 1).

In Fig. 6.3, several spectra are fitted with Lorentzians from different θ angle at 210 K. Using a global fit for all seven transitions, the magnetic shift K_{aa}, K_{cc} and quadrupolar splitting ν_{zz} can be extracted. The absolute theta value θ_0 (when $\theta = 90°$ and θ_0 is the relative angle value set in the program) can also be determined.

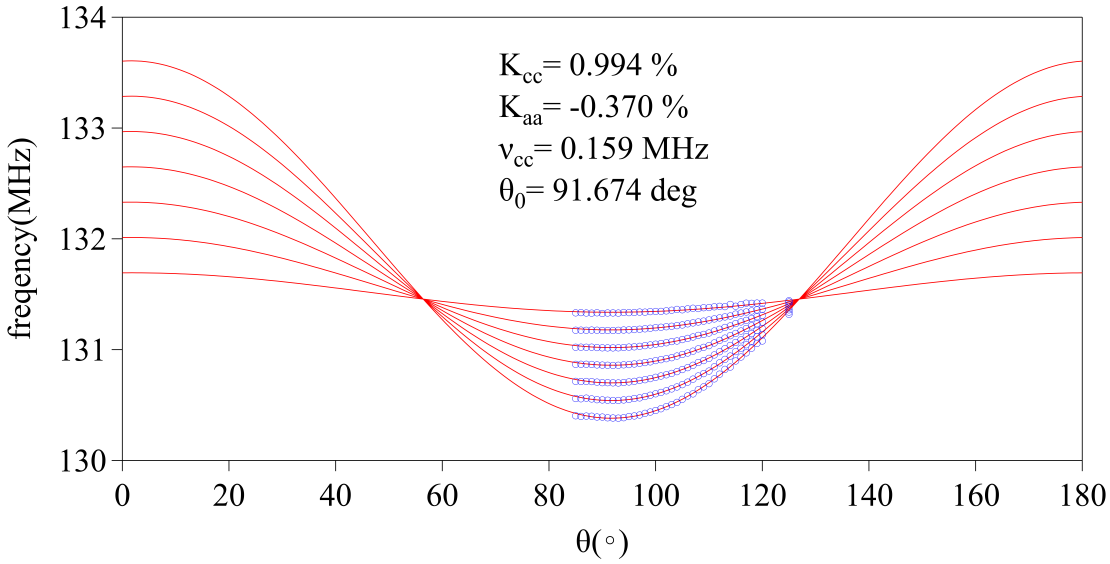

Figure 6.3: ^{51}V peak frequencies vs θ at 210 K

6.4 Spectra and magnetic shift

6.4.1 Torque misalignment

Based on the magnetic susceptibility data (Fig. 6.8(a) inset), the crystal has a strong anisotropy, reflecting the unusual g-factor ($g_c \approx 10.2$, $g_\perp = 0$) of the ground state doublet. This phenomenon can give rise to a misalignment at low temperature.

To be specific, the crystal will experience a torque:

$$\tau = |\mu \times \mathbf{H}|, \tag{6.10}$$

where μ is the total magnetic moment, and $\mathbf{H}$ is the external magnetic field. Since $g_\perp = 0$, it can be simplified to be:

$$\tau = \mu H_0 \cos\theta, \tag{6.11}$$

If the initial orientation is chosen to be in the plane where $\theta_0 = 90°$, the torque will grow monotonically once it is deviated from the initial condition (unstable equilibrium). Let $\theta_0 = 89°$ for estimation, then the torque will be:

$$\tau = \mu H_0 \cos\theta = N\frac{g_c\mu_B}{\hbar}\tilde{J}_z H_0 \cos 1° \sim 50N \cdot m \tag{6.12}$$

This large torque inevitably rotates the sample when temperature is below 80 K, which leads to hysteretic behavior as shown in Fig. 6.4. To alleviate this issue we secured the crystal with epoxy to a mounting plate that is locked by mechanical gears – the spectra remains unchanged while cooling and warming.

6.4.2 Spectra analysis

In order to avoid the backlash of our goniometer, the low temperature data were taken always rotating in one direction. In Fig. 6.5, ^{51}V spectra respect to different temperature and angle θ are displayed. It is important to state that below 80 K, the magnetic shift along the c-axis becomes much larger than that of ab plane. Therefore the angle deviation is small – in the range of 5 degrees with 0.5 degrees step. As temperature decreases, the central line intensity has minimum around 10 K then starts to increase, resulting in 'U' shape spectra at intermediate temperatures. This phenomenon arises due to fast spin-spin decoherence rates (T_2^{-1}) which will be discussed in the Section 6.5.5.

The temperature and angular dependence of the linewidths, EFG are shown in

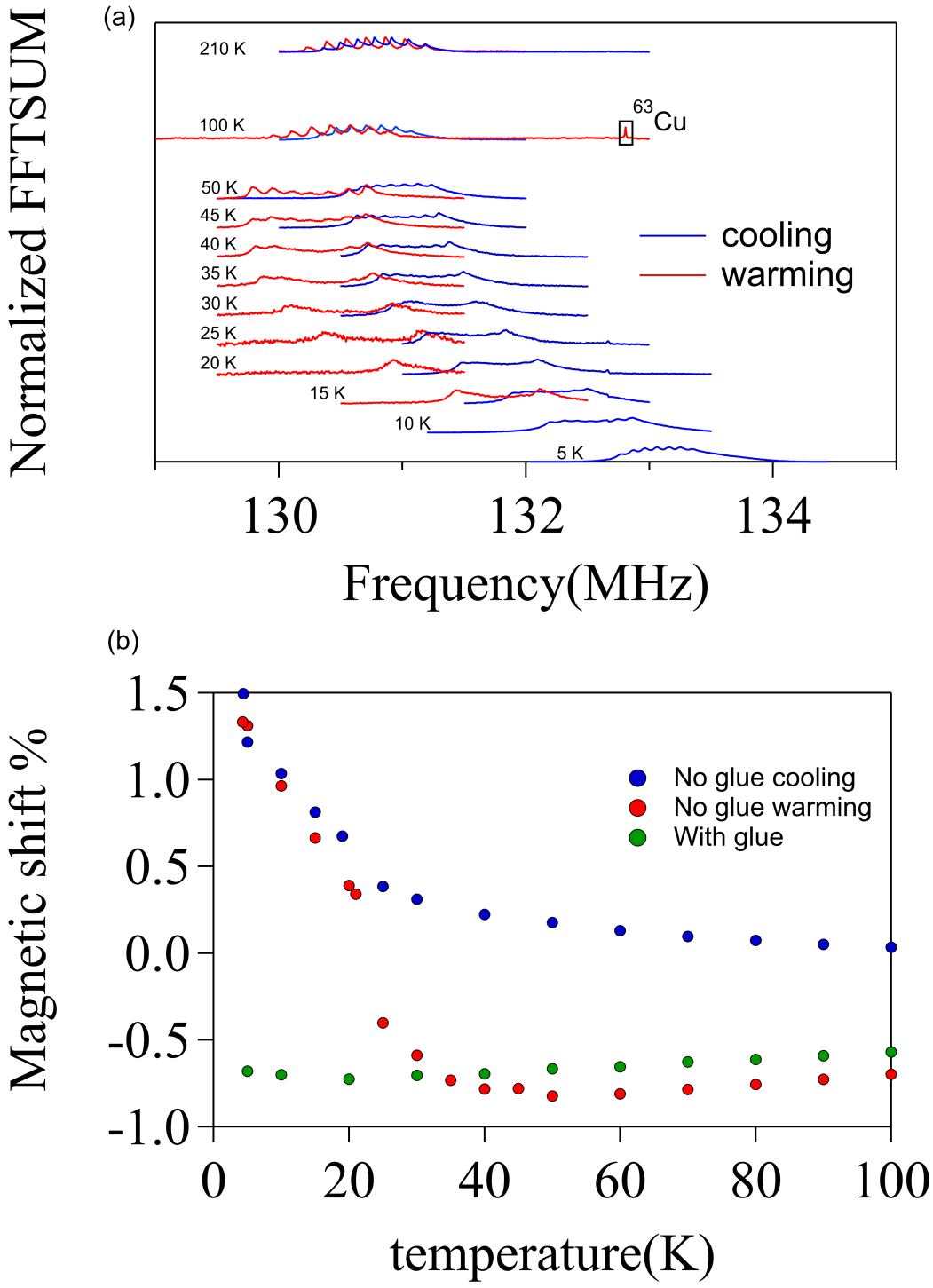

Figure 6.4: (a)^{51}V waterfall Spectra without epoxy mounting. The discrepancy between cooling and warming is due to sample rotating away from 90°; (b) Magnetic shift vs temperature while cooling, warming and epoxy mounting.

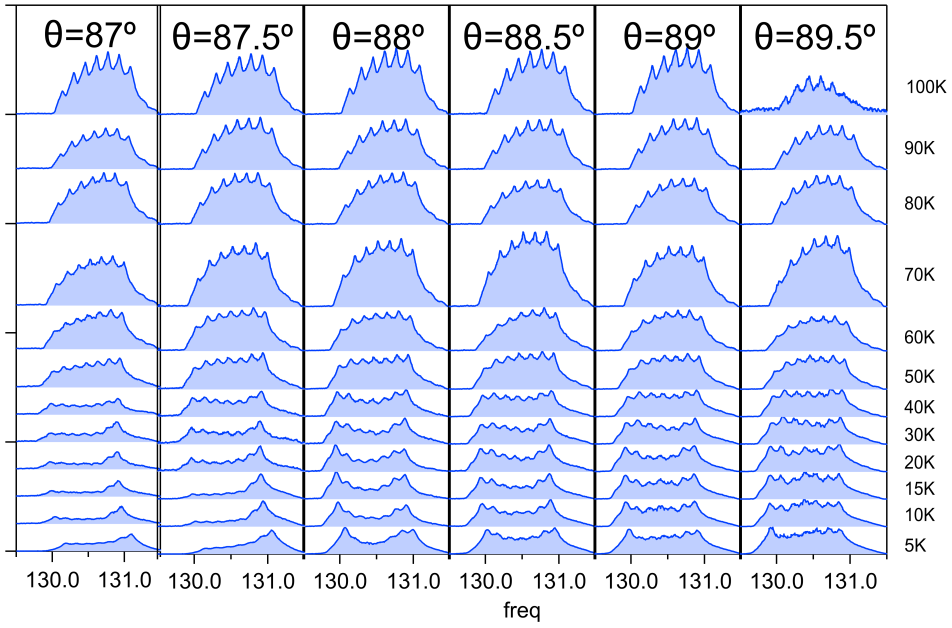

Figure 6.5: ^{51}V Spectra below 100 K vs different θ.

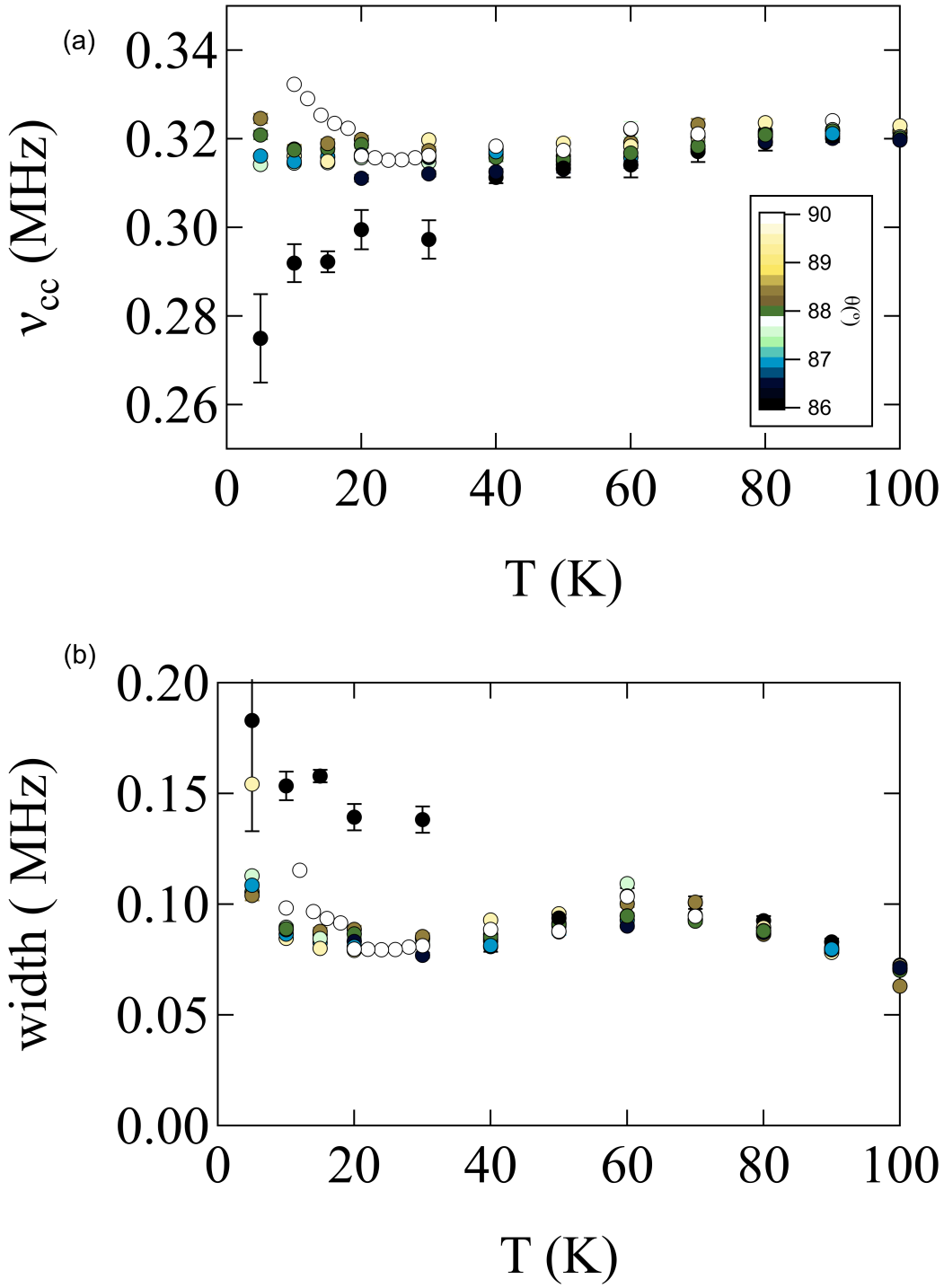

Figure 6.6: The (a) quadrupolar splitting and (b) full-width half maximum versus temperature for several different angles, θ.

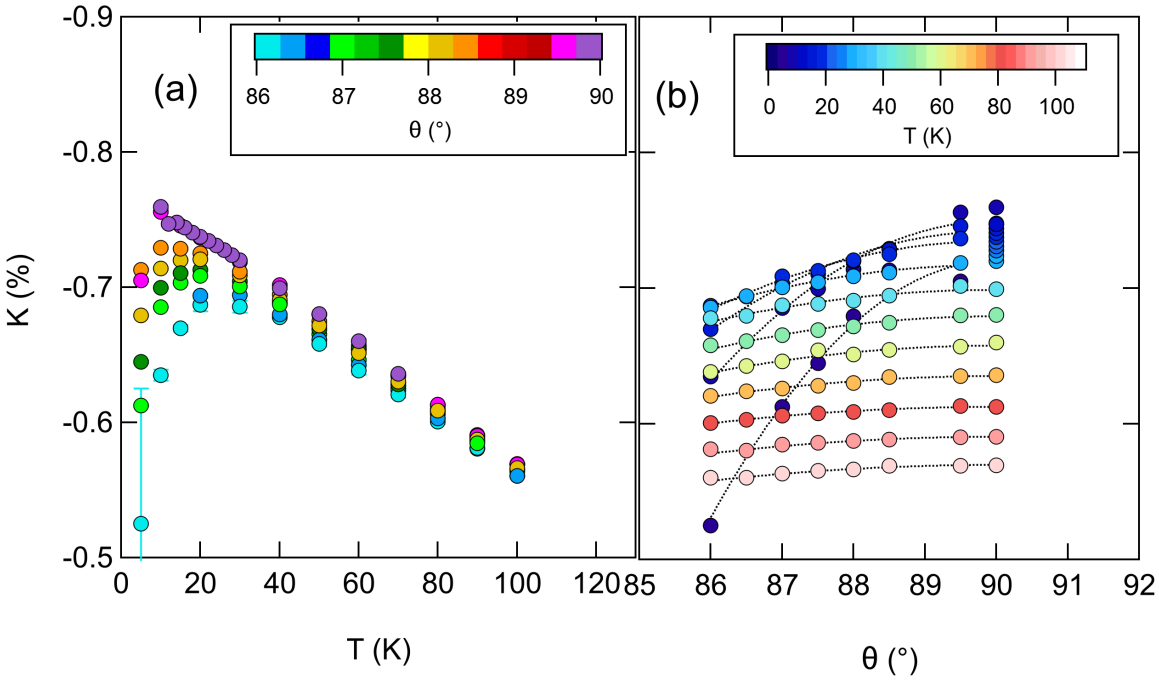

Figure 6.7: Magnetic shift, K, versus temperature (a) and versus θ (b). The dotted lines are fits as described in the text.

Fig. 6.6(a)(b). We find that the EFG is similar to previous measurements[9, 10]. However, the individual peaks become difficult to resolve at low temperatures. Each of the satellite resonances has the same linewidth, implying that the broadening is due to magnetic field inhomogeneity within the sample.

6.4.3 Magnetic shift

The magnetic shift shown in Fig. 6.7 is negative and strongly angular dependent at low temperature. We fit the angular dependence to extract the tensor components K_{aa} and K_{cc}, shown as dotted lines in Fig. 6.7(b). This approach enables us to extract the magnetic shift for the c direction without needing to fully align the crystal in this orientation, although the error bars for K_{cc} are larger than for K_{aa}. The temperature dependence of K_{aa} and K_{cc} are shown in Fig. 6.8(a). K_{cc} is large and positive.

Fig. 6.8(b) shows these shift components plotted versus the bulk susceptibility $\chi_{aa,cc}$, which was measured independently in a SQUID magnetometer. The shift varies linearly with susceptibility as $K_{\alpha\alpha} = K^{orb}_{\alpha\alpha} + A_{\alpha\alpha}\chi_{\alpha\alpha}$, where $A_{\alpha\beta}$ are the components of the hyperfine coupling tensor. The linear fitting reveals that $K^{orb}_{aa} = -0.315 \pm 0.009\%$, $K^{orb}_{cc} = -0.4 \pm 0.1\%$, $A_{aa} = -0.32 \pm 0.07$ kOe/μ_B and $A_{cc} = 1.29 \pm 0.05$ kOe/μ_B. These values of the hyperfine couplings are consistent with a direct dipolar coupling mechanism between the Tm moments and the V nuclear spins.

The magnetic field on V site can be written as:

$$\begin{aligned} \mathbf{h}_{dipole} &= \sum_i (\nabla \times \mathbf{A}_i) \\ &= \sum_i \left(\frac{3\mathbf{r_i}(\mu_\mathbf{i} \cdot \mathbf{r_i})}{r_i^5} - \frac{\mu_\mathbf{i}}{r_i^3}\right) \\ &= \mathbb{A}^{dip} \cdot \mu, \end{aligned} \tag{6.13}$$

where $\mathbb{A}^{dip}$ is the dipolar coupling tensor, μ is the magnetic dipole moment located at lattice site $\mathbf{r}_i$ relative to V. Due to the symmetry, the coupling tensor only has diagonal terms and $A^{dip}_{aa} = A^{dip}_{bb}$. Therefore the couplings can be calculated using the total magnetic field and magnetic moments.

To be specific, a 3×3 supercell is used to estimate the contribution from all the magnetic moments. The target V site is chosen in the center of the supercell and each Tm ion's contribution is counted (oxygen ions have closed shells so it is ignored). The numerical calculation gives: $A^{dip}_{aa}(A^{dip}_{bb}) = -0.336$ kOe/μ_B and $A^{dip}_{cc} = 0.671$ kOe/μ_B at the V site.

The simulation for the perpendicular direction is the same as the measured value within the error limits. For the c axis, the theoretical value is within a factor of two of the measured values, and it is likely there are larger systematic measurement

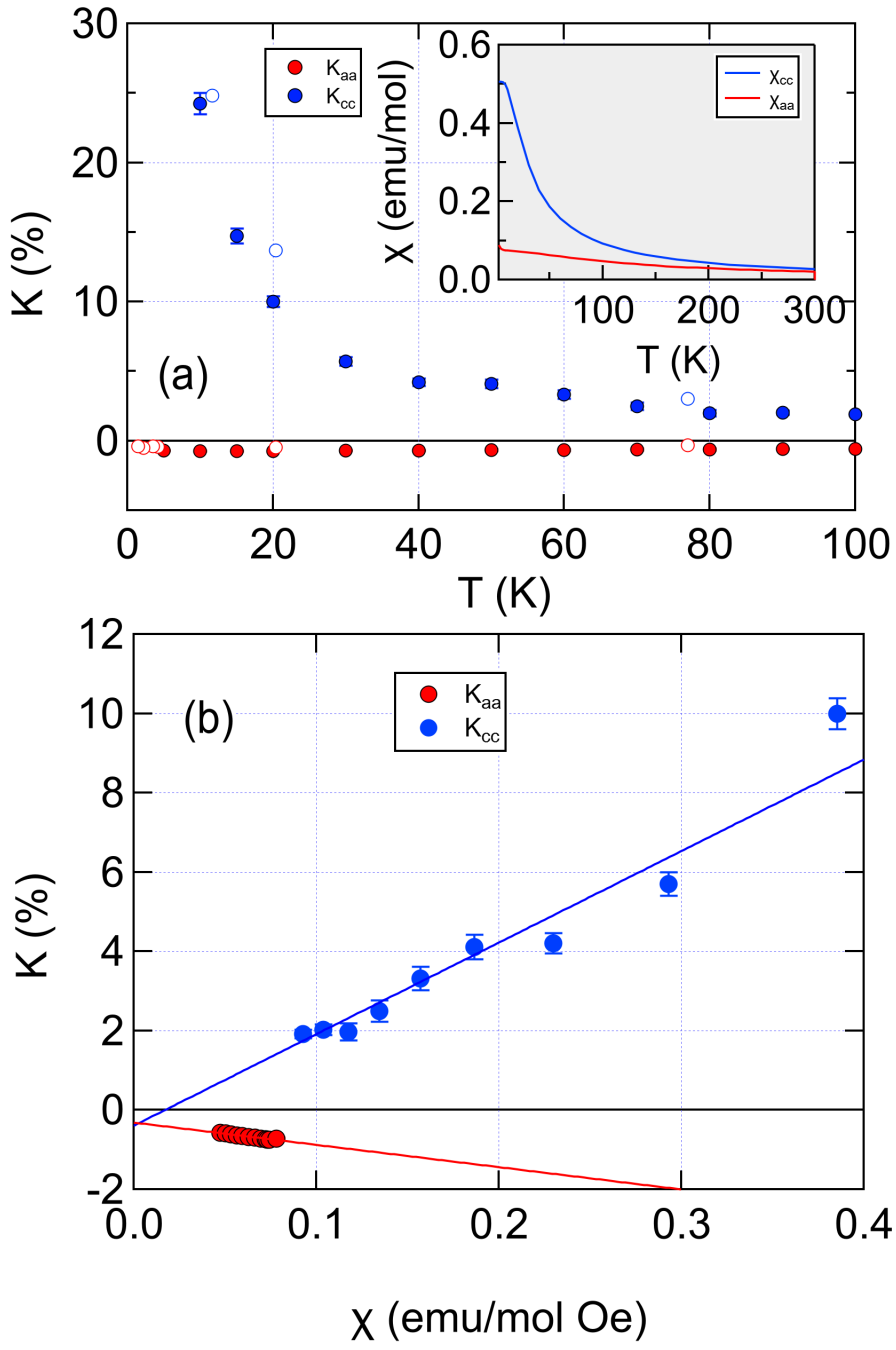

Figure 6.8: K_{aa} and K_{cc} versus temperature (a) and versus bulk susceptibility (b). The open points correspond to values reported in [9]. The solid lines are fits as described in the text. The inset displays the bulk susceptibility versus temperature.

errors involved in extracting this value through a small angle deviation. Still the anisotropic magnetic shift tensor can be fully explained via direct dipolar interactions, as expected for an insulator.

6.5 Relaxation

6.5.1 Spin lattice relaxation $\mathbf{T}_1$

The spin-lattice-relaxation, T_1, was measured by applying inversion pulses at the central transition ($n = 0$) and measuring the echo intensity as a function of recovery time using low power inversion pulses with small bandwidths (pulse widths 6-8 μs), repetition time 10 ms, and pulse power of 39-44 dBm. The magnetization recovery was fit to the standard expression for magnetic fluctuations: $M(t) = M_0\,(1 - 2f\phi(t/T_1))$ (see Section 1.6.2), where M_0 is the equilibrium magnetization, f is the inversion fraction, and

$$\phi(t) = \frac{1225}{1716}e^{-28t} + \frac{75}{364}e^{-15t} + \frac{3}{44}e^{-6t} + \frac{1}{84}e^{-t}. \tag{6.14}$$

This expression fits the data well without the need for a stretching exponent. Fig. 6.9 shows the temperature and angular dependence of T_1^{-1}. For $\theta = 90°$, T_1^{-1} decreases strongly below 80K as the excited crystal field levels are thermally depopulated. In this temperature range T_1^{-1} become strongly angular dependent, increasing by more than a factor of 30 as the field $\mathbf{H}_0$ rotates by only 4° away from the perpendicular configuration. This behavior likely reflects the anisotropy of the g factor of the ground state doublet, however the anisotropy of T_1^{-1} is puzzling. In most of the cases, the relaxation is driven by magnetic fluctuations of the Tm ground state. If it is true, T_1^{-1} should exhibit a *maximum* at $\theta = 90°$ rather than a minimum because fluctuations of the non-Kramers doublet should lie exclusively along the c-axis. Therefore $T_1^{-1}(0°)$

should be much smaller than $T_1^{-1}(90°)$, in contrast to our observations.

6.5.2 T_1^{-1} angular dependence – magnetic fluctuation

For most NMR measurements, the magnetic shift reflects dipolar coupling with the static magnetic moment μ, and the spin lattice relaxation rate reflects dipolar coupling with the time varying magnetic moment $\mu(t)$, when magnetic fluctuations dominate such that $T_1^{-1} \sim W_m$.

If the external field is aligned along the crystal a(x)-axis, the relaxation rate generated by magnetic fluctuation is given by (Section 1.6.2):

$$W_m = \frac{\gamma^2}{2}\int_0^\infty (\langle h_z(\tau)h_z(0)\rangle + \langle h_y(\tau)h_y(0)\rangle)e^{-\omega_L\tau}d\tau, \tag{6.15}$$

where $h_i(t)$ is the fluctuating fields on V site and ω_L is the Lamour frequency.

By the rotation on the y axis, when the angle between the sample c axis and the field direction is θ, $h_{z'} = h_z\sin\theta + h_x\cos\theta$. If we assume that there is no correlation between different axis, $\langle h_i(\tau)h_j(0)\rangle = 0$ if $i \neq j$, then the relaxation rate becomes:

$$W_m(\theta) = \frac{\gamma^2}{2}\int_0^\infty (\sin^2\theta\langle h_z(\tau)h_z(0)\rangle + \cos^2\theta\langle h_x(\tau)h_x(0)\rangle + \langle h_y(\tau)h_y(0)\rangle)e^{-\omega_L\tau}d\tau \tag{6.16}$$

Using the approximation in [74], $\langle h_z(\tau)h_z(0)\rangle = h_{z0}^2 e^{-\frac{|\tau|}{\tau_0}}$, where h_{z0} is the static coupling field and τ_0 is the correlation time. By integrating over τ, we obtain:

$$W_m(\theta) = \frac{\gamma^2}{2}(h_{z0}^2\sin^2\theta + h_{x0}^2\cos^2\theta + h_{y0}^2)\frac{2\tau_0}{1+(\omega_L\tau_0)^2} \tag{6.17}$$

It can also be written as:

$$T_{1m}^{-1} = W_m(\theta) = W_m(0)\cos^2\theta + W_m(90°)\sin^2\theta. \tag{6.18}$$

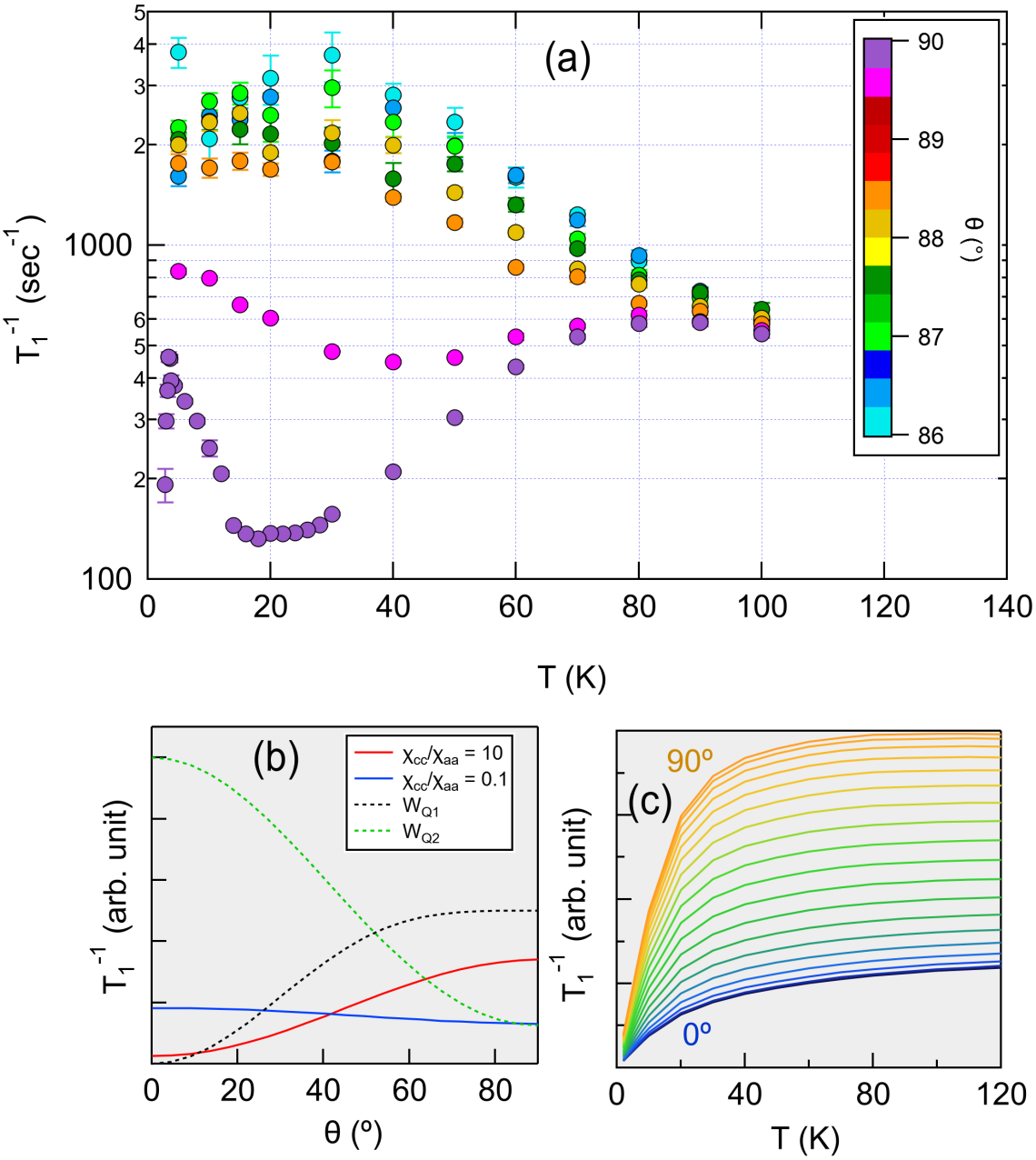

Figure 6.9: (a) T_1^{-1} vs temperature for multiple angles. (b) Calculated T_1^{-1} versus θ for magnetic fluctuations (solid lines) and for quadrupolar fluctuations (dashed lines). (c) Calculated T_1^{-1} versus temperature and angle using Eq. 6.18, where the angle is increased in 5° increments between 0 and 90°.

We know that the static coupling field can be presented as $h_{i0} = A_{ii}^{dip}\mu_i \sim A_{ii}^{dip}\chi_{ii}$. Fig. 6.9(b) displays the expected angular dependence of T_{1m}^{-1} for $\chi_{cc}/\chi_{aa} = 10$ (red), close to the experimental value, and for $\chi_{cc}/\chi_{aa} = 0.1$ (blue). The former clearly exhibits a maximum of T_{1m}^{-1} at $\theta = 90°$, in contrast to our observations. The latter exhibits a shallow minimum at 90°, but the susceptibility anisotropy does not agree with experiment. Fig. 6.9(c) shows the temperature dependence using the measured values of the static susceptibility. Although there is an overall decrease in T_{1m}^{-1} at lower temperatures, the detailed temperature dependence does not match experiment.

To sum up, the experiment T_1^{-1} data cannot be well explained by the single magnetic fluctuation. Since the system forms ferroquadropolar order below T_Q, it is natural to take the quadrupolar fluctuations into consideration.

6.5.3 T_1^{-1} angular dependence – quadrupolar fluctuation

An alternative explanation is that the T_1^{-1} is dominated by quadrupolar fluctuations rather than magnetic. The Tm quadrupole moments couple to the EFG at the V site, giving rise to a second nuclear quadrupolar relaxation channel [23]. The enhancement of T_1^{-1} below 20K for $\theta = 90°$ may represent the growth of critical fluctuations near T_Q. In the presence of both magnetic and quadrupolar relaxation, the expression for $\phi(t)$ (Eq. 6.14) changes, and includes three independent rates: T_{1m}^{-1}, W_{Q1} and W_{Q2}, where the latter two are associated with $\Delta m = \pm 1$ and $\Delta m = \pm 2$ quadrupolar relaxation.

For a tetragonal to orthorhombic distortion, quadrupolar relaxation is driven by fluctuations of the spherical tensor components of the EFG: $V_{\pm 1} = V_{zx} \pm iV_{zy}$ and $V_{\pm 2} = \frac{1}{2}(V_{xx} - V_{yy}) \pm iV_{xy}$, where the $V_{\alpha\beta}$ are the EFG tensor components relative to the direction of $\mathbf{H}_0$. These give rise to nuclear spin relaxation rates (Section 1.6.2):

$$W_{Q1,Q2} = (eQ)^2 \int_0^\infty \langle V_{+1,2}(\tau) V_{-1,2}(0)\rangle e^{-\omega_L \tau} d\tau \tag{6.19}$$

where ω_L is the Larmor frequency [79]. Initially the field H_0 is along c axis ($\theta = 0$). As the field is rotated towards the plane, the tensor operators $V_m(\tau)$ transform as:

$$V'_m(\tau) = \sum_{m'} D^{(2)}_{mm'} V_{m'}(\tau) \tag{6.20}$$

where

$$D^{(l)}_{mm'}(\alpha, \beta, \gamma) = e^{-im\alpha} d^l_{mm'}(\beta) e^{-im'\gamma}, \tag{6.21}$$

are the Wigner D matrices, and the Euler angles are ($\alpha = \phi, \beta = \theta, \gamma = 0$). The correlation functions $\langle V_m(\tau) V_{-m}(0)\rangle$ are thus given by:

$$\langle V'_m(\tau) V'_{-m}(0)\rangle = \sum_{m',m''} D^{(2)}_{2m'}(\phi,\theta) D^{(2)}_{-2m''}(\phi,\theta) \langle V_{m'}(\tau) V_{m''}(0)\rangle. \tag{6.22}$$

Assuming $\langle V_i(\tau) V_j(0)\rangle = 0$ if $i \neq j$, then relaxation rate turns to:

$$\begin{aligned} W_{Q1}(\theta) &= P_1(\theta) W_{Q1}(0) + P_2(\theta) W_{Q2}(0) \\ W_{Q2}(\theta) &= Q_1(\theta) W_{Q1}(0) + Q_2(\theta) W_{Q2}(0) \end{aligned} \tag{6.23}$$

The ferroquadrupolar order in this system has B_{2g} symmetry, so $V_{xx} - V_{yy} \neq 0$, where z corresponds to the c-direction and x and y are along the principal axes of the EFG tensor, which are rotated 45° relative to the tetragonal a-axes. Therefore above T_Q fluctuations of $V_{\pm 2}$ should dominate those of $V_{\pm 1}$, and as a result we anticipate that $W_{Q1}(0)$ can be neglected, which gives:

$$\begin{aligned} W_{Q1}(\theta) \sim P_2(\theta) W_{Q2}(0) &= \frac{\cos^4\theta + 6\cos^2\theta + 1}{8} W_{Q2}(0) \\ W_{Q2}(\theta) \sim Q_2(\theta) W_{Q2}(0) &= \frac{\sin^2\theta(\cos(2\theta) + 3)}{4} W_{Q2}(0) \end{aligned} \tag{6.24}$$

These quantities are shown in Fig. 6.9(b) as dashed lines. W_{Q2} exhibits a minimum

for $\theta = 90°$, whereas W_{Q1} is nearly independent of θ at this angle. This behavior agrees qualitatively with our observations, but the increases we observe are in fact a much stronger function of angle than expected for quadrupolar relaxation. Rotating θ by 1-2° out of the plane enhances T_1^{-1} by an order of magnitude, whereas W_{Q2} exhibits only a quadratic minimum at this angle.

It is worthy to mention that when $\theta = 90°$, $W_{Q1} = 4W_{Q2}$, which is different from $\theta = 0°$. Hence the critical fluctuation at $\theta = 0°$ (bottom purple data in Fig. 6.9(a)) is more likely dominated by W_{Q1}.

6.5.4 Relation to stiffness coefficient c_{66}

By Hooke's law, we know:

$$\sigma_i = c_{ij}\epsilon_j (i, j = 1, 2, ..., 6), \tag{6.25}$$

where ϵ_i and σ_i represents strain and stress respectively on the certain surface (x, y, z) and the certain direction (x, y, z).

Based on [63], for some space groups, in the Voigt notation convention, including that of $TmVO_4$, the shear stress $\sigma_6 = \sigma_{xy} = \sigma_{yx}$ follows:

$$\sigma_6 = c_{66}\epsilon_6. \tag{6.26}$$

In this material c_{66} softens as temperature decreases to T_Q. Fig. 6.10 compares the temperature dependence of T_1^{-1} and that of c_{66}, which softens with decreasing temperature and vanishes at T_Q [58]. This behavior is driven by the nematic susceptibility: $\chi_{nem} = c_{66,0}(1 - c_{66,0}/c_{66})/\lambda^2$, where λ is the coupling between the lattice and the Tm 4f orbitals, and $c_{66,0}$ is the stiffness coefficient in the absence of the coupling [31]. If T_1^{-1} is also determined by the Tm orbital fluctuations, then $(T_1T)^{-1} \sim \chi_{nem}$[23, 46, 66]. We thus expect $T_1T \sim (c_{66,0}/c_{66} - 1)^{-1}$, which is demonstrated in Fig. 6.10.

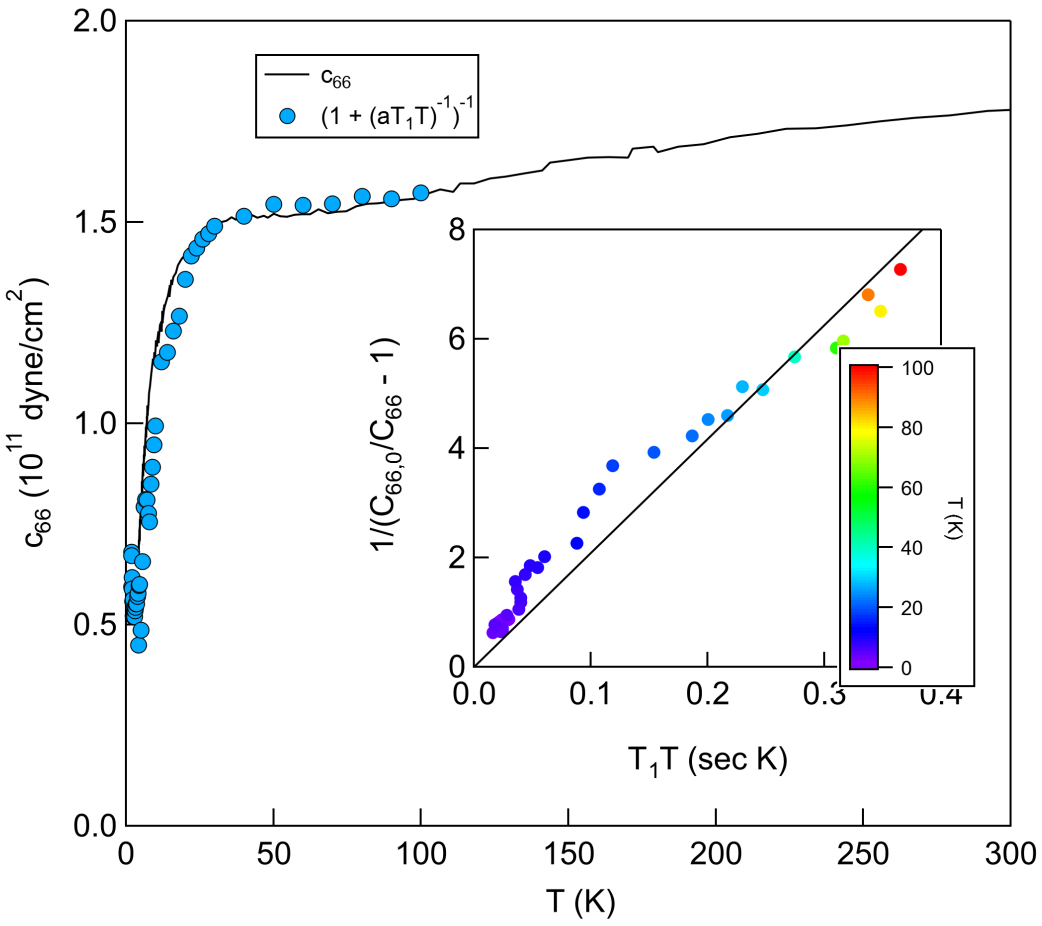

Figure 6.10: The shear elastic stiffness coefficient c_{66} (solid line, reproduced from [58]) and the quantity $1/(1+(aT_1T)^{-1})$ as a function of temperature. INSET: $1/(c_{66,0}/c_{66}-1)$ versus T_1T, with temperature implicit. The solid black line is the best linear fit, giving $a = 18.5 \pm 0.4$ sec^{-1} K^{-1}.

The main panel compares the temperature dependence of c_{66} with the measured T_1^{-1} values, and the inset shows the scaling between the shear modulus and T_1^{-1} with temperature as an implicit parameter. The scaling in Fig. 6.10 suggests that the spin lattice relaxation is driven primarily by quadrupolar fluctuations, which are reflected in the softening of c_{66}.

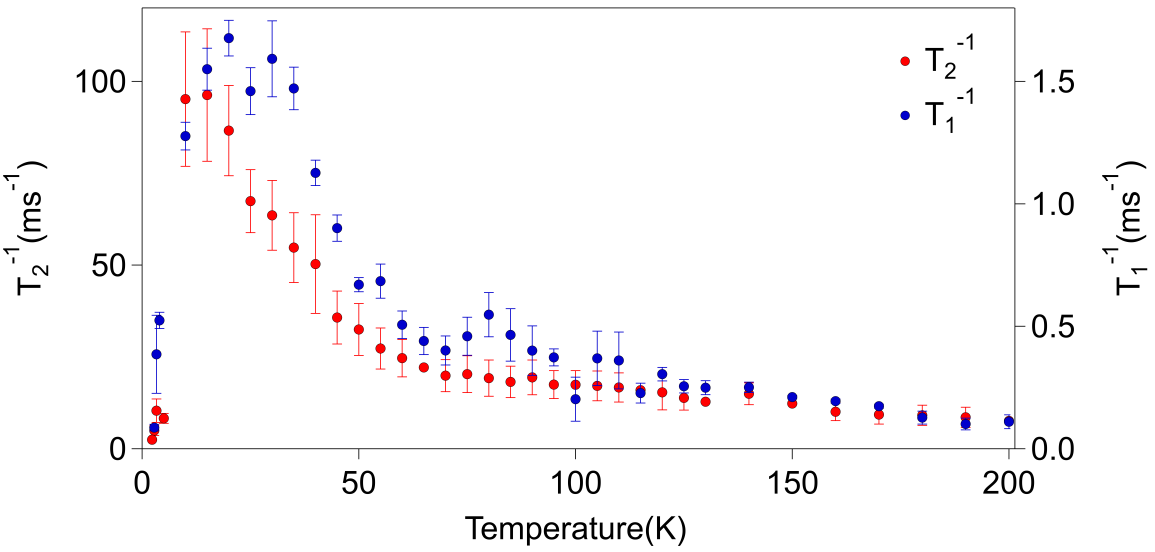

Figure 6.11: T_2^{-1} and T_1^{-1} temperature dependence when $\theta \sim 90°$

6.5.5 spin-spin decoherence T_2

The T_2^{-1} relaxation rate describes nuclear spin coherence time in superposition state. Similar to NV^- centers, the coherence can be extended by dynamical decoupling sequence – in this case it is spin echo.

Fig. 6.11 displays both T_2^{-1} and T_1^{-1} temperature dependence at a orientation that θ is near 90°. Two relaxation rates have a very similar temperature dependence except $T_2^{-1} \sim 66\ T_1^{-1}$.

The same temperature dependence implies T_2^{-1} is also driven by quadrupolar fluctuations, which can be understood by Redfield theory (Eq. 1.79). This result suggests that T_2^{-1} is a better indicator of the dynamical nematic susceptibility χ_{nem}.

6.6 Some improvements

6.6.1 FIB ellipsoid crystal

During the temperature dependence measurements, we find that 7 peaks broadens dramatically that eventually wash out the quadrupolar splitting ($\sim$ 150 kHz). All

peaks are broadened in the same way and the linewidth's temperature dependence suggest that the broadening is due to demagnetizing field.

The prism shaped crystal is located in a homogenious applied field $\mathbf{B_0}$, which polarizes the magnetic moments and creates a magnetization $\mathbf{M}$ in the sample. Continuity of the flux-density $\mathbf{B} = \mu_0\mathbf{M} + \mathbf{B_0}$ across the sample surface requires a demagnetizing field $\mu_0\mathbf{H}_d$ in addition to $\mathbf{B}_0$ [12]. In an arbitrarily shaped sample $\mu_0\mathbf{H}_d(\mathbf{r})$ and hence $\mathbf{B}(\mathbf{r})$ will be inhomogeneous and the NMR spectrum will be broadened because the nuclei each resonate at the local field [43]. In most cases this broadening is not sufficient to cause any significant problems for NMR, however in $TmVO_4$ the non-Kramers doublet has $g_c \approx 10$ and $g_{ab} = 0$. Although $\mathbf{B}_0$ can be oriented perpendicular to c, parts of the crystal near edges and corners tend to have components of $\mathbf{B}$ parallel to c, which exacerbates the broadening effect due to the large anisotropy of the susceptibility.

Fortunately, $\mu_0\mathbf{H}_d$ can be made homogeneous by cutting the sample in either a spherical or ellipsoidal shape [65]. For these studies we utilized a focused ion beam (FIB) to cut our sample to an ellipsoid with the long-axis along the c-axis of the crystal [60], as illustrated in Fig. 6.12(b,c) [82]. The sample is cut from a carefully aligned cuboid from which calculated and programmed concentric circles are removed using by a xenon plasma FIB by Kent Shirer at the MAx Planck Institute in Dresden with a 30 kV, 1 μA beam. Sample damage from the beam is only expected on the surface within a depth of $30-40$ nm and Energy Dispersive X-Ray Analysis (EDX) of a test surface verifies the unchanged composition of $TmVO_4$ below. The final sample diameter is 0.4 mm and the length of 1.3 mm require a total cutting time in excess of 25 h of each side. In the FIB process Al and C are deposited on the sample surface layer, however these do not affect the NMR signal from the bulk of the sample.

Fig. 6.12(d) compares the NMR spectrum of the uncut with the FIB crystal. It is clear that the magnetic broadening is dramatically reduced in the FIB crystal,

such that each of the seven peaks separated by the quadrupolar splitting are clearly resolved. The ability to resolve all seven peaks is important because it enables us to extract details of the magnetic and quadrupolar contributions to the T_1^{-1} that would otherwise be inaccessible, as discussed below.

6.6.2 Multi-channel relaxation fitting

In general, there are three distinct relaxation channels: a magnetic, W_m, and two quadrupolar relaxation rates, W_{Q1} and W_{Q2}. In Section 6.5 we demonstrated that by analyzing the T_1^{-1} angular dependence it is certain that quadrupolar relaxation channel plays dominating role in the relaxation. However still it is difficult to disentangle the contribution of each channel's contribution [79]. These relaxation channels couple different sets of the I_z nuclear spin levels. The relaxation measured at a particular nuclear spin transition $m \leftrightarrow (m-1)$ is a complicated function of W_m, W_{Q1} and W_{Q2} determined by a master equation (with an 8×8 dimensional matrix for spin 7/2 of ^{51}V). The relaxation function for each transition is slightly different, thus by measuring the relaxation at multiple transitions one can globally fit the set of seven recovery curves to extract W_m, W_{Q1} and W_{Q2}. In order to do so it is vital to resolve and excite each transition in the spectrum individually. The inhomogeneous broadening from the demagnetization field precluded such studies previously, but fortunately all seven transitions are clearly visible in the FIB sample [82].

Fig. 6.13 shows values obtained at each of the seven peaks by fitting the measured relaxation curves by the formulae corresponding to the magnetic relaxation only. The data is measured when $\theta = 90°$.

If there were only magnetic fluctuations, all seven peaks would be described by a single value of $T_{1,mag}^{-1} = 2W_m$, shown by the dotted line in Fig. 6.13(a). Such a model clearly does not fit the data, which reveal a significant enhancement of the relaxation of the satellites. On the other hand, including a finite W_{Q1} accurately captures the

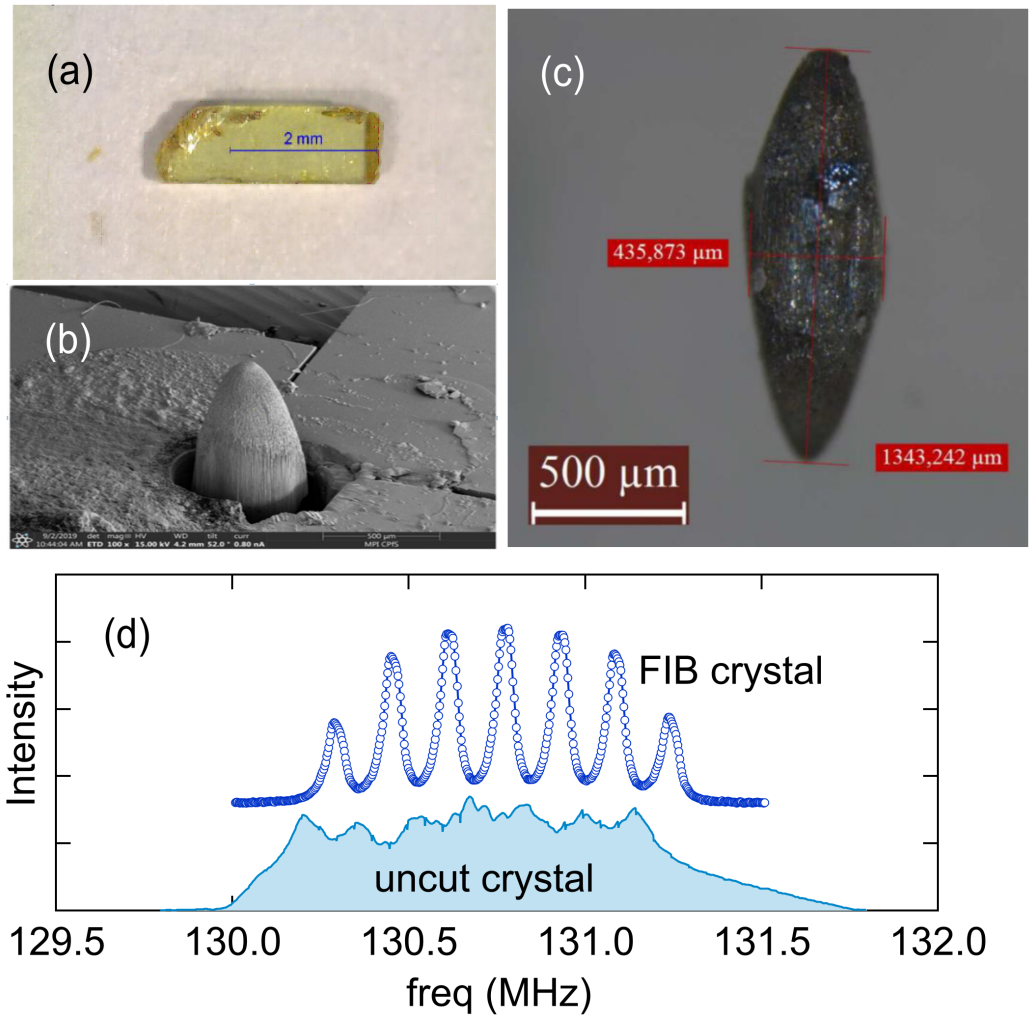

Figure 6.12: (a) Uncut sample of $TmVO_4$. (b) Scanning electron microscopy (SEM) scan of the sample during the FIB process. (c) Crystal after FIB. Al and C are deposited on the sample surface layer during the FIB processing, but do not contribute to the NMR signal. (d) ^{51}V-NMR spectra of ellipsoidal (FIB) and uncut samples measured at T=10 K and B_0=11.7294 T, illustrating the broadening effect of the inhomogeneous demagnetization field on the seven nuclear spin transitions.

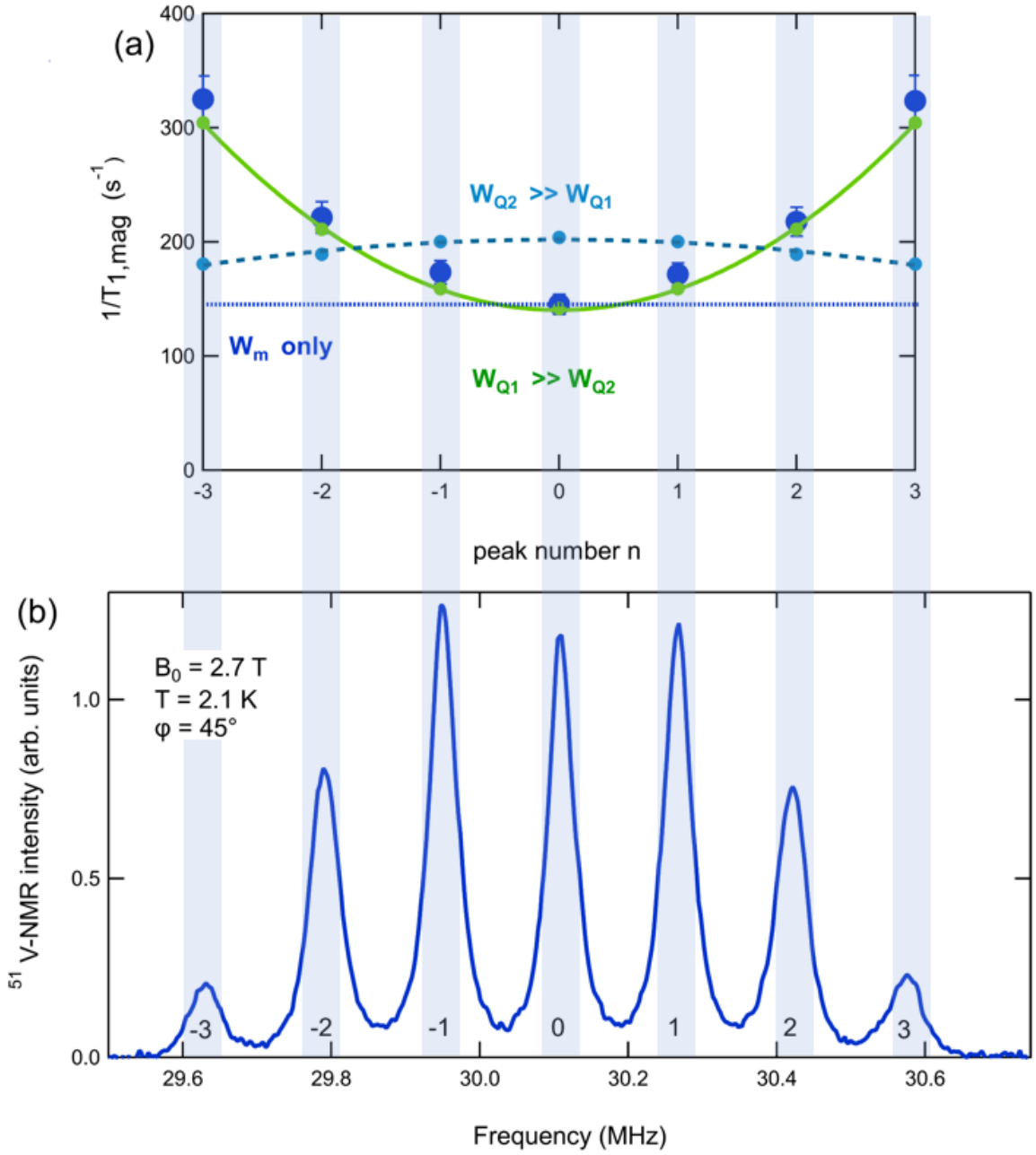

Figure 6.13: (a) Plot of the magnetic relaxation rate $T_{1,\mathrm{mag}}^{-1} = 2W_m$ (large blue circles) with strongly enhanced relaxation rates on the outermost satellites ($n = \pm 3$) at $B_0 = 2.7$ T and $T = 2.1$ K. Purely magnetic relaxation should give identical $T_{1,\mathrm{mag}}^{-1}$ for all peaks (horizontal line). Fits to magnetic relaxation only of simulated relaxation curves that include $W_{Q1} = 2.3$ s^{-1} and $W_{Q2} = 0$ reproduce the upward curvature of $T_{1,mag}^{-1}$. Inclusion of $W_{Q2} = 2.3$ s^{-1}, but $W_{Q1} = 0$ leads to downward curvature. Lines are quadratic fits and vertical bars link relaxation data with the corresponding transitions of the NMR spectrum. (b) Spectrum of FIB sample at $B = 2.7$ T and $T = 2.1$ K.

trend visible in the data, illustrated by the solid green line in Fig. 6.13(a). Here, we have computed the relaxation curve for each transition in the presence of both W_m and W_{Q1}, and fit the curves to a purely magnetic relaxation model. Thus, the enhanced relaxation at the satellites indicates the presence of EFG fluctuations that contribute to the nuclear spin relaxation. Including W_{Q2} has a minor effect that is opposite to what is observed: if W_{Q2} fluctuations dominate, then the relaxation is enhanced for the inner transitions and suppressed for the outer transitions, as illustrated by the dashed cyan line. Thus our data suggest that $W_{Q1} > W_{Q2}$. This behavior is also in consistent T_1^{-1} angular dependence, where we find $W_{Q1}/W_{Q2}(\theta = 90°) = 4$.

6.7 Conclusion

In this chapter, we have studied rare earth insulator with quadropolar order $TmVO_4$, including NMR spectra nad relaxation rates as a function of temperature and field direction. We find that the magnetic shift tensor agrees quantitatively with direct dipolar coupling between the V nuclear moments and the Tm $4f$ moments. The spin-lattice relaxation rate exhibits a steep minimum for a field oriented 90° to the c axis, which is inconsistent with purely magnetic fluctuations. We find that T_1 scales with the lattice constant for shear strain, c_{66}, which softens and vanishes at the nematic transition. It is likely that both quadrupolar and magnetic fluctuations are present and drive spin-lattice relaxation. We also made some progress on lessening the demagnetizing field broadening and extracting both magnetic and quadrupolar T_1 relaxation channels.

Bibliography

[1] Anatole Abragam. *The principles of nuclear magnetism*. 32. Oxford university press, 1961.

[2] Mustafa Ahmed Ali Ahmed, Gonzalo A Alvarez, and Dieter Suter. "Robustness of dynamical decoupling sequences". In: *Physical Review A* 87.4 (2013), p. 042309.

[3] Yulieth Cristina Arango. "Electron spin resonance (ESR) spectroscopy of low-dimensional spin systems". PhD thesis. 2011.

[4] Neil W. Ashcroft and N. David Mermin. *Solid State Physics*. Thomson Learning, 1976.

[5] Claudia Avalos. "Detection and Polarization of Nuclear and Electron Spins using Nitrogen-Vacancy Centers". PhD thesis. University of California, Berkeley, 2014.

[6] Alex D Bain. "Coherence levels and coherence pathways in NMR. A simple way to design phase cycling procedures". In: *Journal of Magnetic Resonance (1969)* 56.3 (Feb. 1984), pp. 418–427. DOI: 10.1016/0022-2364(84)90305-6.

[7] John F Barry et al. "Sensitivity optimization for NV-diamond magnetometry". In: *Reviews of Modern Physics* 92.1 (2020), p. 015004.

[8] Michael SJ Barson et al. "Nanomechanical sensing using spins in diamond". In: *Nano letters* 17.3 (2017), pp. 1496–1503.

[9] B. Bleaney and M. R. Wells. "Radiofrequency Studies of $TmVO_4$". In: *Proceedings of the Royal Society of London. Series A, Mathematical and Physical Sciences* 370.1741 (1980), pp. 131–153. ISSN: 00804630.

[10] B. Bleaney et al. "Nuclear electric quadrupole interaction in $LnVO_4$". In: *Journal of Magnetism and Magnetic Materials* 31-34 (Feb. 1983), pp. 745–746. DOI: 10.1016/0304-8853(83)90664-9.

[11] Felix Bloch. "Nuclear induction". In: *Physical review* 70.7-8 (1946), p. 460.

[12] S. Blundell. *Magnetism in Condensed Matter*. Oxford: Oxford Univ. Press, 2001.

[13] Christopher M Breeding, Sally Eaton-Magaña, and James E Shigley. "NATURALLY COLORED YELLOW AND ORANGE GEM DIAMONDS: THE NITROGEN FACTOR." In: *Gems & Gemology* 56.2 (2020).

[14] B Alex Brown and BH Wildenthal. "Status of the nuclear shell model". In: *Annual Review of Nuclear and Particle Science* 38.1 (1988), pp. 29–66.

[15] Dominik B Bucher et al. "Hyperpolarization-enhanced NMR spectroscopy with femtomole sensitivity using quantum defects in diamond". In: *Physical Review X* 10.2 (2020), p. 021053.

[16] Dominik B Bucher et al. "Quantum diamond spectrometer for nanoscale NMR and ESR spectroscopy". In: *Nature Protocols* 14.9 (2019), pp. 2707–2747.

[17] Herman Y Carr and Edward M Purcell. "Effects of diffusion on free precession in nuclear magnetic resonance experiments". In: *Physical review* 94.3 (1954), p. 630.

[18] Yiwen Chu and Mikhail D Lukin. "Quantum optics with nitrogen-vacancy centers in diamond". In: *Quantum Optics and Nanophotonics* (2015), pp. 229–270.

[19] Timothy DW Claridge. "Practical aspects of high-resolution NMR". In: *Tetrahedron Organic Chemistry Series*. Vol. 27. Elsevier, 2009, pp. 35–98.

[20] A.H. Cooke, S.J. Swithenby, and M.R. Wells. "The properties of thulium vanadate — An example of molecular field behaviour". In: *Solid State Communications* 10.3 (1972), pp. 265–268. ISSN: 0038-1098. DOI: https://doi.org/10.1016/0038-1098(72)90005-1.

[21] Jian-Hong Dai et al. "Quantum sensing with diamond NV centers under megabar pressures". In: *arXiv preprint arXiv:2204.05064* (2022).

[22] Christian L Degen, Friedemann Reinhard, and Paola Cappellaro. "Quantum sensing". In: *Reviews of modern physics* 89.3 (2017), p. 035002.

[23] A. P. Dioguardi et al. "NMR Evidence for Inhomogeneous Nematic Fluctuations in $BaFe_2(As_{1-x}P_x)_2$". In: *Phys. Rev. Lett.* 116 (10 Mar. 2016), p. 107202. DOI: 10.1103/PhysRevLett.116.107202.

[24] Marcus W Doherty et al. "The nitrogen-vacancy colour centre in diamond". In: *Physics Reports* 528.1 (2013), pp. 1–45.

[25] Marcus W. Doherty et al. "Electronic Properties and Metrology Applications of the Diamond NV^- Center under Pressure". In: *Phys. Rev. Lett.* 112 (4 Jan. 2014), p. 047601. DOI: 10.1103/PhysRevLett.112.047601.

[26] Florian Dolde et al. "Electric-field sensing using single diamond spins". In: *Nature Physics* 7.6 (2011), pp. 459–463.

[27] RJ Epstein et al. "Anisotropic interactions of a single spin and dark-spin spectroscopy in diamond". In: *Nature physics* 1.2 (2005), pp. 94–98.

[28] M. I. Eremets. *High Pressure Experimental Methods*. Oxford Science Publications, 1996.

[29] ROBERT Feigenson. "Flux Growth of Type RVO_4 Rare-Earth Vanadate Crystals". In: *Journal of the American Ceramic Society* 51.9 (Sept. 1968), pp. 538–539. DOI: 10.1111/j.1151-2916.1968.tb15689.x.

[30] S Felton et al. "Hyperfine interaction in the ground state of the negatively charged nitrogen vacancy center in diamond". In: *Physical Review B* 79.7 (2009), p. 075203.

[31] Rafael M. Fernandes et al. "Scaling between Magnetic and Lattice Fluctuations in Iron Pnictide Superconductors". In: *Phys. Rev. Lett.* 111 (13 Sept. 2013), p. 137001. DOI: 10.1103/PhysRevLett.111.137001.

[32] R. Matthias Geilhufe and Wolfram Hergert. "GTPack: A Mathematica Group Theory Package for Application in Solid-State Physics and Photonics". In: *Frontiers in Physics* 6 (2018), p. 86. ISSN: 2296-424X. DOI: 10.3389/fphy.2018.00086.

[33] David R Glenn et al. "High-resolution magnetic resonance spectroscopy using a solid-state spin sensor". In: *Nature* 555.7696 (2018), pp. 351–354.

[34] Michael Lurie Goldman et al. "State-selective intersystem crossing in nitrogen-vacancy centers". In: *Physical Review B* 91.16 (2015), p. 165201.

[35] Terry Gullion, David B Baker, and Mark S Conradi. "New, compensated carr-purcell sequences". In: *Journal of Magnetic Resonance (1969)* 89.3 (1990), pp. 479–484.

[36] Connor A Hart et al. "N-V–Diamond Magnetic Microscopy Using a Double Quantum 4-Ramsey Protocol". In: *Physical Review Applied* 15.4 (2021), p. 044020.

[37] Wolfram Hergert and R. Matthias Geilhufe. *Group Theory in Solid State Physics and Photonics: Problem Solving with Mathematica*. ISBN: 978-3-527-41133-7. Wiley-VCH, 2018.

[38] S. Hsieh et al. "Imaging stress and magnetism at high pressures using a nanoscale quantum sensor". In: *Science* 366.6471 (Dec. 2019), pp. 1349–1354. DOI: 10.1126/science.aaw4352.

[39] AE Hughes and WA Runciman. "Uniaxial stress splitting of doubly degenerate states of tetragonal and trigonal centres in cubic crystals". In: *Proceedings of the Physical Society (1958-1967)* 90.3 (1967), p. 827.

[40] Angel Ibarra et al. "Wide frequency dielectric properties of CVD diamond". In: *Diam. Relat. Mater.* 6.5-7 (1997), pp. 856–859.

[41] Koichi Katsumata. "High-frequency electron spin resonance in magnetic systems". In: *Journal of Physics: Condensed Matter* 12.47 (2000), R589.

[42] Rep Kubo. "The fluctuation-dissipation theorem". In: *Reports on progress in physics* 29.1 (1966), p. 255.

[43] M. Lawson et al. "Measurements of the NMR Knight shift tensor and nonlinear magnetization in URu_2Si_2". In: *Phys. Rev. B* 97.7 (Feb. 2018), p. 075138. DOI: 10.1103/physrevb.97.075138.

[44] Matthew Lawson. "NMR Studies of Heavy Fermion Materials". PhD thesis. University of California, Davis, 2017.

[45] Margarita Lesik et al. "Magnetic measurements on micrometer-sized samples under high pressure using designed NV centers". In: *Science* 366.6471 (Dec. 2019), pp. 1359–1362. DOI: 10.1126/science.aaw4329.

[46] K. M. Leung and D. L. Huber. "Low-frequency dynamics in cooperative Jahn-Teller systems". In: *Physical Review B* 19.11 (June 1979), pp. 5483–5494. DOI: 10.1103/physrevb.19.5483.

[47] Michael Loretz et al. "Spurious harmonic response of multipulse quantum sensing sequences". In: *Physical Review X* 5.2 (2015), p. 021009.

[48] ER MacQuarrie et al. "Mechanical spin control of nitrogen-vacancy centers in diamond". In: *Physical review letters* 111.22 (2013), p. 227602.

[49] Akash V. Maharaj et al. "Transverse fields to tune an Ising-nematic quantum phase transition". In: *Proc. Natl. Acad. Sci.* 114.51 (Dec. 2017), pp. 13430–13434. DOI: 10.1073/pnas.1712533114.

[50] H. J. Mamin et al. "Multipulse Double-Quantum Magnetometry with Near-Surface Nitrogen-Vacancy Centers". In: *Physical Review Letters* 113.3 (July 2014). DOI: 10.1103/physrevlett.113.030803.

[51] Mason C Marshall et al. "High-precision mapping of diamond crystal strain using quantum interferometry". In: *Physical Review Applied* 17.2 (2022), p. 024041.

[52] Pierre Massat et al. "Field-tuned ferroquadrupolar quantum phase transition in the insulator $TmVO_4$". In: (2021). DOI: 10.48550/ARXIV.2110.03791.

[53] Yuichiro Matsuzaki et al. "Optically detected magnetic resonance of high-density ensemble of NV- centers in diamond". In: *Journal of Physics: Condensed Matter* 28.27 (2016), p. 275302.

[54] Jeronimo R Maze et al. "Properties of nitrogen-vacancy centers in diamond: the group theoretic approach". In: *New Journal of Physics* 13.2 (2011), p. 025025.

[55] Nathan J McLaughlin et al. "Strong correlation between superconductivity and ferromagnetism in an Fe-chalcogenide superconductor". In: *Nano Letters* 21.17 (2021), pp. 7277–7283.

[56] Saul Meiboom and David Gill. "Modified spin-echo method for measuring nuclear relaxation times". In: *Review of scientific instruments* 29.8 (1958), pp. 688–691.

[57] Thomas Meier et al. "Magnetic flux tailoring through Lenz lenses for ultra-small samples: A new pathway to high-pressure nuclear magnetic resonance". In: *Science advances* 3.12 (2017), eaao5242.

[58] R. L. Melcher, E. Pytte, and B. A. Scott. "Phonon Instabilities in $TmVO_4$". In: *Phys. Rev. Lett.* 31 (5 July 1973), pp. 307–310. DOI: 10.1103/PhysRevLett.31.307.

[59] Thomas A Mittiga. "Sensing the local charge and strain environments surrounding Nitrogen-Vacancy centers in diamond". PhD thesis. 2020.

[60] Philip J.W. Moll. "Focused Ion Beam Microstructuring of Quantum Matter". In: *Annu. Rev. Condens. Matter Phys.* 9.1 (Mar. 2018), pp. 147–162. DOI: 10.1146/annurev-conmatphys-033117-054021.

[61] Tôru Moriya. "The effect of electron-electron interaction on the nuclear spin relaxation in metals". In: *Journal of the Physical Society of Japan* 18.4 (1963), pp. 516–520.

[62] Victoria A Norman et al. "Novel color center platforms enabling fundamental scientific discovery". In: *InfoMat* 3.8 (2021), pp. 869–890.

[63] John Frederick Nye et al. *Physical properties of crystals: their representation by tensors and matrices*. Oxford university press, 1985.

[64] Jner Tzern Oon et al. "Ramsey Envelope Modulation in NV Diamond Magnetometry". In: *arXiv preprint arXiv:2205.02387* (2022).

[65] J. A. Osborn. "Demagnetizing Factors of the General Ellipsoid". In: *Phys. Rev.* 67.11-12 (June 1945), pp. 351–357. DOI: 10.1103/physrev.67.351.

[66] J H Page and S R P Smith. "Microwave ultrasonic attenuation above the Jahn-Teller phase transition in $TmVO_4$". In: *Journal of Physics C: Solid State Physics* 16.2 (Jan. 1983), pp. 309–316. DOI: 10.1088/0022-3719/16/2/014.

[67] Linh My Pham. "Magnetic field sensing with nitrogen-vacancy color centers in diamond". PhD thesis. 2013.

[68] MHL Pryce. "A modified perturbation procedure for a problem in paramagnetism". In: *Proceedings of the Physical Society. Section A* 63.1 (1950), p. 25.

[69] Lucio Robledo et al. "Spin dynamics in the optical cycle of single nitrogen-vacancy centres in diamond". In: *New Journal of Physics* 13.2 (2011), p. 025013.

[70] Simon Schmitt et al. "Submillihertz magnetic spectroscopy performed with a nanoscale quantum sensor". In: *Science* 356.6340 (May 2017), pp. 832–837. DOI: 10.1126/science.aam5532.

[71] Yan-Xing Shang et al. "Magnetic Sensing inside a Diamond Anvil Cell via Nitrogen-Vacancy Center Spins". In: *Chinese Physics Letters* 36.8 (Aug. 2019), p. 086201. DOI: 10.1088/0256-307x/36/8/086201.

[72] T Shiroka et al. "A two-axis goniometer for low-temperature nuclear magnetic resonance measurements on single crystals". In: *Review of Scientific Instruments* 83.9 (2012), p. 093901.

[73] Maria Simanovskaia et al. "Sidebands in optically detected magnetic resonance signals of nitrogen vacancy centers in diamond". In: *Physical Review B* 87.22 (2013), p. 224106.

[74] Charles P Slichter. *Principles of magnetic resonance*. Vol. 1. Springer Science & Business Media, 2013.

[75] S.H. Smith and B.M. Wanklyn. "Flux growth of rare earth vanadates and phosphates". In: *Journal of Crystal Growth* 21.1 (Jan. 1974), pp. 23–28. DOI: 10.1016/0022-0248(74)90145-6.

[76] David W Snoke. *Solid state physics: Essential concepts*. Cambridge University Press, 2020.

[77] LG Steele et al. "Optically detected magnetic resonance of nitrogen vacancies in a diamond anvil cell using designer diamond anvils". In: *Applied Physics Letters* 111.22 (2017), p. 221903.

[78] Louis Steele. "Development of a Nitrogen-Vacancy-Center Magnetometer for High Pressure Studies using Designer Diamond Anvil Cells". PhD thesis. University of California, Davis, 2018.

[79] A Suter et al. "Mixed magnetic and quadrupolar relaxation in the presence of a dominant static Zeeman Hamiltonian". In: *Journal of Physics: Condensed Matter* 10.26 (1998), p. 5977.

[80] JP Tetienne et al. "Magnetic-field-dependent photodynamics of single NV defects in diamond: an application to qualitative all-optical magnetic imaging". In: *New Journal of Physics* 14.10 (2012), p. 103033.

[81] T Van der Sar et al. "Decoherence-protected quantum gates for a hybrid solid-state spin register". In: *Nature* 484.7392 (2012), pp. 82–86.

[82] I Vinograd et al. "Second order Zeeman interaction and ferroquadrupolar order in TmVO4". In: *npj Quantum Materials* 7.1 (2022), pp. 1–8.

[83] Xiaoche Wang et al. "Electrical control of coherent spin rotation of a single-spin qubit". In: *npj Quantum Information* 6.1 (2020), pp. 1–6.

[84] Z Wang et al. "ac Sensing Using Nitrogen-Vacancy Centers in a Diamond Anvil Cell up to 6 GPa". In: *Physical Review Applied* 16.5 (2021), p. 054014.

[85] Z Wang et al. "Anisotropic nematic fluctuations above the ferroquadrupolar transition in TmVO 4". In: *Physical Review B* 104.20 (2021), p. 205137.

[86] S. T. Weir et al. "Epitaxial diamond encapsulation of metal microprobes for high pressure experiments". In: *Appl. Phys. Lett.* 77 (2000), p. 3400. DOI: 10.1063/1.1326838.

[87] R.L. Workman et al. *Review of Particle Physics*. 2022.

[88] DE Wortman, RP Leavitt, and CA Morrison. "Analysis of the ground configuration of Tm3+ in YVO4". In: *Journal of Physics and Chemistry of Solids* 35.4 (1974), pp. 591–593.

[89] Fei Xue et al. "Measurement of statistical nuclear spin polarization in a nanoscale GaAs sample". In: *Physical Review B* 84.20 (2011), p. 205328.

[90] King Yau Yip et al. "Measuring magnetic field texture in correlated electron systems under extreme conditions". In: *Science* 366.6471 (Dec. 2019), pp. 1355–1359. DOI: 10.1126/science.aaw4278.